**Trinity College Dublin**
Coláiste na Tríonóide, Baile Átha Cliath
The University of Dublin

# *Evaluation of 3D Photogrammetry Tools for Applications in the Scanning Electron Microscope*
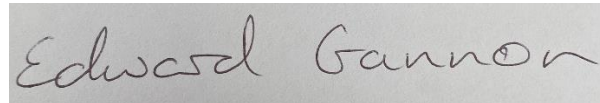
Author:

Edward Gannon

20328472

Supervisor:

Dr. Lewys Jones

(2023)

## Plagiarism Declaration

I have read and I understand the plagiarism provisions in the General Regulations of the University Calendar for the current year, found at: http://www.tcd.ie/calendar. I have also completed the Online Tutorial on avoiding plagiarism, 'Ready, Steady, Write', located at

https://libguides.tcd.ie/plagiarism/ready-steady-write.



## Acknowledgments

I would like to thank the entire Ultramicroscopy Research Group, the technical staff of the AML, and of course my supervisor Professor Jones for their assistance and support during this project. Professor Jones' support, particularly through this busy period throughout lockdowns and reopening and ensuring the progress of my project. The entire technical staff of the AML deserves thorough thanks for their work in maintaining the laboratories. The great support network that was the research group provided a great place for sharing ideas. Special thanks to Patrick Mc Bean and Professor Jones who provided fantastic feedback for my thesis before submission. I would also like to acknowledge my family for always believing in me.

**Work from this thesis has been presented at the following conferences:**

- Microscopy Society of Ireland Symposium 2021 (Presentation)
- Microscopy Society of Ireland Symposium 2022 (Poster)

# Abstract

3D models find application in a range of materials science areas, from fractography and failure studies to 3D printed metal topology. Atomic force microscopy (AFM) is commonly used for measuring surface topology, though this is limited to relatively flat surfaces and by tip geometry. However, 3D data can be obtained from scanning electron microscope (SEM) images via quadrant detectors ("shape from shading"), stereo pair reconstructions or photogrammetric datasets. Photogrammetry constructs 3D models from several 2D images at different viewpoints through the use of a number of mathematical algorithms to extract the scene's geometry. With the reconstruction only requiring 2 or more 2D images, standard SEM imaging can be used in place of digital photography, and without requiring specialised hardware. The widespread popularity of photogrammetry has created an upsurge in reconstruction software, both commercial and open source, whose rapid advancements can be leveraged for SEM applications. Photogrammetry, however, can be a time consuming and expensive process, depending on the sample being imaged and the software used for model reconstruction. We demonstrate an efficient method for 'microscopy for photogrammetry', developing a framework for selecting imaging parameters to ensure a satisfactory photogrammetric data set is acquired. This results in a practical and accessible procedure for reconstructing 3D microscale structures using open-source photogrammetry software in the SEM.

# Table of Contents

# 1. Glossary

VR – Virtual Reality

SIFT – Scale-invariant feature transform

SfM – Structure from Motion

MVS – Multi-View Stereo

SEM – Scanning Electron Microscopy/Microscope

TEM – Transmission Electron Microscope

SE – Secondary Electron

HC – High Current

E-T – Everhart-Thornley Detector

BSE – Backscattered Electron

WD – Working distance

ESB – Energy Selective Backscatter Detector

In-Lens – In-Lens Detector

STEM – Scanning Transmission Electron Microscopy

AFM – Atomic Force Microscope

EDX – Energy Dispersive X-Ray Spectroscopy

EP - Eucentric Point

## 2.  Motivation

Accurate measurement of the three-dimensional form is essential for enhancing the performance and behaviour of technologically significant devices, ranging from electronics to medical stents. The intricate relationship between a device's 3D structure and its functionality requires precise measurements to identify areas for improvement, in order to drive innovation in device design. By capturing and analysing the 3D characteristics of these devices, researchers can uncover new insights that contribute to the development of more efficient and advanced technologies.

# 3. Introduction

## 3.1. Stereo Pair imaging

When an observer looks at a solid object with both eyes, the lateral separation of the eyes in the observer's head means that each eye obtains a 2D image of the object at slightly different viewpoints.[1] The observer's brain/central nervous system uses this binocular disparity to unite the two images and produce a single 3D representation of the scene and thus perception of depth, in a process called stereopsis. Humans, through knowledge and experience of the world, can also perceive depth through a number of monocular depth cues (linear perspective, shading, relative size), although it is not as powerful as binocular depth perception. In other words, depth perception allows humans to view the world around them in three dimensions.[2–4]

### 3.1.1. History of 3D viewing

Charles Wheatstone is credited with the discovery of stereopsis and subsequent invention of the first stereo scope (called the Wheatstone mirror) in 1838.[5] Wheatstone illustrated that horizontal disparity was an effective depth cue by creating the illusion of depth from two 2D pictures that differed only in their horizontal position.[6] This illusion of depth is called stereoscopy and has been a source of entertainment/amusement since Victorian times. This method brought 2D photographs to life and allowed ordinary people to see a world they may never see from the comfort of their own home.
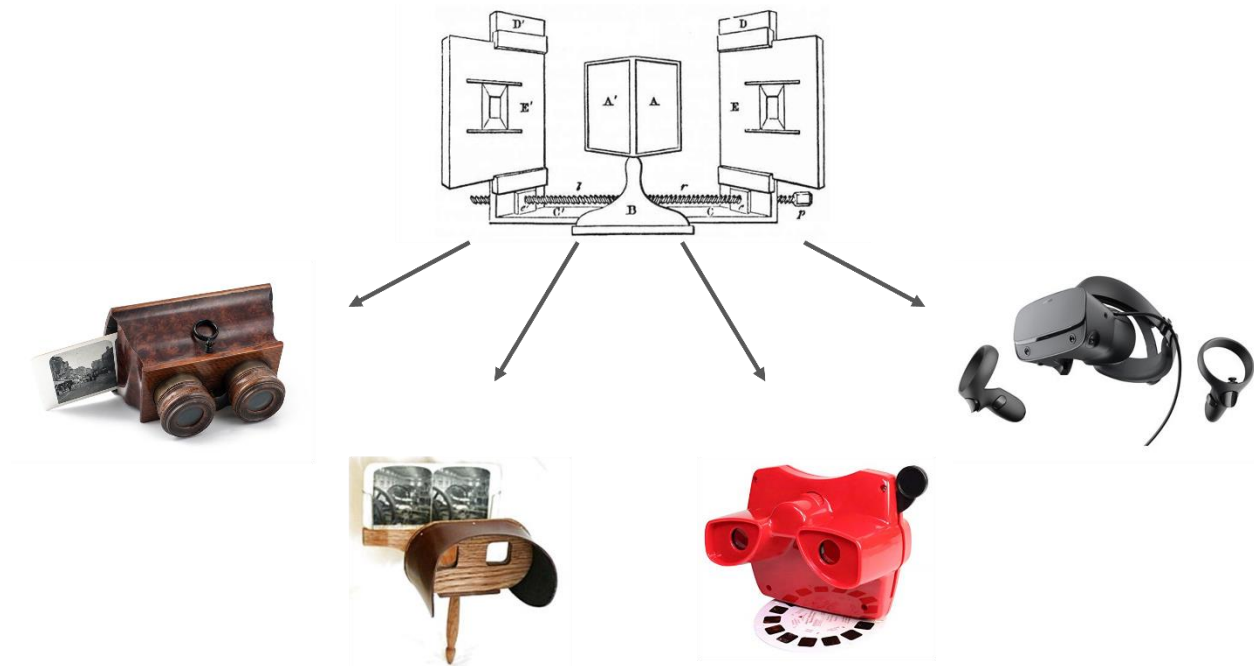
*Figure 1: The Wheatstone mirror, invented by Charles Wheatstone in 1838 and the 3D stereoscopic viewers which have been developed since then, including: The Holmes Steropticon, the Mattel View-Master and modern Virtual Reality headsets (like the Oculus Rift)*

The Wheatstone mirror, or stereoscope (Figure 1), involved the use of a pair of mirrors at 45-degree angles to the observer's eyes, each of which reflected an image onto screens located off to the sides. The brain fuses the two images as one, proving that each eye sees one image.[5] The stereoscope has continually been improved upon throughout history, from the bulky Wheatstone mirror, came the Holmes Stereopticon, which was then improved upon by the Mattel View-Master in the early 1900s. Modern applications of stereoscopes include red-blue 3D movies (anaglyph stereo pairs) and Virtual Reality (VR) headsets, such as the Oculus Rift or the HTC Vive.[7–9] Anaglyph 3D stereo pair imaging involves taking two images of the same subject at slightly different perspectives. This imitates how our eyes look at objects from separate perspectives and can determine depth. The two images are taken and overlaid.[10] The individual images are filtered into the viewers separate eyes by encoding the images with chromatically opposite colours (red and blue) or in modern 3D movies, by polarising the images differently.[11] Glasses with a red and a blue lens or different polarising lenses are then used to view the subject in 3D.[12] This imitates how our eyes look at objects from separate perspectives in order to determine depth. Nowadays VR headsets allow a stereoscopic viewer to not only view 2D images in 3 dimensions, but to interact and fully immerse themselves into

4

a simulated environment through the use of images projected into each eye and accelerometers in the head mounted display and hand controllers to track head and hand movement.[8] Having been first developed in the mid 90's, VR has recently seen an enormous rise in popularity due to their heavy use in entertainment (video games)[13], education (military or medical training)[14,15] and business settings (metaverse).[16]

## 3.2. Photogrammetry

Photogrammetry is the science of taking 3D measurements from 2D photographs.[17] Generally, when measuring the size of an object, e.g. the length, height and width of a building, then an operator would carry this out on site. However, in the case where this building did not exist anymore, then these dimensions could be determined through historical photos, provided the scale of the photos was known.[18] This process is an example of photogrammetry. Photogrammetry can be defined as any technique allowing the modelling of 3D space from two or more 2D images.[19] In other words, it is a measurement technique which can extract the geometry of a 3D object from a number of 2D images of the object. 3D reconstruction in any environment is one of the integral tasks in 3D computer vision for artificial intelligence which has occupied mathematics and computer science researchers for the last 3 decades.[20]

### 3.2.1. History of photogrammetry

Photogrammetry finds origin in ancient Greece, with Aristotle laying the foundation with his theory of vision.[21] This was further worked upon through the perspective technique, which involved the implementation of 3D cues within 2D paintings by mathematicians, architects and painters in the 18th century.[22] Photogrammetry techniques couldn't exist without the existence of a photographic process, which was pioneered in the 19th century by Nicéphore Niépce.[23] In the late 19th century, the first photogrammetry experiments involving aerial photographs for the process of topographical mapping were carried out by Colonel Aimé Laussedat in his hot air balloon. His dedication to the subject earned him the title "The father of photogrammetry".[24] Technological innovation and progress in film, cameras, photogrammetric techniques and flight continued through the 20th century, driving continual innovation across the sector. The drive for military reconnaissance allowed for improved

research into aerial imaging/photogrammetry and therefore the mass production of maps during the first and second world wars.[25,26]
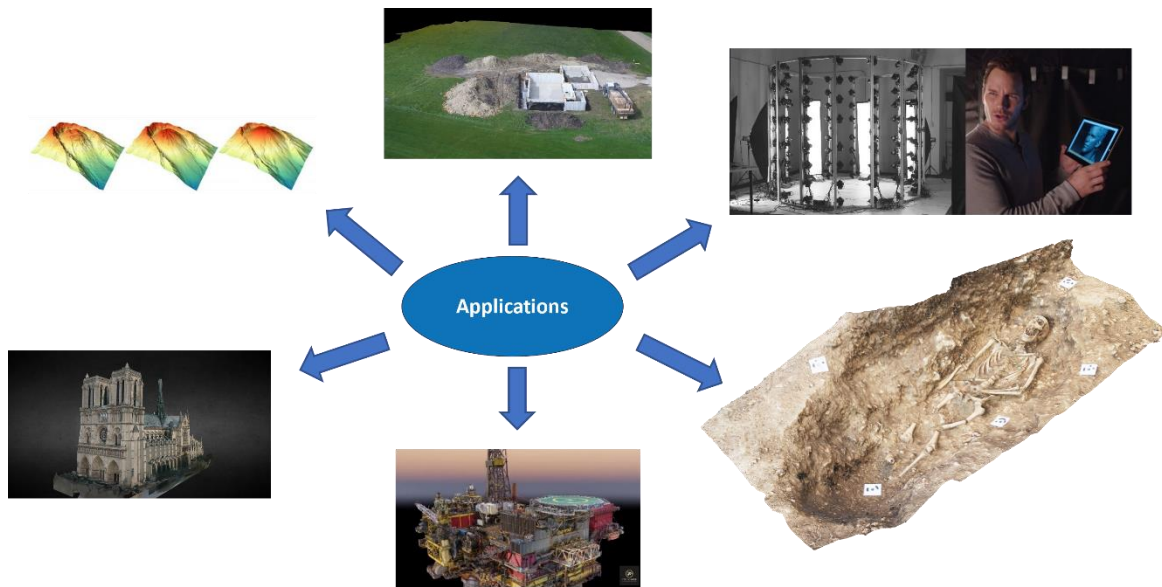


Figure 2: Outlines the many industries employing photogrammetry to improve the quality of work or make it more efficient. The industries displayed are (top-left, clockwise) Geoscience, Construction, Entertainment, Archaeology, Health and Safety, Urban Surveying.

The modern development of photogrammetry has been heavily influenced by the advancement and falling cost of computing power, software engineering, commercial unmanned aerial vehicles (drones) and digital photography.[27,28] These advancements have improved the field of topographical mapping, but more importantly, have made photogrammetry more accessible to a plethora of different industries/fields, including hobbyists. The incorporation of photogrammetry into different applications has allowed it to evolve from solely aerial datasets of a topography to images of close-range subjects. Some of these industries are outlined in Figure 2. The field of geoscience which uses aerial photogrammetry to study volcanos, their growth over time and possibly predict eruptions.[29] Photogrammetry allows construction firms and safety inspectors to safely monitor the progress of building sites or hazardous/difficult to reach areas.[30,31] Archaeologists use photogrammetry to record buildings, artefacts and dig sites. It allows for a better understanding of the subject and offers a more comprehensive record than drawn records.[32] Photogrammetry is also used in the film and video gaming industry to enhance the computer-

generated imagery (CGI) and to bridge the gap between the real and digital world.[33,34] Photogrammetry is developed on the angles and relative shifts of the objects within the scene. Therefore, the mathematics of the algorithms will hold up for objects of any size including celestial objects[35] and micro- and nanoscale objects. This is discussed further in section 3.2.2.4.
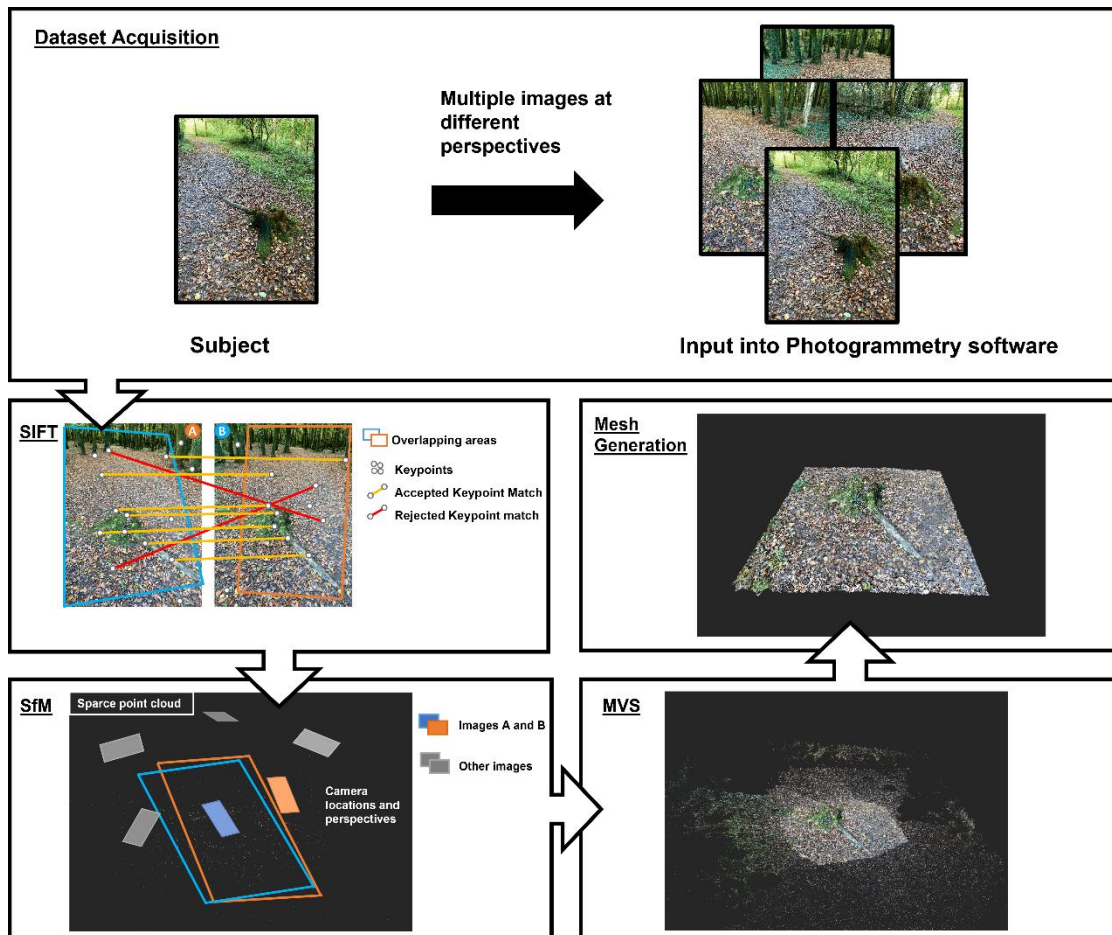


*Figure 3: The key stages in a photogrammetry workflow: (1) Dataset acquisition of a subject, in this case of a tree stump, imaged with an iPhone camera. (2) keypoint matching through Scale-invariant feature transform (SIFT). (3) Structure From Motion (SfM) with camera position/perspective and sparse point cloud as an output. (4) Densified point cloud computed via Multi view stereo (MVS). (5) 3D model and mesh generation*

Photogrammetry software reconstructs sets of 2D photographs of the original 3D source object into 3D computerised models. In order to complete this task, the software employs a number of mathematical algorithms.[36] These algorithms, summarised in Figure 3, have the ability to determine/compute the camera's position and extract 3D information from a scene, through the use of a series of overlapping images. This negates the need for a *priori*, or

prerequisite information on camera location, orientation, calibration and/or known reference points within the scene, as these are all computed by the software.[37]

### 3.2.2.    Summary of Common Algorithms

#### 3.2.2.1.  *Structure from Motion (SfM)*

Structure from Motion (SfM) is a photogrammetric technique which is modelled on the basis that humans, with binocular vision and the ability to view objects while in motion, can determine an object's depth, volume and 3D features.[38] It involves a number of mathematical algorithms in order to carry this process out. Such algorithms include Scale-invariant feature transform (SIFT), Bundle adjustment and multi-view stereo, among others.[39,40]

#### 3.2.2.2.  *Scale invariant feature transform (SIFT)*

SIFT, also known as keypoint extraction, identifies points or sets of pixels known as keypoints, that are locally distinct, i.e. have distinctive contrast or texture. When keypoints are on two or more images within a dataset and SIFT gives them each a numerical descriptor, called a feature vector.[41] The keypoint is found on the image through a difference of Gaussian approach: multiple Gaussian blurs are applied at different magnitudes and then subtracted from one another. The stacked blur will reveal extreme points, those that stand out with high contrast or intensity.[42] These key points are then matched up on all of the images in which they appear.
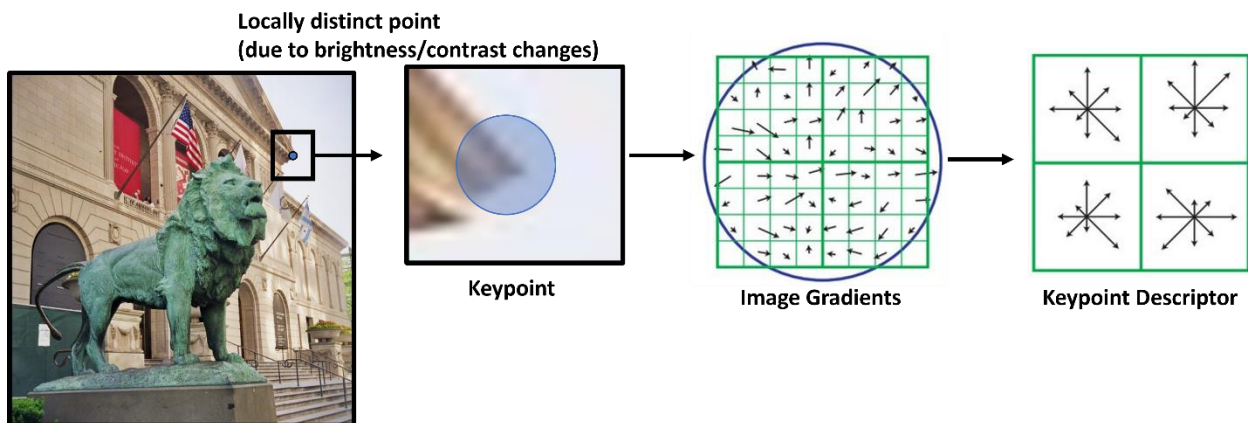


*Figure 4: A visual description of how the SIFT algorithm determines keypoints on images.*

Figure 4 illustrates how the SIFT algorithm determines keypoints on the basis of localised differences of intensity/brightness/contrast. It does this by analysing the surrounding image patch or local area/neighbourhood of the distinctive point within the image and determining

the intensity gradients of this area/patch, through collecting histograms of the intensity of the local image area (image gradients).[43] These histograms are discretised thus giving the local point its descriptor vector.[44] This exact intensity gradient is then used to search for where the intensity gradient/descriptor vector appears in other images taken of the same scene/object.[45] Therefore, the amount by which one image's area includes the area covered by another image is key. When this coverage is expressed as a percentage it is commonly called overlap. 60-70% overlap is quoted as the suggested minimum overlap for most photogrammetry software, to ensure the same points between images are being tracked by the algorithm.[46] This is known as keypoint matching an algorithm in computer vision to detect and describe local features in images which was invented by David Lowe in 1999.[47] If a sufficient number of keypoints are matched across an acceptable number of images, then the SfM process carries out a bundle adjustment.

### 3.2.2.3. Bundle Adjustment

Bundle adjustment is an estimation technique which estimates the location of the computed/matched keypoints from the SIFT algorithm in 3D space.[48] It is not technically a part of the SfM process but is a very common next step in order to refine the initial point cloud produced by SfM.[49]
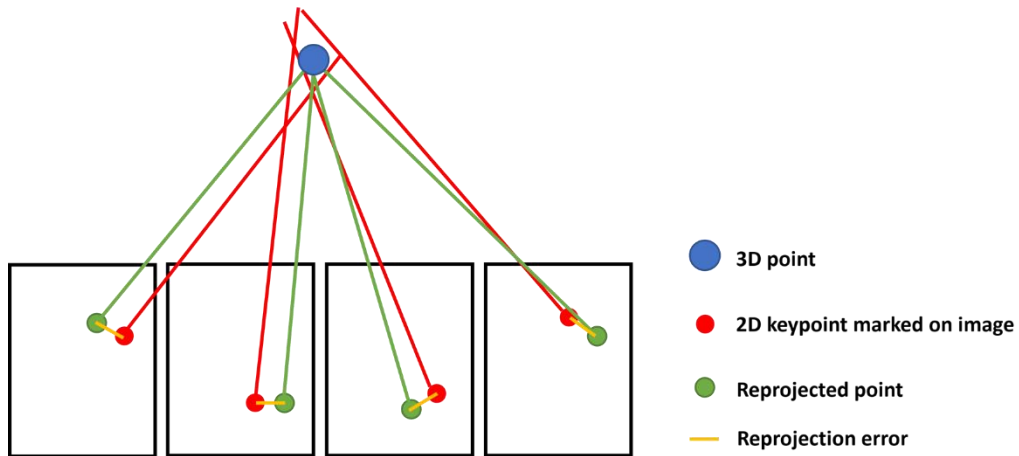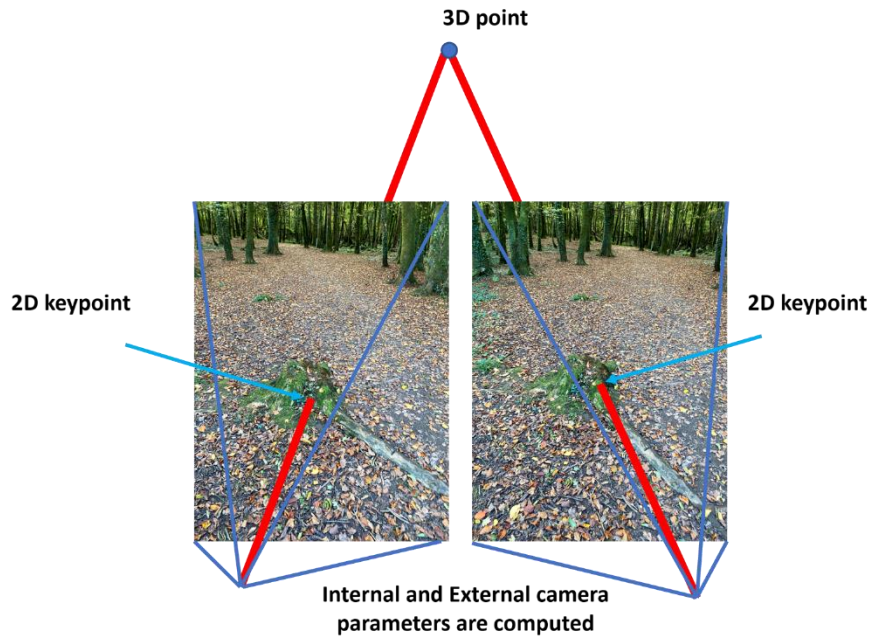
*Figure 5: (Top) A schematic of how bundle adjustment uses the keypoints, computed by SIFT, to determine the camera's internal and external parameters as well as the position of the keypoint in 3D space. (Bottom) Also shown is how the algorithm determines the reprojection error of the 2D points in relation to the 3D point.*

Bundle adjustment estimates the 2D keypoints' location in 3D, as presented in Figure 5. The algorithm also estimates the camera's external parameters, known as its position and orientation. It calculates this to 6 degrees of freedom (i.e. 3 movements (x, y, z) along an axis and 3 rotations (roll, pitch, yaw) around an axis).[50] The algorithm also estimates the camera's internal parameters (focal length, principal point etc.). The estimation of the location of the

keypoints and the location of the cameras, in 3D space, are completed at the same time in order to ensure that reprojection error is minimised.[51] As outlined by Figure 5, the reprojection error is the distance between a reprojected keypoint and a 2D keypoint, computed by SIFT.[52] Minimising the reprojection error leads to a large least squares problem.[53] Due to sparsity (inability to observe all key points in all images) in the dataset, only some keypoints/features will be present in all or many images. This will lead to a number of zeroes, resulting in sparse matrices. The algorithm can exploit this sparsity by computing just the non-zero parts of the sparse matrices to make this process more computationally efficient.[54] Thus this algorithm optimises 3D point and camera placements simultaneously by minimising the squared error between the estimated and measured image feature locations.[55] What results is a so-called sparse point cloud, shown in Figure 3, which displays the matched keypoints in their positions in 3D space.[56]

### 3.2.2.4. Multi View Stereo (MVS)

Multi view stereo (MVS), as the name suggests, is a multiple viewpoint version of the stereo matching algorithm, invented in 1979.[57] Instead of just two viewpoints however, the algorithm would use multiple viewpoints in an effort to increase surface texture and decrease image noise.[58] It allows for a huge number of images to be used with the only constraint on the user being computing memory/power and time.[59] MVS algorithms are able to produce accurate, coloured and dense point clouds from multiple images, if the cameras' parameters and viewpoint positions have been determined.[60] These parameters and viewpoints are already determined by the previous two techniques (SIFT and Bundle adjustment), which are given by the sparse point cloud. The MVS algorithm sets out to densify the sparse point cloud into a dense point cloud, as depicted in Figure 3, through attempting to determine the 3D location of every pixel in every image. It does this using the sparse point cloud, through a depth map computed by trigonometry between the rays projected from the camera positions to the image pixels.[61] Dense point clouds are subsequently converted into mesh, through one of several algorithms, such as Poisson surface reconstruction.[62] It does this by linking the points in the dense point cloud to produce a polygon mesh, which is made up of a collection of 2D shapes which defines the 3D shape of the model.[63] The more points that the dense point cloud

has, the smaller the individual polygonal shapes leading to a more refined polygonal mesh. The mesh can be further refined through photo-consistency checking algorithms and UV application. Texturing the 3D mesh is carried out through UV unwrapping. The letters "U" and "V" denote the axis of the 2D texture as x, y and z are already being used to denote the objects position in 3D space. UVs are essentially points which indicate which pixels on the texture corresponds to which vertexes on the 3D mesh. What results is a photo realistic version of the 3D mesh based on the 2D images it was created from. This improves the mesh's texture and photo realism and lead to a working 3D model as displayed in Figure 3.[64]

These algorithms have made photogrammetry a lot more accessible to the general public and have drastically altered the workflow of a photogrammetric acquisition for the better, saving time and money.[65] Where a traditional photogrammetric topographic workflow would involve extensive planning and the use of specialised equipment, workers and/or a number of helicopter flights, a modern digital photogrammetry workflow could just involve a single operator with a DSLR camera and a personal computer.[66,67] This greatly reduces the cost and time factor involved with photogrammetry, especially because of great advances in DSLR cameras, unmanned aerial vehicles (UAVs/Drones) and GPU and computing power.[68,69] That being said, because photogrammetry is a passive technique, the quality of the resultant 3D reconstruction is entirely dependent on the quality of the input images. Therefore, even though the general public has good access to relatively good cameras, good computing power and robust photogrammetry software, the acquisition designs, cameras and settings should still be optimised and considered with utmost care.[37]

Originally designed for macro-scale photogrammetry applications, these algorithms have been adapted and applied to microscopy, specifically in the context of scanning electron microscopy (SEM).[70] Photogrammetry relies on angle measurements, which are size invariant, and relative shifts, which are proportional to scale. As a result, photogrammetry can be scaled up to huge objects, like the sun,[35] or can be scaled down to the micro scale while maintaining the integrity of its mathematical algorithms' principals. With the aid of these algorithms, SEM operators can now capture a series of micrographs and reconstruct detailed 3D models of microscopic samples. This will be evaluated in the following section.

## 3.3. Scanning Electron Microscopy

Scanning electron microscopy (SEM) is a characterisation technique used in a multitude of different fields. It is widely used in both academia and in industry, for quality control or failure analysis of materials.[71,72] As the name suggests, electron microscopes use a beam of electrons as a source of illumination, in contrast to light rays used for a light microscope.[73] There are two main types of electron microscopes: Scanning Electron Microscope (SEM), where the electron beam is scanned over the sample and the resultant signal collected at a detector; Transmission Electron Microscope (TEM), which involves the electron beam passing fully through the sample and being detected at the bottom of the microscope.

## SEM Column

**Electron Gun**

**Magnetic Lens**

**Backscattered Electron Detector**

**In-Lens SE Detector**

**Magnetic Lens**

**Secondary Electron Detector**
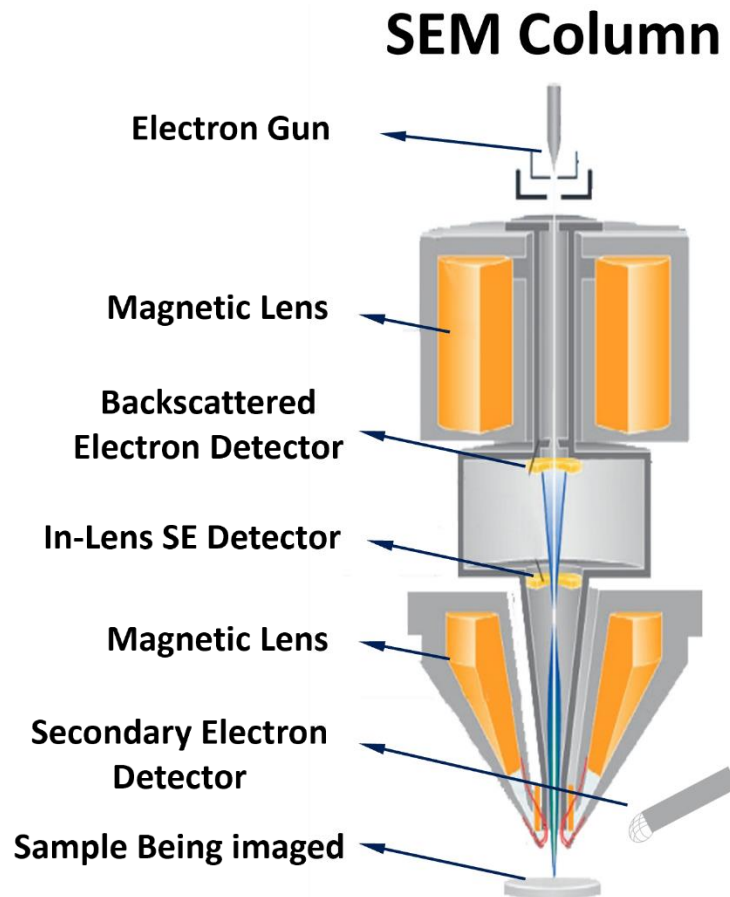
**Sample Being imaged**

*Figure 6: Cross-section and main components of **Zeiss© GEMINI** electron column.*

The internal components of the SEM electron column are described in Figure 6. Electron beams are produced by electron guns (i.e. a negatively charged electrode) via one of two processes called thermionic emission[74] or field emission.[75] Thermionic emission involves the

liberation of electrons from a cathode when it's heated to a certain temperature and field emission involves creating a strong electric field to extract electrons from the tip of a sharp W/ZrO$_2$ crystal (Schotkky Field Emission gun). Electrons are negatively charged sub-atomic particles and can be manipulated by electric or magnetic fields.[76] The electrons are accelerated down the electron column by an accelerating voltage, which can determine the velocity and energy of the electron beam. Samples to be imaged by electron microscopes must be conductive or made to be conductive, through various methods (Au/Pd sputtering, Ag colloid etc.). If an insulating sample is used, the electron beam can cause a build-up of electric charge on the surface of the sample. This can cause various imaging artefacts (due to beam deflection from the negative surface charge) and sample damage.[77] Samples within an electron microscope must be under vacuum to allow free unimpeded movement of electrons from the electron gun to the sample and then to the detector. This vacuum is produced through a series of increasingly powerful pumps.[78] Resolution is defined as the smallest distance between two points that can still be distinguished as two separate entities. The resolution of a microscope depends on the wavelength of the illumination source, diffraction effects cause the image to distort, leading to blurred or smeared-out features. TEMs have a theoretical resolution of approximately 0.05 nm, which is much smaller than the smallest resolution achievable by light microscopy (400-700 nm). SEMs have a theoretical resolution of approximately 1-5 nm, which is also much smaller than light microscopy. However achieving a theoretical resolution can be difficult due to a number of factors (i.e. instrument stability, sample preparation and imaging conditions).[79,80]

As described by Louis De Broglie,[81,82] electrons have a wave-particle duality just as photons do, and coincidentally have much smaller wavelengths ($10^{-12}$ m) than light rays ($10^{-7}$ m).[83,84] This was described by De Broglie, where the wavelength ($\lambda$) is inversely proportional to the momentum ($m\ v$) of the particles: $\lambda = \hbar\ /\ m\ v$ where $\hbar$ is the reduced Planck's constant. The momentum of photons of light is governed by their energy $(E = h\ f)$, and therefore their frequency/wavelength ($c = f\ .\ \lambda$). A visible light microscope's resolution is therefore constrained by the large wavelengths of the visible light range (700-300 nm). The best possible resolution of a light microscope would therefore be 300 nm x 0.5 = 150 nm.[85] Due to the much

smaller wavelength of electron beams, much smaller objects can be resolved by the electron microscope, such as the SARS-CoV-2 viral structure.[86] The resolution of electron micrographs depends on the sample composition and the parameters used on the microscope, such as: detector used, accelerating voltage and working distance (WD).[87] The electron beam is then focused using electromagnetic lenses into a fine spot, onto the sample being imaged.[88] The distance between the pole piece and the beam's cross over is the WD. A small WD means the resolution of the sample will be larger due to a smaller electron flight to the sample. The strength of the magnetic field produced by the lenses and therefore the severity of the deflection of the electron beam can be modulated by changing the current supplied to the lenses.[89] The electromagnetic lenses therefore control the focus (using the condenser/objective lens),[87] astigmatism (using the quadrupole lens),[90] and magnification and position (using the scan coils) of the electron beam. The electron beam is then scanned across the surface of the sample being imaged in a rectangular fashion called a raster scan.[91] The aperture of the electron column is "hole", which has a variable radius, that the electron beam passes through. Aperture choice is dependent on the user's/sample's need. The aperture is placed in between the condenser lens and the objective lens. The aperture and condenser lens in the SEM play crucial roles in beam current and depth of field. The depth of field refers to the distance along the z-axis over which the sample remains in an acceptable focus. The WD, when increased, can also increase the depth of field, due to the decrease of the convergence angle. [92] In general, when the aperture size is large, the convergence angle of the electron beam is larger which decreases the depth of field of the image. Using a larger aperture, however, causes a larger probe diameter and therefore, allows for more electron beam current to reach the sample. This allows for increased signal yield to be produced by the sample, leading to larger contrast, with the drawback of having less resolution due to the larger spot size.[93] The electron column shown in Figure 6 is specifically a **GEMINI©** column, developed by **Zeiss©**.[94] The **GEMINI©** technology has been designed to overcome the main limiting factors of the SEMs resolution, using innovative solutions such as the integrated beam booster or the magnetic/electrostatic objective lens. The **GEMINI©** column does not have a multiple condenser lens set up and crossing over of the beam happens only after the objective

lens. The **GEMINI©**'s probe current can be influenced by the High current (HC) mode. HC mode doubles the beam current in comparison to standard operation parameters by changing the angle of the probe entering the objective allowing a greater flux of electrons. As a by-product, the convergence angle is decreased, which increases the depth of field. The higher current in a smaller beam diameter allows for a greater depth of field over the sample. However, tilting a flat specimen to a high degree can exceed this large depth of field. This leads to a focused centre of the image and out-of-focus edges. At high tilt angles, the sample's higher side causes underfocus, while the lower side causes overfocus of the electron beam. Consequently, the edges of the resulting electron micrographs appear defocused. This can be relieved through the use of dynamic focus. When dynamic focus is selected, the power amplifier supplies the objective lens with a "saw-tooth" current in order to modulate the focal point along the range focal changes across a tilt.
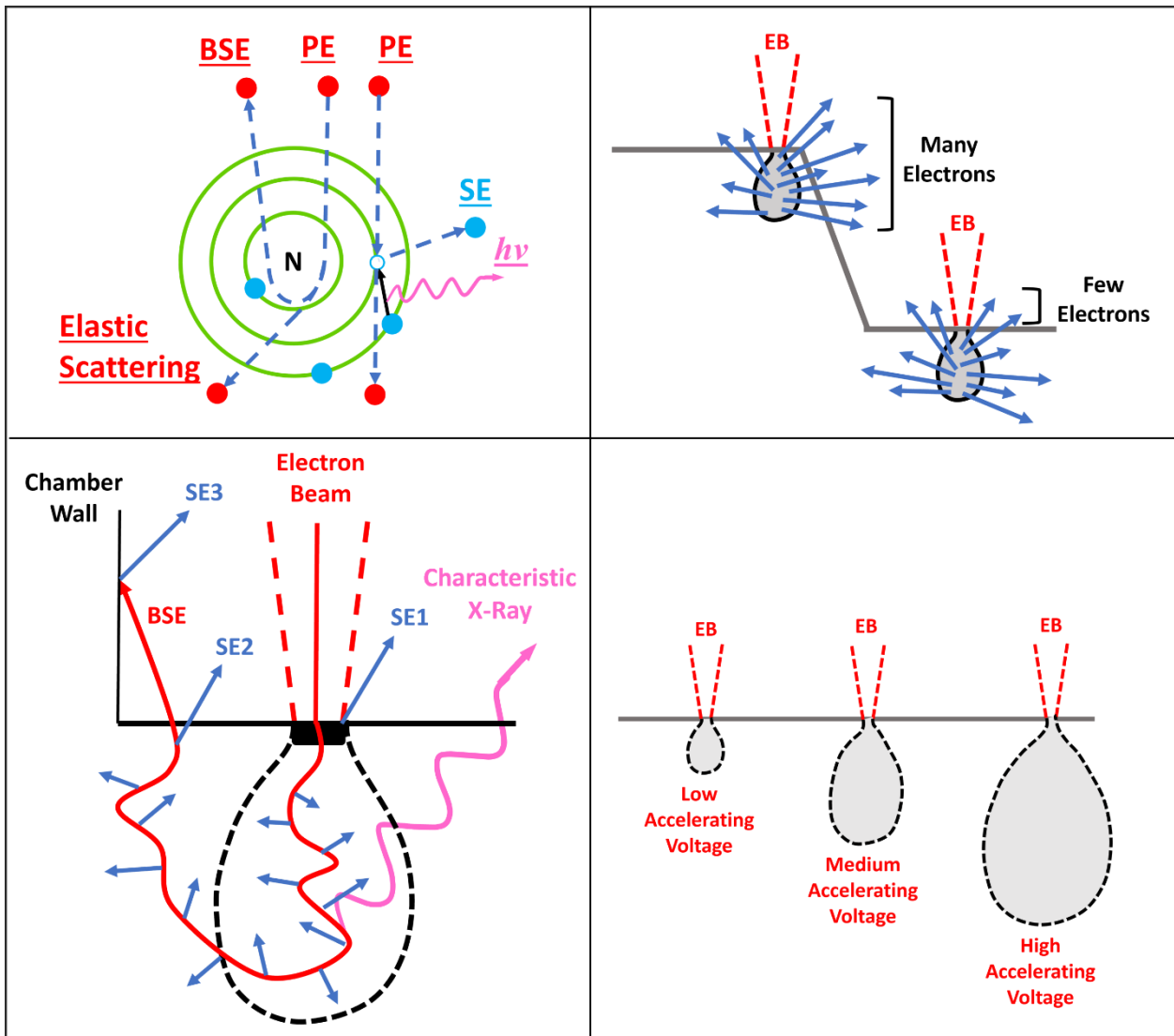
*Figure 7: Sample interactions of an electron beam. (Top-Left) describes how primary electrons (PE) can interact with sample atoms and produce different types of signals. (Bottom-left) describes the depth at which the electron beam can penetrate and where different SE (SE1, SE2 and SE3) and BSE originate from, this is also known as the interaction volume. (Top-Right) describes the edge effect and how a larger signal originates from higher aspect ratio surface structures. (Bottom-right) describes how the interaction volume changes with differing SEM parameters, in this case accelerating voltage.*

As presented in Figure *7* (top-left), when the electron beam scans the sample's surface it interacts with the sample's atoms. The energy exchange between the electron beam and the sample's atoms produces a number of signals which may be used as a source of contrast for an image (secondary electrons (SE), backscattered electrons (BSE), characteristic X-rays etc.).[95] BSEs occur when the incident electron beam undergoes elastic scattering with the atomic nuclei. There are two types of SE produced by the sample. SE1 are generated by the direct

impact of the electron beam with the sample. SE2 are generated by BSEs, which have elastically scattered, from deeper in the sample. SE3 are generated by high energy BSE which have emerged from the sample and strike the vacuum chamber wall or pole piece and generate SEs from these surfaces.[96] Some of the signals received from a scanned sample can give topographical contrast (SE) and others give characteristic contrast (BSE). These signals are collected by different detectors, which are placed in several different positions in the specimen chamber.[97]

The SE detector, an Everhart-Thornley (E-T) detector, solved the problem of detecting low energy SEs through post-specimen acceleration.[98] To prevent this from affecting the primary electron beam, the E-T detector is located at a distance from the primary beam, on the lateral wall of the sample chamber (Figure 6), off to the side of the sample being imaged. The E-T detector is sensitive to type 1,2 and 3 SEs as well as BSEs, providing both topographical and atomic number contrast.[93] Various topographical contrast mechanisms play a role in enhancing the visualisation of the SEM including: diffusion contrast, SE diffusion contrast, mass-thickness contrast, shadowing contrast and surface-tilt contrast. The edge effect, which is shown in Figure *7* (top-right), is primarily described by the shadowing and surface-tilt contrast mechanisms. Surface-tilt contrast refers to the variations of SE signal intensity from the surface of a sample when the incident electron beam interacts with inclinations of the surface on a specimen. When the surface is tilted/inclined the angle of incidence of the electron beam changes, which results in variations in SE emission and collection efficiency. Shadowing contrast is the mechanism when the incident electron beam strikes a bump or protruding feature on the sample surface. When the beam interacts with this raised area it causes a shadow to form on the surface behind the feature, caused by reduced SE emission.[99] This interplay of illumination and shading of the sample's protruding features, known as topographical contrast, is the dominant mechanism of secondary electron detection. It reveals the topography of the sample, providing a visual representation that is analogous to the way directional light reveals surface details, contours, and creates perception of depth, similar to how the human eye perceives three-dimensional objects.[93,100]

Through-the-lens (TTL) detectors, which include the energy selective backscattered (ESB) detector and the "In-Lens" SE detector. The In-Lens detector detects SE1 which are produced by the interaction of the electron beam and the sample surface, as described by Figure *7* (bottom-left). They are then captured by the lens' magnetic field and are then attracted to an E-T detector at the top of the lens.[93] This method of SE capture means that BSE are completely excluded, resulting in the In-Lens detector being much more surface sensitive.[101] It also reduces the topographic information given by the edge effect, as the detector is along the same axis as the electron beam, rather than to the side of the sample. This is analogous in the macroscale to an object being illuminated and viewed from top-down.

## 3.4. 3D Characterisation

Currently there are many techniques used to extract 3D images from electron microscopes. That is, images that represent the x, y and z axes of the sample. Obtaining 3D information provides valuable insights into the relationship between the chemical make-up, structure and performance of materials. [102] For this reason, many industries require more spatial resolution than that in the 2D. Fields like the petrochemical industry to examine the porosity of clays,[103] Carbon-Carbon composite research to determine its internal density[104] and semiconductor industry to determine the surface topography and the subsurface tomography of the sample.[105]
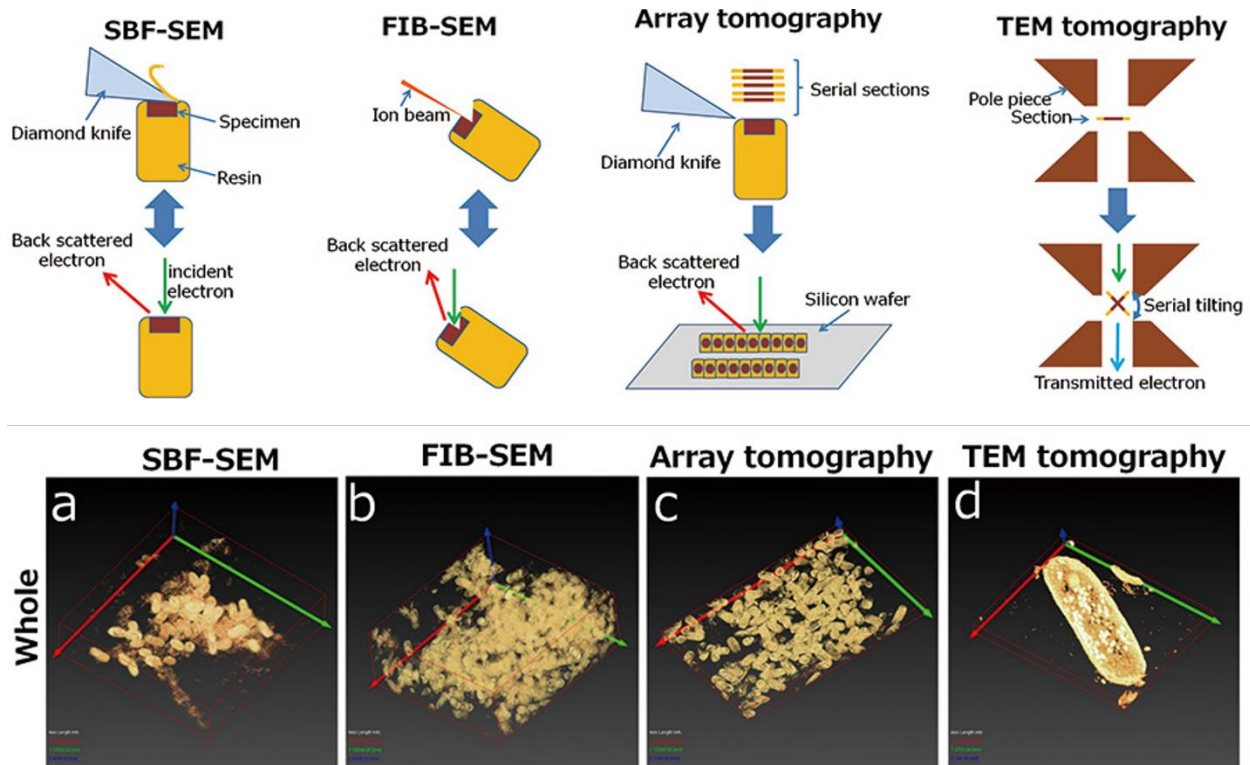
*Figure 8: Diagram of the different methods to produce a tomographic 3D-model in the SEM (SBF-SEM, FIB-SEM and Array Tomography) and in the TEM (TEM Tomography) and their subsequent 3D models (a-d)[106]*

### 3.4.1.  Micro-tomography

Tomography is an imaging technique using a penetrative ray to image multiple sections of a sample. It is used in multiple industries to form a 3D reconstruction of the internal components of 3D objects.[107–110] Computerised tomography (CT) scans can be used as powerful diagnostic tools for medical patients with internal injuries/diseases. A rotating x-ray source produces slices/cross sectional images of the patient's body. These are then stacked together to form a 3D image of the part of the body that is being imaged.[111] Electron tomography is analogous of this process. This is the same mechanism by which electron tomography is carried out, except the penetrative rays used are electron beams instead of X-rays. Electron beams are used in place of X-rays due to their much smaller wavelength as a consequence of the De Broglie wavelength of travelling electrons,[82,102] as mentioned above in the section 3.3. Electron Tomography is used to image the internal structures of biological samples (cells, tissues, primitive multicellular organisms) and can be carried out by an SEM or a TEM, as described by

Figure 8.[112,113] The ability of electron micro-tomography to acquire 3D information of the internal structure of a sample is limited by factors such as the thickness of the sample and the accelerating voltage of the electron beam used. The z-resolution of the images is entirely dependent on the thickness of the slices. Thickness of the slice can vary depending on the instrument used and the sample's material.[114] A microtome (diamond knife) must therefore be used to section a sample, encased in resin. The microtome can section the sample (in 10 to 200 nm)[115] within the SEM's vacuum chamber while imaging (Serial Block Face Tomography – SBF-SEM)[116] or before imaging by mounting the sample slices on a stub and then placed into the SEM vacuum (Array Tomography).[117] In place of a microtome, a small section of the sample can be milled away using a focused ion beam (FIB-SEM).[118] A TEM transmits the electron beam straight through the sample allowing a 2D view of the internal structures of the sample. Electron tomography using a TEM involves taking multiple electron micrographs at different sample tilt values (i.e. this doesn't involve the use of slicing the sample). Computational algorithms then reconstruct the sample's 3D internal structure from a series of projections obtained by multiple tilts. TEM tomography allows for a comprehensive and detailed representation of the sample's internal features in three dimensions.

### 3.4.2. Shape from shading

Four quadrant BSE detectors have the ability to capture compositional and topographic information simultaneously while imaging.[119] BSE (elastically scattered from atoms, as described by Figure *7*, above) are more likely to occur when the atoms on the sample being imaged are large (i.e. when the atomic number is high).
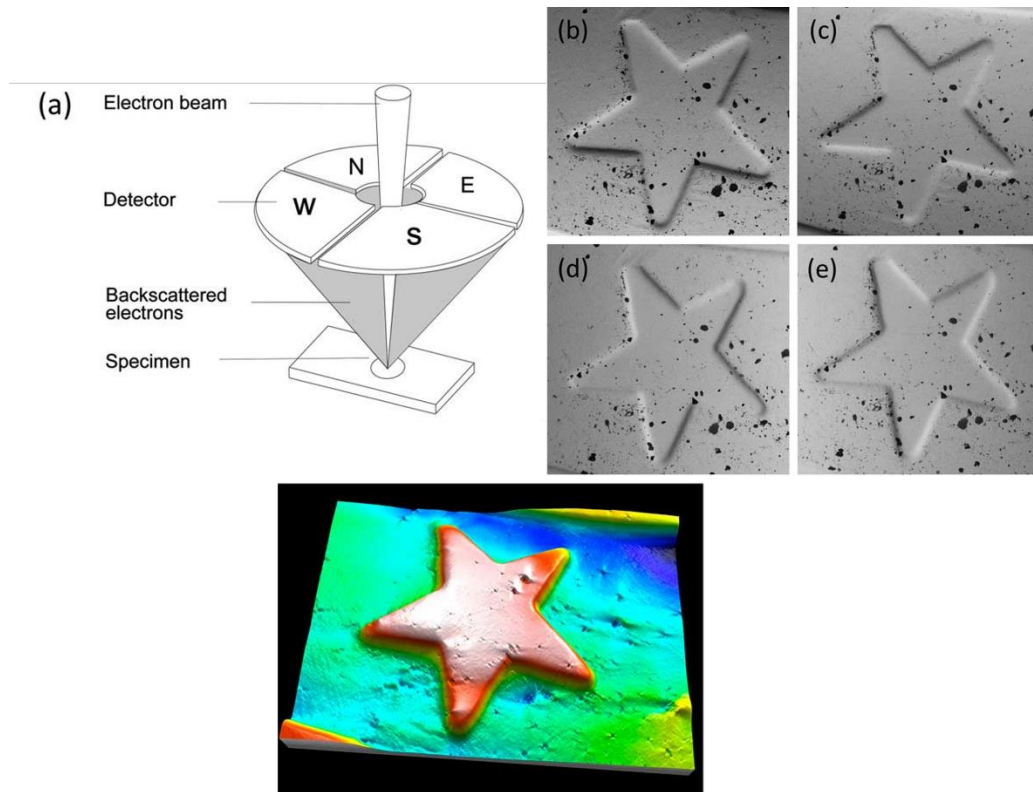


*Figure 9: (a) A quadrupole backscattered electron detector. (b-e) The images produced from each of the quadrants of the BSE detector. (Bottom) A 3D colourised model produced from a height map calculated from the images captured from the detector. Images sourced from: (http://dx.doi.org/10.1017/S1551929518000482)*

As the four quadrant BSE detector is split into 4 sections (as in Figure 9), each section views the same point at a slightly different perspective, which is analogous to the way in which our eyes perceive depth. This causes there to be shading on different sides of each image (Figure 9 (b)-(e)). This shading is seen as a local gradient/slope at each pixel. When opposite sides of the detector are combined as pairs (N-S and E-W), these slopes can be calculated. A height map can be produced through the integration of these local slopes. The height map is a grayscale image which represents the height of each pixel on the sample, with brighter pixels indicating higher elevations. The 3D modelling software utilizes adjacent point connecting

algorithms, combined with smoothing algorithms, to connect the height map data and create a 3D model of the sample.[120] However, there are several limitations BSE images to consider when using them as a 3D reconstruction tool. As mentioned in section 3.3, the BSE signal is sensitive to the atomic number (Z) of the material, so variations in sample composition could negatively affect the contrast and accuracy of the resulting 3D reconstruction. BSE do not provide the same level of surface detail of other electron interactions (such as SE1) as they originate from deep within the sample, as described by Figure 7. Also, quadrant detectors can incur significant costs on the researcher in terms of acquiring specialised hardware and training which may be prohibitive to some researchers.

### 3.4.3.   Stereoscopic 3D imaging

Stereoscopic imaging in SEM is a technique that which aims to replicate the depth perception in human vision by simulating the way our eyes perceive 3D objects, outlined in section 3.1. In stereoscopic SEM, two scanning electron micrographs are acquired from slightly different angles, mimicking two images being detected by human eyes. The two SEM images can then be combined digitally through anaglyph generation or by creating a stereo pair. The image can then be viewed using a stereoscope or other display system that allows each eye to see the corresponding image, creating a perception of depth. This method provides enhanced visual information about the 3D structure and morphology of samples. By perceiving depth, researchers can new insights into the surface topography. However, there are certain limitations to consider when using stereoscopic imaging in the SEM. The superposition of two images can lead to loss of fine detail and resolution, compromising the resulting image quality. Stereoscopic imaging requires specialised equipment such as a stereoscope or 3D display system, which may not be readily available or accessible for all. Additionally, getting optimal results with SEM stereoscopy requires expertise and training, as achieving the correct angle between the two images is complex and crucial. Lastly, 3D images produced by stereoscopy have a very limited field of view, limiting the comprehensive visualization of the surface structure and specimen.[121] SEM Stereoscopy is analogous to the work of Stefan Diller and **Nanoflight©** who produced very impressive 3D videos of micro and nanoscale samples. The videos show the user "flying" through the micro or nanoscale world, showing the complete

sample. This is not a common technique, however. Diller needed to procure specialised equipment in order to carry out these videos. The technique required a larger vacuum chamber to house a non-standard, 8-axis SEM stage as well as nine detectors, to capture multiple perspectives of the sample at the same time. The technique also required a lot of manual control over SEM parameters to ensure accurate images were being obtained. Therefore, this is a highly specialised technique which requires significant modifications and training to carry out.[122]

### 3.4.4. Photogrammetry in the SEM

As described in section 3.2, Photogrammetry is a process of extracting precise geometric measurements and generating accurate 3D models or maps from a collection of overlapping 2D images. With photogrammetry software only requiring two or more overlapping 2D images, standard SEM imaging can be used in place of digital photography, without requiring specialized hardware.[123] This is possible due to photogrammetry being based on matching keypoints between overlapping images and not being reliant on specific length scales or additional information about the camera or scene. This has already been attempted by a number of technique development researchers, such as: P. Kozikowski *et al.* who utilized paid photogrammetric software and an SEM to determine the diameter of relatively large graphite nanoparticles (hundreds of microns in size) or A.D. Ball *et al.* who used paid photogrammetry software to create a digital 3D model of a fly's head using an SEM and then used the 3D model to create a physical model of a fly's head through 3D printing for outreach.[123,124] These studies demonstrate the potential of utilizing photogrammetric software for reconstructing 3D models from SEM images. However, it is worth noting that these studies primarily focused on larger samples, which may not fully represent the microscale range typically observed in the SEM. Moreover, specific details regarding SEM and software parameters were not extensively provided in these works which can present challenges in replicating their findings.

## 3.5. Atomic Force Microscopy (AFM) and Limitations

The most common method of 3D model production of micro/nano scale samples is atomic force microscopy (AFM). AFM is a type of scanning probe microscopy which is universally used

due to its versatility. A cantilever with a sharp tip at the end is scanned across the surface, scanning the sample in the x, y and z directions.
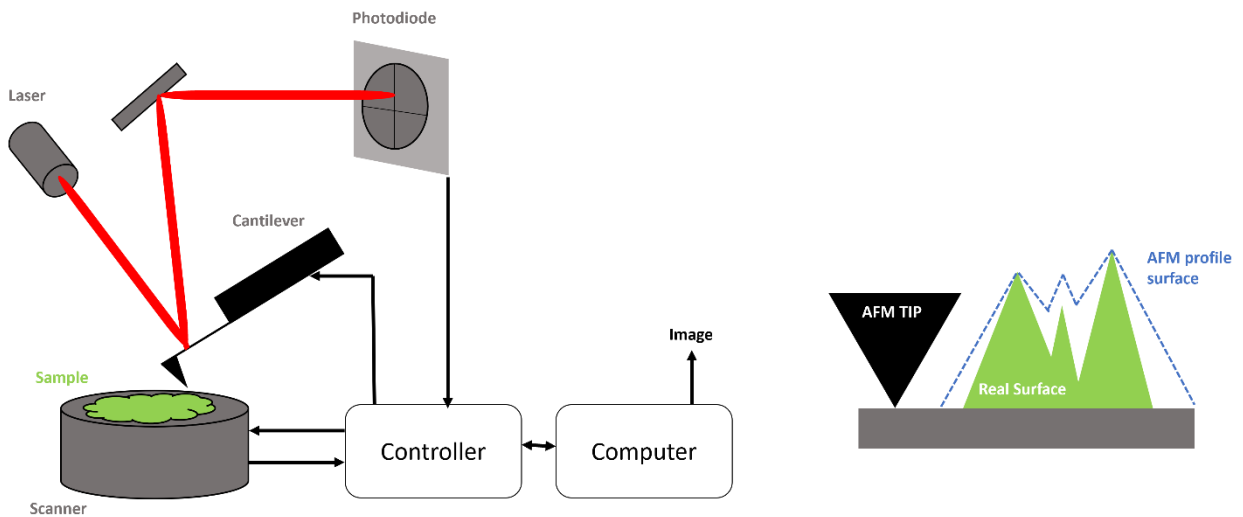


*Figure 10: Diagram of the main components of an atomic force microscope (AFM). (Right) the resolution limitation caused by the size and aspect ratio of the cantilever tip.*

The cantilever (which obeys Hooke's law) bends, when it comes in contact with the sample, deflecting a laser positioned on the back of the cantilever as outlined in Figure 10. The laser reflects from the back of the cantilever onto a photodiode. When the cantilever is deflected due to being in contact with the sample surface, so does the laser, reflected onto the photodiode. As the position of the laser on the photodiode changes, it produces a voltage. This voltage is sent to the z-piezoelectric element, via a feedback loop. This lifts the cantilever to follow the height of the sample, until it reaches a set point of laser deflection. If there is a pit in the topography, the cantilever descends to keep the set point constant. These ascents and descents in cantilever heights can be recorded and therefore the topography of the sample's surface can be accurately determined. In tapping mode, the cantilever is oscillated in order to read a change in amplitude. The feedback loop keeps the amplitude between the tip and sample constant. AFMs have a demonstrated resolution on the order of fractions of a nanometre. It has the ability to image with atomic resolution and is therefore well-suited for the characterisation of nanomaterials.

AFM is a versatile technique for producing 3D models of microscale samples due to its capability of operating in a variety of environments including ambient air, vacuum or liquid

environments, and its ability to image non-conducting samples, unlike in electron microscopy. It can operate in contact mode or non-contact mode, which involves deflection based on Van der Waals forces between the cantilever tip and the surface. Non-contact mode can be used with samples which may cause excess deflection when in contact mode, especially biological samples. However, AFM is also limited by factors such as z-piezo range, tip length and aspect ratio. (Figure 10, (right)) and by the feedback loop (how quickly the cantilever head responds to changes in height) to prevent tip-sample contact/separation. In addition, the imaging process can be sensitive to factors such as sample roughness. Uneven or rough samples can cause the AFM tip to deflect inconsistently, resulting in inaccurate height measurements, which will ultimately lead to distortions in the final 3D model. AFM also requires samples to be prepared on a flat clean surface, which can be impractical for certain types of samples[125–127]

# 4.   Aim of project

The aim of this project is to develop a framework for efficient imaging parameters in the SEM for use in the acquisition of photogrammetric datasets. Additionally, to increase the efficiency of this process, a predictive, mathematics-based, stage automation program will be developed to potentially decrease the time taken for the acquisition of the full dataset. Finally, these developed methods will be used to produce a 3D model of a microscale sample. The resulting photogrammetric microscale 3D model will then be compared against a microscale model produced via AFM.

The primary objective of this project is to establish a comprehensive framework for optimizing imaging parameters such as brightness, focus, astigmatism, position and depth of field. This framework aims to act as a guideline enhance the quality, efficiency and throughput of data acquisition, ensuring the acquisition of high-quality photogrammetric datasets that can be subsequently reconstructed into accurate 3D models.

In addition to parameter optimization, a key focus of this project is the development of a predictive, mathematics-based stage automation program. This program aims to automate the movement and positioning of the sample stage, which is the most time-consuming aspect of the data acquisition process. This program should streamline the data acquisition process, potentially reducing the time required to capture the full dataset. Furthermore, the developed method will be applied to generate a high-resolution 3D model of a microscale sample using the acquired photogrammetric dataset. Crucially, the photogrammetric software used should be open-source or the very least inexpensive. This model will serve as a valuable reference for evaluating the accuracy, cost-effectiveness, and reliability of the SEM-based photogrammetry approach. To provide a comprehensive analysis, the resulting microscale 3D model will be compared against a model generated using AFM. This comparison will allow us to assess the strength of the photogrammetry-based approach.

# 5. Materials and Methods

## 5.1. Scanning Electron Microscopy (SEM)

All microscopy work was carried out on the **Zeiss© ULTRA** and the **Zeiss© Supra** Scanning Electron Microscopes housed in the Advanced Microscopy Laboratory in Trinity College Dublin. The **Zeiss© Ultra** (made in Germany) has a **GEMINI©** class electron column, capable of sub-nanometre resolution.[94] This particular **Zeiss©** SEM is equipped with an SE2, In-Lens, ESB, STEM and EDX detectors.
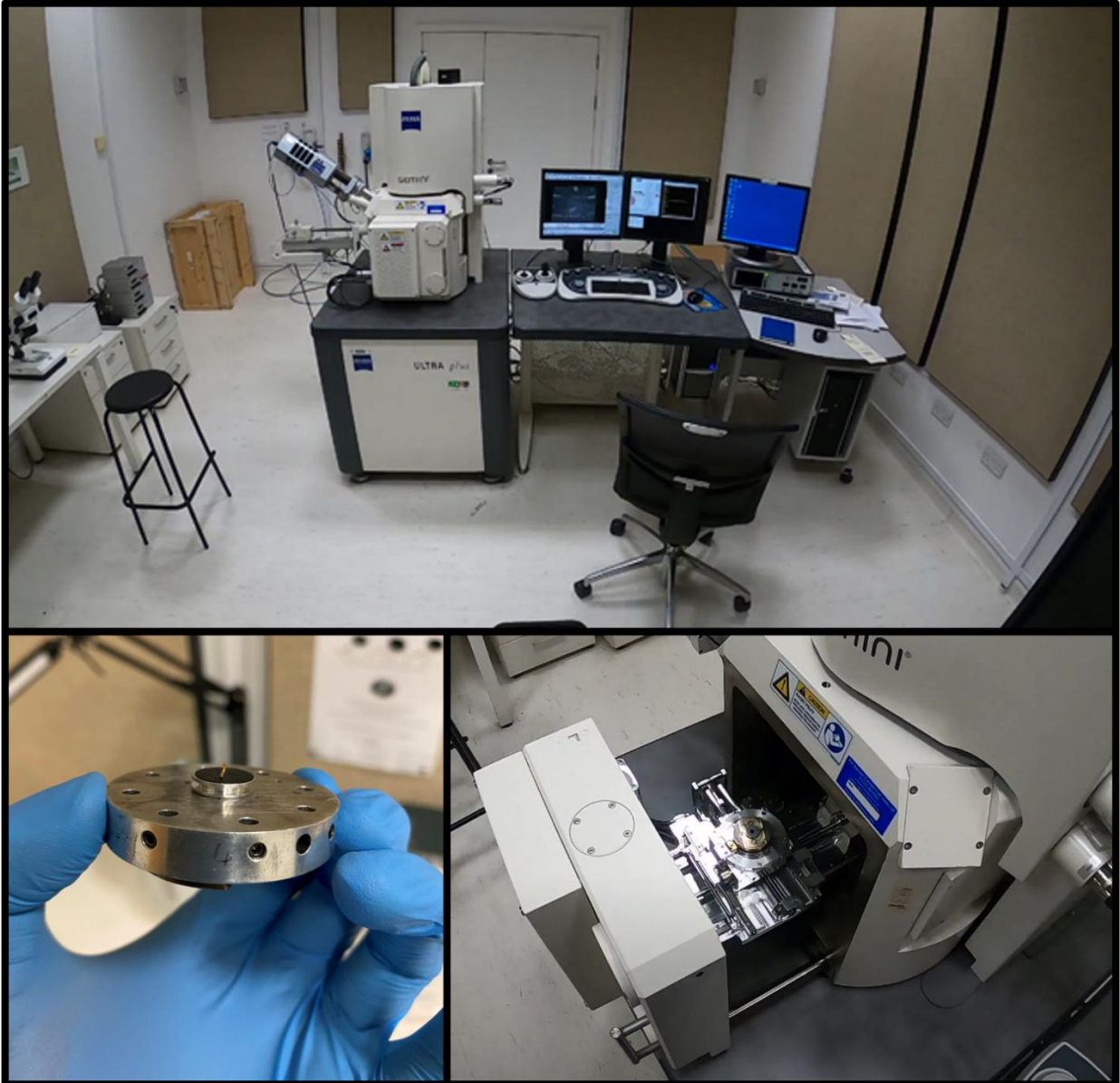
*Figure 11: Images of the **Zeiss© ULTRA** SEM (top) situated in the Advanced Microscopy Laboratory (AML) in Trinity College Dublin. (bottom-left) A stage carousel, with a single sample. (Bottom-right) the vacuum chamber door and the stage traversal system, where the stage carousel is mounted.*

Samples that were imaged were first cleaned and ensured to be conductive (Au/Pd sputtering, copper tape, Ag colloid) in order to be placed into the SEM vacuum chamber. Gloves were worn to ensure that the samples were protected from natural oils on the user's skin. Samples were affixed to stainless steel sample pin mounts (Ted Pella Ø12.7 mm and Ø25.4 mm pin mounts) by conductive sticky carbon tabs (Ted Pella Ø12.7 mm and Ø25.4 mm carbon tabs). The samples were further cleaned using a plasma cleaner and then placed into the slots on the stage carousel, as seen in Figure 11(bottom-left) and tightened using the tightening screws on

the left of the carousel. The vacuum chamber was vented, using the Zeiss SEM software on a Dell desktop computer, to allow for the vacuum chamber door to be opened. The carousel was turned upside down and shaken lightly to ensure the entire sample had adhered to the carbon tab and therefore prevent any unwanted materials contaminating the vacuum pump. The carousel was then secured to the sample stage, inside the vacuum chamber. The door was closed, and the air was pumped out of the vacuum chamber. Once the vacuum was pumped to the standard vacuum level (approximately $5x10^{-6}$), which took roughly 5 mins to complete, the software allowed for the Extra High Tension (EHT) to be selected and turned on. This allows the electron gun to begin to produce an electron beam. From here the sample was positioned in the x, y, rotate and tilt axes using the SEM software, or the joystick seen in Figure 11 (top). The sample was moved higher in the vacuum chamber using the z-stick and camera inside the chamber, to ensure an appropriate WD (or the distance from the objective lens to the sample when the sample is in focus) could be reached, without colliding with the pole piece. The focus/astigmatism/alignment/brightness and contrast were corrected using the SEM control panel. Any imaging parameters (accelerating voltage/apertures etc.) were changed or selected using the **Zeiss© SmartSEM** software. Once adequate imaging parameters had been reached, the scan speed was slowed to decrease the signal to noise ratio and the micrograph of the sample was captured. Micrographs were then saved to the desktop computer, which were subsequently saved onto a USB drive.

### 5.1.1. Dynamic Focus

Dynamic focus mode prevents the defocus on the edges of the electron micrograph during tilting. This parameter was turned on using the **Zeiss© SmartSEM** software. The "Dyn. Focus" checkbox was ticked. The "frame corrected focus (FCF) setting", which sets the degree of dynamic focus, slider was adjusted until an optimum sharpness across the entire image was achieved.

### 5.1.2. High Current Mode

High current mode is utilized to boost the sample's depth of field, through doubling the beam's current. This was turned on using the "High Current" check box on the "Apertures" tab on the **Zeiss© SmartSEM** software.

## 5.2. Sapphire Dome Samples

Aurivillius phase thin films, also known as Sapphire Domes, were produced by L. Colfer from the Keeney group in the Tyndall Institute, Cork. The sample is a rare example of a room temperature (RT) magnetoelectric multiferroic[128,129], that have potential for future application in memory storage devices where 2D ultra-thin film that are phase-pure could produce up to 8 different logic states.[130] The discovery of various topological structures in $Bi_6 Ti_{2.9} Fe_{1.5} Mn_{0.6} O_{18}$ (B6TFMO) such as charged domain walls and exotic polar vortices[131] means the material has potential for use in nanoelectronics, discrete memory storage technologies[132] and domain wall device applications. The B6TFMO, which produces microscale dome like structures, was grown by a direct liquid injection chemical vapour deposition (DLI-CVD) technique on a sapphire substrate. This sample was chosen for this project as the domes on the sample surface are crystalline in structure and have a high degree of roughness.

## 5.3. AFM Data

The AFM images were obtained in the Tyndall institute, using a Veeco Multimode V instrument in AC Tapping mode. The instrument, produced in the United States, is a desktop scanning probe microscope, capable of sub-nanometre resolution. It is a so-called multimode instrument, as it can act as an atomic force microscope (AFM), a magnetic force microscope (MFM) or scanning tunnelling microscope (STM), depending on the researcher's needs. The images were performed by L. Colfer, using a tip (AC160TS-R3), with a radius of 7 nm.

## 5.4. Photogrammetry Regime (Macro and Micro scale)

Once a subject to be reconstructed into a digital 3D model is decided upon, an imaging regime must be established. On this, there are two main methods of capturing a photogrammetry dataset of a subject, depending on its size. Photogrammetry of large objects (terrain or buildings) requires the movement of the camera, while the lighting and the subject stays motionless (parallel axis capture). This was demonstrated by obtaining a photogrammetry dataset of a tree stump, shown in Figure 3. Once the tree stump was identified as the subject for reconstruction. Good lighting was ensured by taking the dataset on a clear day. The camera that was chosen was an **iPhone©** 11 smartphone camera. 28 images were captured at multiple

different elevations and perspectives by walking around the subject with the camera and capturing images. The resulting images were then input into photogrammetry software.

In contrast, photogrammetry of micro-/nanoscale objects (models or artefacts) involves the camera remaining stationary and moving the object in a fixed manner (convergent axis capture). The shadow of the user/camera can interfere with the acquisition as they move around the small object. Therefore, lighting must therefore be kept constant and diffuse across all surfaces of the object. Constant lighting prevents false points being counted by the SIFT algorithm, due to an excess or insufficient amount of light falling on a single side as it is being rotated. In the macroscale this can be carried out with a fixed camera (which can alter its height) and a turn table (which can rotate the subject). This is the same mechanism by which the SEM can obtain a photogrammetry dataset as the electron beam is in a fixed position. The sample is moved via a sample stage, which translates the sample in the x, y and z directions. A data set of the sapphire dome sample was captured by obtaining a hemisphere of coverage around a decided-on point on the sample surface. 96 images were captured at as many different perspectives of the sample as possible. Different perspectives were captured using the SEM sample stage. The sample stage was rotated by 360° through 20° increments at tilt angles of 0°, 10°, 20°, 30°, 35° and 40°. Increased tilt values above the 40° value were not used as the sample stage was at risk of colliding with the microscope's pole piece. Images were captured at each of these points using the method outlined above. Following each tilt or rotation, the sample stage required reorientation to the point of interest, by adjusting the x and y position of the stage. At each new viewpoint, the brightness, contrast, astigmatism and focus were checked and adjusted where necessary. The entire acquisition of the dataset was completed in two microscope sessions each lasting 3 hours, totalling 6 hours of microscope time.

## 5.5. Photogrammetry software

The photogrammetry software that was to be chosen was first researched. The software candidates were broken down and compared on their affordability, if they had user limits and if they required the use of a GPU to be used. The software which was chosen was **Meshroom©** made by Alicevision. It was installed and used on a HP Omen laptop, containing an **Nvidia©**

RTX 3060 laptop GPU. Once the dataset was obtained, the SEM images were input into the software. At this point, the user can select an appropriate algorithm mix to use for processing the images. The user interface of the software allows the algorithms to be interacted with via. a node-based graph structure, where each node represents an individual algorithm. The user can modify the settings on each node to achieve the desired result for the reconstruction.

## 5.6. Stage Automation

In order to speed up the process of dataset acquisition, a mathematics-based predictive stage position program was conceptualised. The most time-consuming part of the dataset acquisition was identified as being the movement of the sample stage in x and y, after rotating or tilting, in order to re-centre the point of interest. It was noted that the SEMs raster mechanism of image capture slowed this process down considerably. Therefore, the mechanisms by which the sample stage moved (i.e. x, y, z, rotation and tilt) were studied and translated into movement vectors in a 3D Cartesian plane. Then, using the Python programming language, a program was written in order to predict the locations, in x, y, rotation and tilt.

# 6. Results and Discussion

This section provides an overview of various experiments and analysis carried out during this project. It highlights the distinctions between photography for macroscale photogrammetry and scanning electron microscopy for microscale photogrammetry. The discussion then delves into the selection into the selection of optimal detectors and microscope parameters to maximise the resulting photogrammetric 3D model. Additionally, it explores the significance of stage automation in streamlining the data acquisition process. The section also outlines the step-by-step procedure for obtaining a photogrammetric dataset and generating the corresponding 3D model. Finally, a comparison is made between the 3D model obtained through photogrammetry and the AFM data acquired from the same sample, facilitating an assessment of their respective attributes.

## 6.1. iPhone Data

As reported in Figure 3, a dataset of a tree stump was obtained using the camera on an iPhone 11. This was completed as a test for the software on a subject in an environment that it is designed to produce 3D models in. Secondly, the 3D model of the tree stump was reconstructed to create this figure to visually explain how the photogrammetric algorithms work in terms of overlapping images.

## 6.2. Scanning Electron Microscopy

As the Ultramicroscopy research group is not a synthesis research group and is mainly focused on technique development, samples that were to be 3D characterised were sourced from other research groups. A general call for difficult to image/rough surface features was put to research groups in need of more information from their sample's surfaces. As well as this, a number of everyday metal household items were obtained for ease of imaging, due to their conductive material's nature. (i.e. a 10 cent coin, broken safety pin (ductile metal fracture surface), broken sewing needle (brittle metal fracture surface) and a shaving razor).

Because photogrammetry modelling software packages are produced, optimised and calibrated for DSLR optical cameras in either close-range or aerial photography, then the SEM's parameters and imaging regimes must mirror those of a normal optical photogrammetry data

acquisition regime. Photogrammetry of large objects (terrain or buildings) requires the movement of the camera, while the lighting and the subject stays motionless (parallel axis capture).[133] This is contrasted with photogrammetry of small objects (models or artefacts) where the camera remains stationary, and the object moves in a fixed manner (convergent axis capture). This is because the shadow of the user can interfere with the acquisition as they move around the small object. Lighting must therefore be kept constant and diffuse across all surfaces of the object, to ensure no false points are counted due to an excess or insufficient amount of light falling on a single side as it is being rotated. Each of the parameters (Detectors, Brightness/Contrast, Depth of field, Focus/Astigmatism, Stage location, lighting effects etc.) of the SEM must therefore be carefully considered.

### 6.2.1.  Lighting Effects

Lighting effects must also be taken into account when acquiring a photogrammetric dataset.
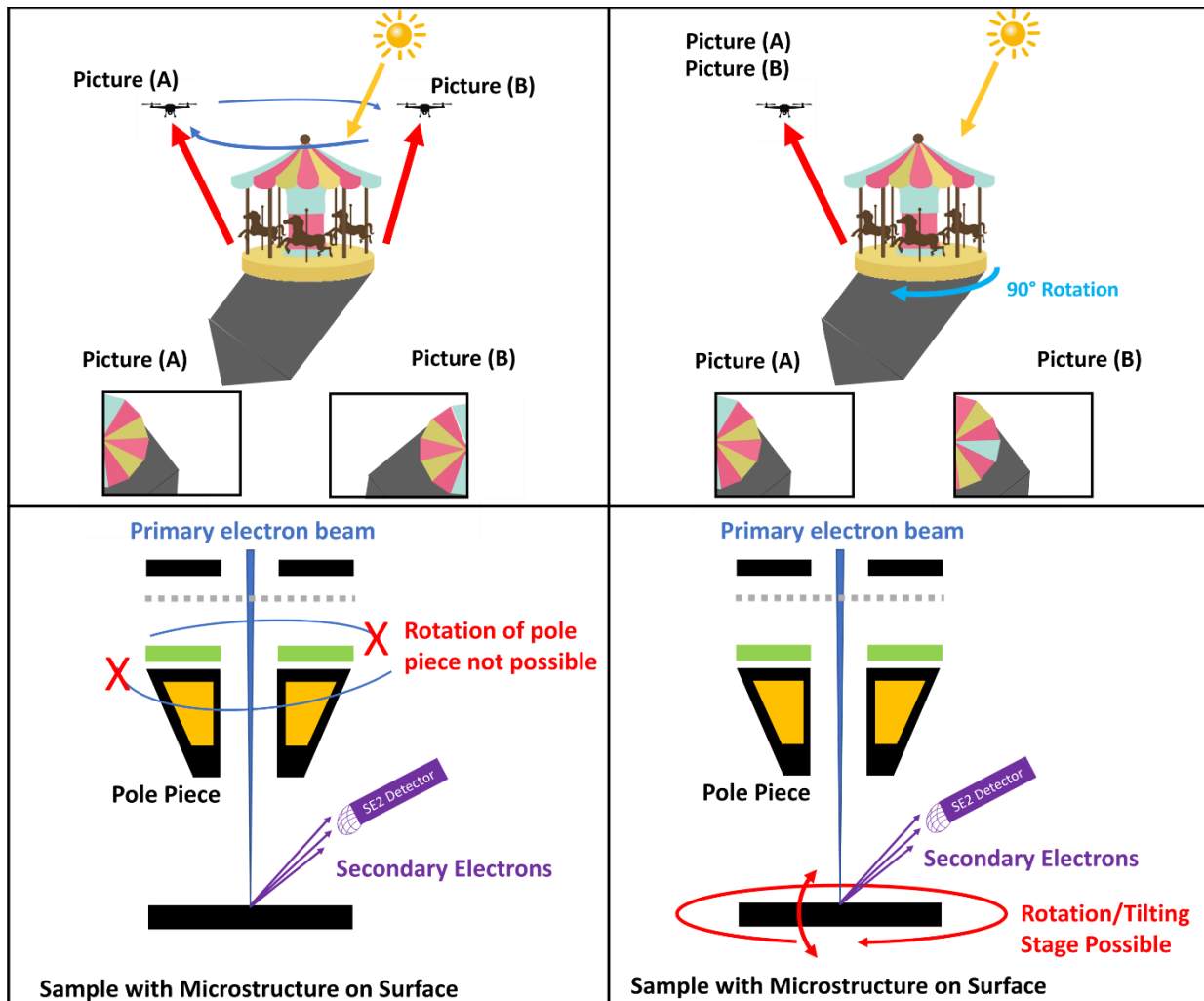
*Figure 12: The comparison and differences of macroscale and microscale photogrammetry capture. The top row describes the two methods by which a subject could be captured in the microscale. The bottom row describes the same method but instead using the SEM.*

A comparison between macro and micro scale photogrammetric acquisition is described in Figure 12. The different methods by which photogrammetric datasets are captured in the macro scale are compared against each other and how they contrast the photogrammetric dataset acquisition techniques within the SEM system. In Figure 12 (top-left), parallel axis capture is described by a sensor (camera drone/UAV) performing multiple image capture (picture A and B) by flying over a large object (Carousel). The light source (Sun), at an oblique angle, casts a shadow on the carousel's opposite side. From the pictures taken (A + B), the shadow and the carousel keep their position, allowing the SIFT image matching algorithm work

to match chosen points up based on their relative intensities, which can be seen in Figure 4 in the introduction. This is contrasted against Figure 12 (top-right), the convergent axis capture technique, where the sensor stays static and the object is rotated through 90° degrees. Here, the shadow cast stays static but the object rotates, as seen by the cyan triangle rotating into the shaded region. Because the cyan triangle is now in the shaded region, its relative intensity value has now changed between picture A and picture B. This will hinder the SIFT algorithm's ability to match these two points together and therefore disorient the rest of the workflow. These two situations are compared with the SEM system. In Figure 12 (bottom-left) the sample is being imaged by an electron column which can alternate its angle of attack. This is compared to the macro imaging example of the drone flying around the object (Figure 12 top-left). This would be the ideal solution, considering the position of the SE2 detector, at an oblique angle to the sample. No such system exists currently however, due to the complexity of moving the electron column (vacuum, lenses, detectors etc. in the way) and for the reason that it is much easier, for general use, to move the sample on a moving sample stage. A moving sample stage with a fixed SEM column is the method by which the SEM operates in the real world and is described in Figure 12 (bottom-right). In the figure and in all real-world SEMs, sample stages are motorised and can move in 5 ways (x, y, z translations, tilt, and rotation) allowing for objects of interest on the SEM stage to be positioned under the beam. This is analogous to the macro example (Figure 12 (bottom-right) where, in place of the sun, the light source is the SE2 detector and the sensor, in place of the camera drone, is the electron beam.

### 6.2.2.   The Edge Effect

Because of the position of the SE2 detector, relative to the electron beam, the so-called "edge effect" causes signal intensity differences at changes in topography. In other words, vertical sections of the sample surface pointing towards the SE2 detector collect more signal than those pointing away and thus these regions are bright, while the regions pointing away are darker.
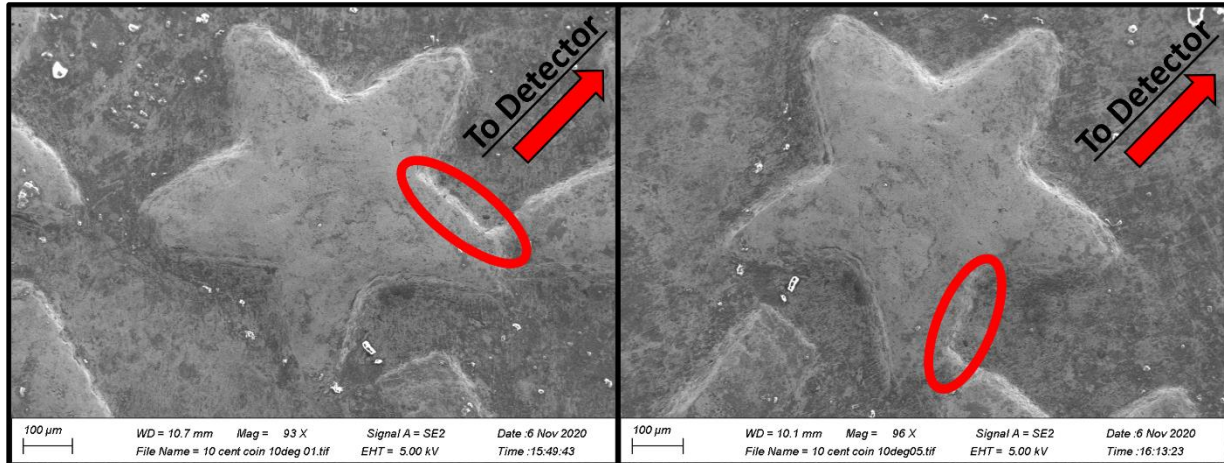
*Figure 13: SE2 E-T detector images of the star on a 10 cent coin. The red circle on the first image (left) shows the position of signal intensity, due to the position of the detector. The next image (right) shows the same location but with much less intensity. The red arrow shows the direction of the SE detector.*

In Figure 13, the edge effect on the topography of the star on a 10 cent coin is illustrated by identifying the particular edge (red ellipse) which has extra intensity (higher contrast). This is caused by the identified edge being in the direction of the SE2 detector/SE detector. As outlined in section 3.3, SEM gains topographical contrast from a number of contrast mechanisms working in tandem. Surface-tilt and shadow contrast contribute to the so called "edge effect". The edge effect is a result of the interplay between of the variations of SE emissions from different inclinations on the sample surface and the path of flight of these electrons towards the detector. When an edge is facing the detector, a greater number of electrons will be detected compared to when the edge is facing away from it. This sample is then rotated by approx. 40 degrees, clockwise (Figure 13(right)), turning the identified edge away from facing the SE detector. In this location, the identified edge is now pointing away from the detector, reducing the intensity. This effectively casts a shadow on this location by the electron flight pointing away from the detector. This is analogous of the macro scale example described in Figure 12. The SIFT algorithm therefore has difficulty matching the distinguishable intensity of the identified edge between the two images. Therefore, to ensure that the photogrammetry software is not confused by these high intensity regions moving a different detector must also be considered.

### 6.2.3. Detector Choice

As mentioned in the introduction (and in Figure *7*), the electron beam can interact with a sample's atoms in a number of ways. These interactions produce different signals with inherent information attached to them. This information's relative intensity can be used as contrast to form an image. SEMs are therefore fitted with a number of different detectors to catch particular signals which are being emitted from the irradiated sample. Each detector has a different method of obtaining their signal from the sample's surface, therefore choosing the detector has implications for the final photogrammetric dataset.
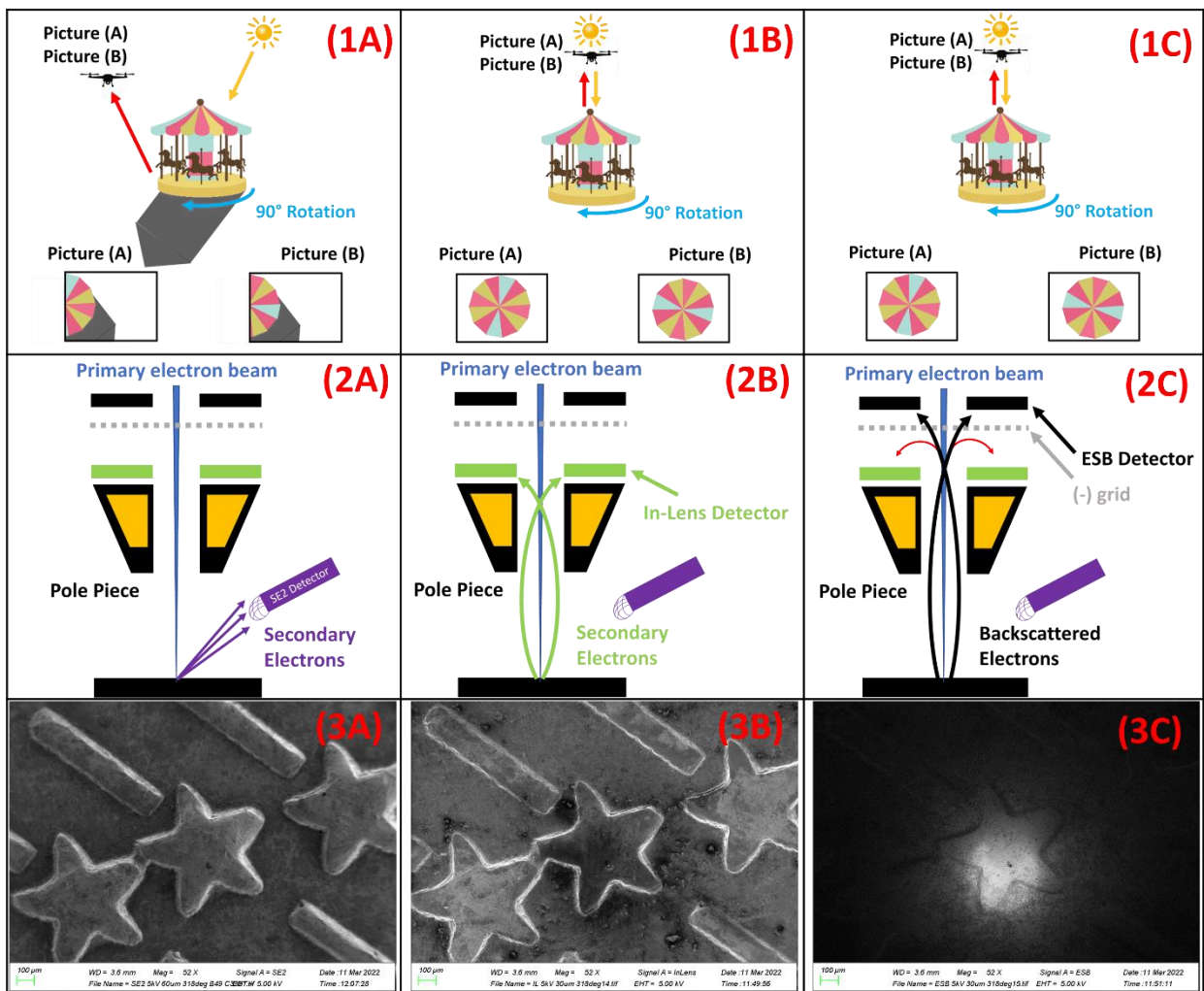


*Figure 14: (Top row) The analogous macroscale methods of capturing a photogrammetry dataset of a subject using a drone. (Middle row) Method (to the macroscale) of capturing a photogrammetry data with different detectors: (left to right) SE2, In-lens, ESB. (Bottom row) Sample images of a star on a 10 cent coin, captured by different detectors: (left to right) SE2, In-Lens and ESB detectors).*

The E-T detector is the most commonly used detectors by SEM operators. This detector would be attractive to a user trying to obtain a photogrammetric data set due to its ease of use and huge signal availability (detects SE1, 2, 3 and BSE). The E-T detectors, being at an oblique angle to the sample's surface, detects SEs asymmetrically from the sample's surface. For this reason and the so called "edge effect" of shallow emitting SEs, an increased number of SE are detected at vertical edges and edges which are facing it. This causes an increase in brightness when imaging in these regions, due to excess emission, and a shadow at the surface structures facing away from it, due to reduced emission. This can be seen in Figure 13. Where one side of the star (right) on the 10 cent coin is illuminated whereas its opposite side is not. This is analogous to a macro/aerial photo being taken of an object on the surface of the earth, at sunrise/sunset i.e. when the sun is at an oblique angle between the sensor (camera) and the object. This is demonstrated in Figure 14 (1A) where the Sun is illuminating the object (a carnival's carousel) at an oblique angle, causing a shadow. The sensor, a camera UAV/drone, is imaging the object directly above it. This can cause issues for imaging as the relative intensity for the SIFT feature matching algorithm is stays on the same side of the carousel as it rotates i.e. the blue triangle rotates into the shadowed region making it difficult to pinpoint between the two images. This is contrasted to the In-Lens and ESB detectors. These detectors gather electrons in the electron column, as described in Figure 14 (2B+2C). In modern SEMs the two In-Lens detectors are generally placed in parallel to each other along the beam axis. The In-Lens SE detector very efficiently collects SE1 type SE. SE1 electrons are produced very near the upper region of the interaction volume and therefore contain the most surface detail of all SE types.
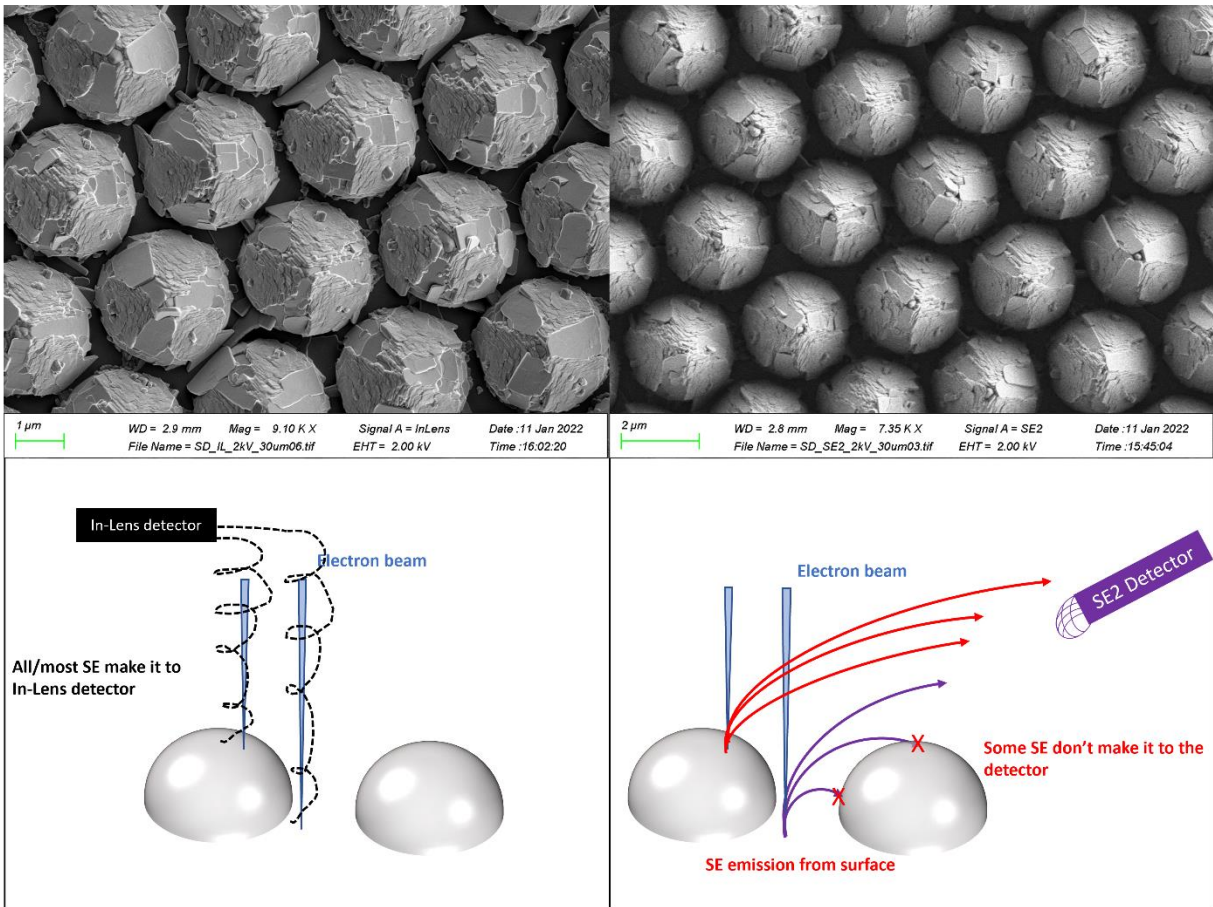
*Figure 15: Comparison between In-Lens (left column) and SE2 (right column) methods of SE collection to cause differences in surface contrast while imaging a Sapphire Dome sample.*[134]

In-Lens detectors capture electrons from a top-down perspective from the sample's surface and therefore do not produce overly bright or shaded regions on either side. This allows for electrons to escape from deep portions of a sample and allows for better contrast in hard-to-reach areas. Figure 15, which shows a sapphire dome sample being imaged using the In-Lens SE detector (left) and the ET-SE detector (right), demonstrates this phenomenon. In the SE2 detected image, there are voids of information in the sections between individual domes. This is due to an interruption in the produced SEs flight towards the detector, caused by another dome getting in their way. In Figure 15, where the SEs produced in the space between domes have their flights toward the ET-SE detector interrupted. This lack of signal produces the shaded/dark regions of the SE2 detected image (right). This is compared against the In-Lens image (left) where the contents of the sections between each dome are clearly visible. The In-Lens detector collects SEs along the axis of the beam just above the objective lens. Thus, no

signal is blocked by the sample surface, allowing the full surface to be in a modest contrast range. This uniform contrast across the full surface, helps build up a clear structure for the photogrammetry software to work with.

### 6.2.4.   Brightness and Contrast

In an electron microscope, as outlined in section 3.3, the contrast of the micrograph originates from several contrast mechanisms, which originate from beam interaction with the sample. The contrast can be influenced by a mix of beam parameters, sample interactions, the nature of the signal and the position and response of the detector. As described in section 3.3, topographic contrast shows brighter portions at vertical inclination of surface structures, due to the edge effect (Figure *7* and Figure 13). Therefore, steep portions of the sample, pointing towards the detector (easier electron flight), are brighter than those steep portions pointing away. Therefore, careful choice of detector and parameters is key to ensure brightness and contrast is optimised to avoid data loss and ensure that images taken have significant overlap to ensure the most efficient key matching.
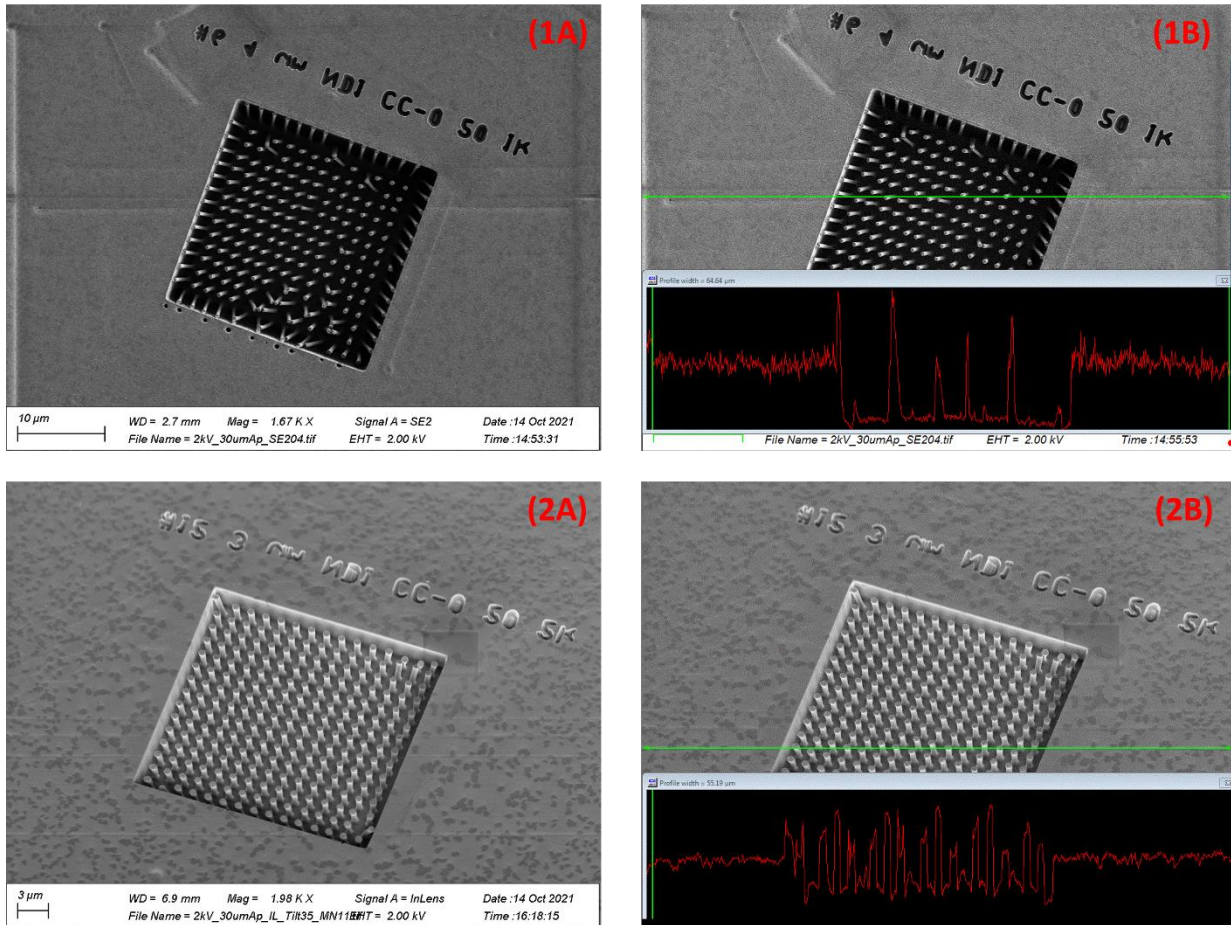
*Figure 16: Comparison of using two different detectors, SE2 (1A + 1B) and In-Lens (2A + 2B) and different contrast and brightness values on a PEG nanopillars sample in the SEM, which is represented by a histogram (1B, 2B) of the signal intensity for a particular raster line (green line).*

Described in Figure 16 is the difference that changing a detector can do to the signal received by the SEM software. As mentioned in Figure 14, above, the SE2 detector is placed on the lateral wall of the SEM vacuum chamber wall. This can cause regions of low or high contrast depending on the topography of the sample. This can be seen in Figure 16(1A), where the SE2 signal inside the pit is lost due to the inability of the electrons to fly towards the detector. Contrarily, the top of the nanopillars show a large signal intensity which also causes the loss of information. This supported by the signal histogram in Figure 16(1B), which shows the signal intensities which is being displayed for a particular raster line (green line in Figure 16) Changing the contrast/brightness on an SEM is done by changing the gain on the pre-amplifier, which amplifies the signal before being digitised. Changing the brightness on the SEM translates the histogram in the y-direction on its graph. Changing the contrast on the SEM changes the

relative size of the peaks and troughs on the histogram (i.e. increases the amplitude of the intensity peaks). Incorrect brightness or contrast settings can lead to loss of surface features through the oversaturation or the bottoming of signals, which is evident by Figure 16 (1B), as the histogram's peaks and troughs are outside the graph area. This loss of data can cause issues for the photogrammetry software to properly understand the geometry of the scene. This is contrasted with Figure 16 (2A and 2B) which are In-Lens images where the brightness and contrast has been corrected to ensure that no data is lost through a lack of or too much intensity. What results is a much clearer, more resolute image. In this image the surface of the bottom of the pit, that the nanopillars sit in, can be clearly seen. The bottom of the pit is now not devoid of information, and the bottom can be made out. Also, the surface of the top of the nanopillars are also well defined and not oversaturated. These images would be far superior candidates for the image matching algorithm of the photogrammetry software, as there is much more surface information retained for key points to be matched to each other. This is supported by the histogram of this image Figure 16 (2B). In this histogram, the brightness and contrasted has been corrected to ensure that the peaks and troughs are not out of the graph area, giving a graphical representation of data retention.

### 6.2.5.  Contamination and Dwell time

Due to the considerable number of images needed to obtain a 3D model of adequate quality, the number of times the raster scan therefore passes over a tiny unit squared spot on the sample is considerable. Depending on the sample type, the surface can fail to dissipate the electrons it is being bombarded with. This is especially evident in insulating samples where electron build-up occurs on the sample surface (Since the electrons fail to be grounded). The build-up of electrons causes a localised electric field on the surface, which can influence the trajectories of the primary electron beam and signals produced by the sample-electron beam interaction. This can cause a large intensity spike seen at the detector and significant image distortion.[135] A significant dose of the electron beam can also cause radiolysis on sample surface.

Even with conducting samples however, when exposed to large electron beam currents, a number of interactions can affect observed contrast. These include sample charging, which

should be prevented to minimise electron scattering and beam induced heating. Moreover, radiolysis effects can occur, which can cause structural alterations or cause mass loss of the sample. Additionally, the deposition of contaminants arising from ambient hydrocarbons (i.e. from a dirty sample or vacuum) can obscure or distort the electron micrograph.[136]
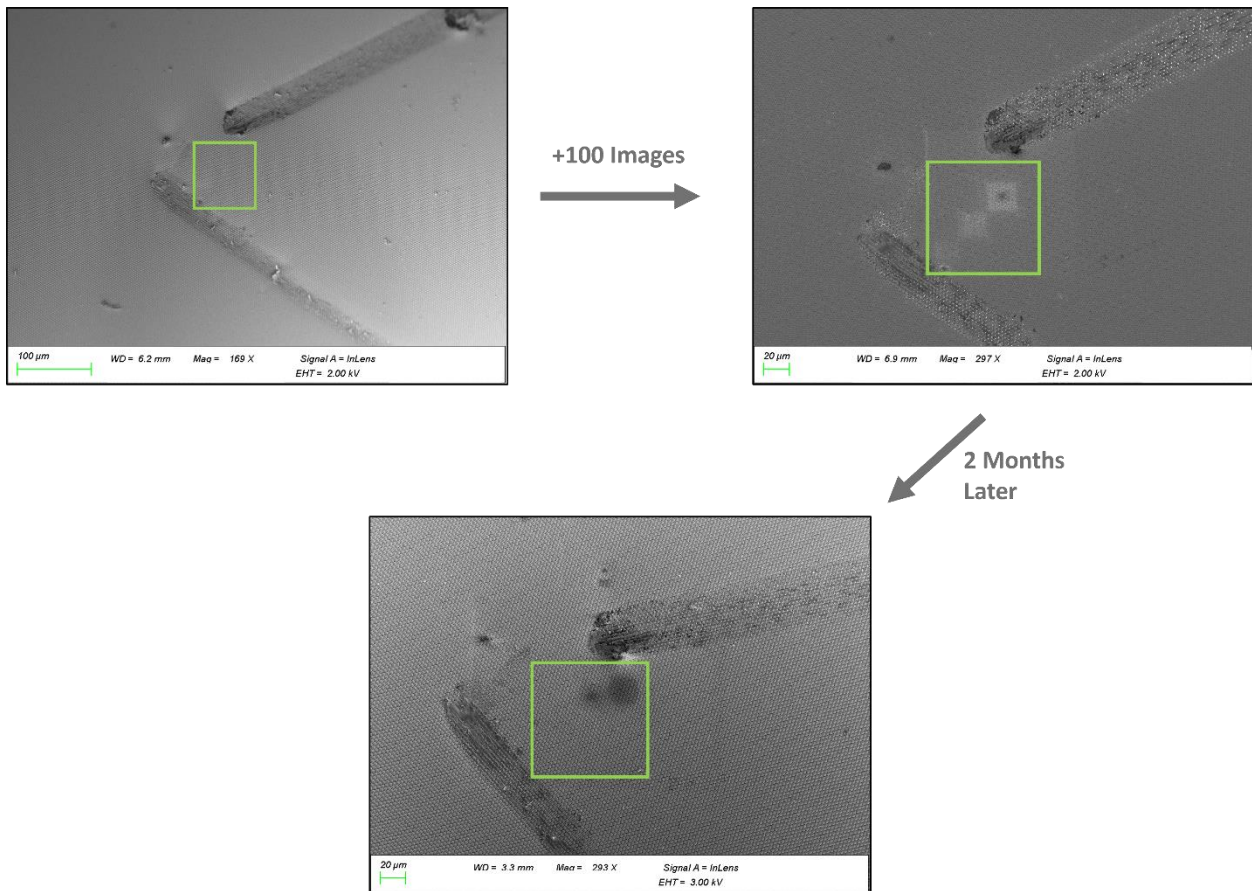


*Figure 17: The consequences of contamination as a function of dwell time of the electron beam on the sample surface. (top-left) 1$^{st}$ Image of Sapphire Dome sample, (top-right) image of the same area after a photogrammetry dataset acquisition and (bottom) an image showing the lingering contamination 2 months after the sample had been initially imaged.*

Outlined by Figure 17 is the implications of beam time on a sample, where a permanent change in sample surface can be seen in the contrast given back from it. The green square shows the result of the sample after a long period of beam exposure (right) due to taking many (100+) images of the subject of interest. It highlights the bright squares (relative to the rest of the surface) on the surface that are produced by the beam being rastered over the sample's surface. These blemishes are a function of a "dirty" vacuum or sample, because of unwanted particles/molecules in the sample chamber or on the sample itself. This is due to improper

handling and/or cleaning of the sample or unsuitable samples being placed into the sample chamber and through the use of an inadequate (non-ultra high) vacuum. Hydrocarbon gas molecules (oils) present in the chamber or on the sample drift near the electron beam. When the molecule and the electron beam interact, the molecule becomes positively charged, due to the electron beam knocking electrons from the molecule's orbitals. The electron beam, a stream of negatively charged particles, causes the sample surface to be negatively charged, thus causing an attractive force between the sample and the hydrocarbon molecule. The hydrocarbon molecule therefore deposits onto the sample surface and causes this change in brightness/contrast.
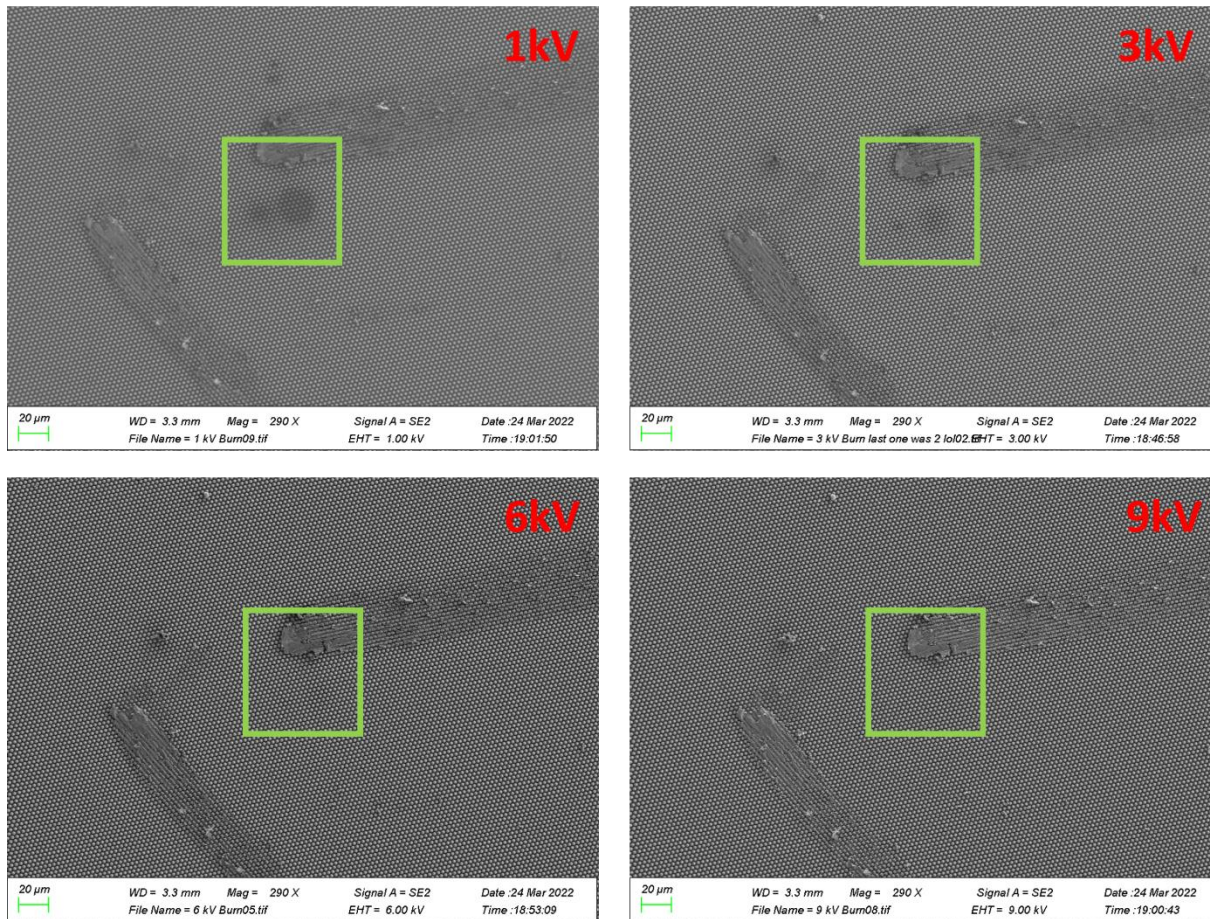


*Figure 18: A comparison between the visibility of the contamination on the surface (green box) and the accelerating voltage (red writing). The figure shows a decrease in visibility of the contamination, which correlates with an increase in acceleration voltage.*

This can be negated by increasing the accelerating voltage, which is known to penetrate deeper into the sample[137] and passing straight through the deposited material. As reported in

Figure 18, by increasing the accelerating voltage, the electron beam penetrates deeper into the sample, passing by the carbon/hydrocarbons which have been deposited onto the surface. However, this also has the effect of lowering the surface sensitivity of the SEs/ reduce the number of surface electrons and therefore lose the high surface resolution of a lower accelerating voltage. This is due to the beam producing BSEs/SEs deeper within the bulk of the sample. Thus, a trade-off between high surface sensitivity and high deposition amounts must be accounted for/ considered.

This surface damage (commonly termed raster burn/deposition) generally worsens with prolonged exposure and with a decreased spot size/higher magnification (due to increased intensity per unit area). This causes the subject of interest to become darker and darker as the sample is continuously imaged for a photogrammetric dataset. This could cause an issue for the photogrammetry point matching algorithm as the subject of interest's brightness/contrast changes between images being acquired. Various measures can be undertaken to ensure sample hygiene throughout the SEM imaging process. Cleaning the sample's surface using ultrasonic, solvent and/or plasma cleaning techniques can mitigate the issue of a dirty sample. Also, an ozone plasma cleaning apparatus can be employed to help maintain cleanliness within the vacuum chamber. It is important to take steps to maintain cleanliness of all aspects of the analysis before, during and after to ensure any imaging artefacts are avoided, resulting in reliable imaging results. This will be discussed further in future work.

## 6.3. Image acquisition and preparation

Like acquiring a dataset for a macro scale object (carousel in **Error! Reference source not found.**) a dome of overlapping image coverage must be obtained to ensure a good 3D model is reconstructed. Thus the "flight" and imaging path of the electron beam must be carefully considered before imaging takes place. For aerial photography, a number of software/tools (**PIX4Dcapture©**, **SkyDrones©** etc.) exist to help the UAV/drone pilot to plan flights along a geographical topography. For individual object capture it is recommended, by photogrammetry software providers, to obtain a hemisphere of photo coverage around the object, using different values of elevation and azimuth. This may involve the use of a drone for large objects such as buildings or handheld cameras and small objects. For micro scale

photogrammetry the stage rotation allows for different "azimuth" values and the tilt allows for different "elevation" values, for the hemisphere of coverage.

### 6.3.1. Eucentric Point acquisition

The Eucentric point (EP) of an electron microscope stage is the point where the sample does not move off the field of view, when the stage is tilted or rotated. This is a convenience feature in dual beam FIB-SEM, which ensures the feature of interest remains at the same position under the electron beam at different values of tilt. In terms of rotation, the EP allows the centre of the screen to function as the centre of rotation.[138] For this project, the EP of the sample stage is sought after in order to easily acquire multiple images at different values of tilt and rotation for a 3D model reconstruction.
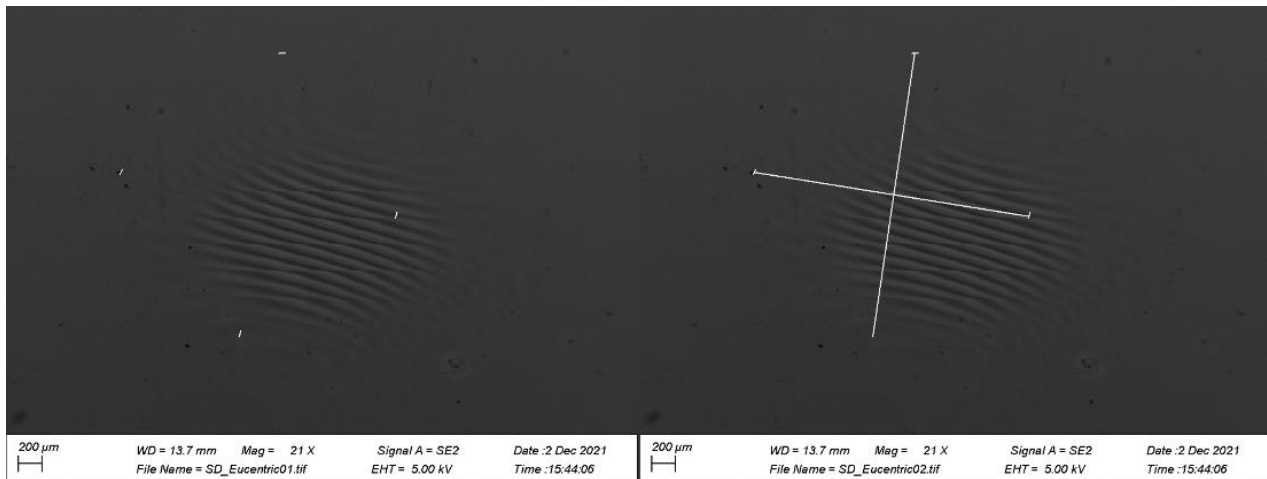


*Figure 19: Low magnification method of determining the EP of the sapphire dome sample. (Left image) a surface structure is identified and marked using the SEM software's marking tool. The sample is rotated 90 degrees and the structure is marked again. (right image) This is completed until a "crosshairs" can be drawn between the marks. The stage navigated to the middle of the crosshairs which is the EP of the stage. This is an image of the Sapphire dome sample at low magnification.*

In Figure 19, the method by which the EP is determined is outlined. Before this stage the approximate centre of the stage is chosen through clicking the centre of the carousel animation on the stage navigation pane (right). The scan time is reduced, to increase the speed of the raster scan, giving an almost live look at the sample, albeit with considerable noise detected. The stage is then rotated continuously while the stage is moved in the x and y direction towards the centre of the rotation. These translations are carried out until the centre

of the stage is found i.e. the continuous rotation doesn't move surface structures out of the field of view.

To find the exact EP of the stage, a surface blemish (piece of dust, dirt or damage) or other small distinguishing point is marked with the software line tool. The stage is rotated 90° and the point is marked again. This process is repeated 3 times until 4 marks remain on the screen. Points directly opposite each other are joined together with another line. The point marked by the intersection of these lines is the EP of the stage. The user can then "CTRL+click" on the EP to move the stage there. Finding the EP is fine if you have a random or a continuous surface structure all throughout the surface and therefore on the EP. However, for particular or desired points of interest on the surface it may be required to move away from imaging on the EP as it may be devoid of any interesting surface structures.
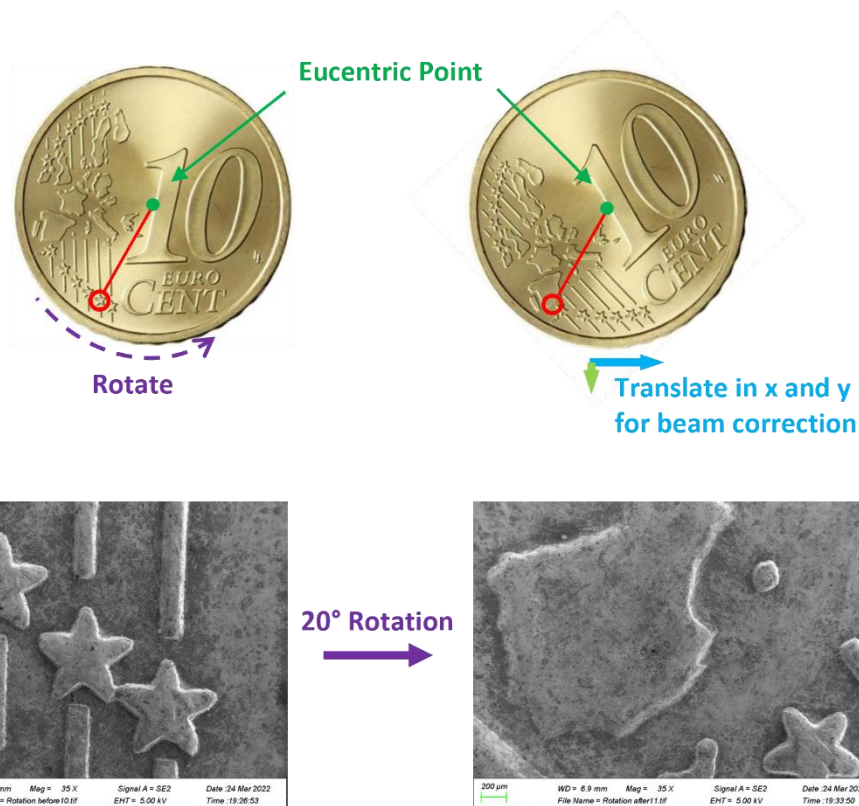


*Figure 20: Describes the movement of the field of view (red circle) of the electron beam on a sample when the FOV is a distance away from the EP on the sample. This is also demonstrated using electron micrographs by rotating a 10 cent coin 20° on the sample stage.*

Figure 20 shows the implications of sample rotation, when the beam is not imaging the sample at the EP of the stage. Sample rotation is carried out to obtain a different perspective of the

sample surface (star on 10 cent coin) for the photogrammetry software to create a 3D model. When the sample is rotated however, the beam moves off the subject of interest as the star is not on the EP of the stage, which would be the middle of the coin. The stage must therefore be translated in the x and y directions in order to recentre the subject of interest. During microscale photogrammetric capture, traversing the sample is the most substantial burden on the time to acquire a full dataset. This is especially the case when the subject of interest is far away from the EP (i.e. on one of the outer sample holders on the SEM carousel). To counter/help this drawback, stage automation was investigated.

### 6.3.2.    Stage Automation

In order to ease the time taken to traverse in the x and y direction after a rotation or tilt change a mathematic based predictive stage correcting program was written in the python programming language. Through understanding the movement of the stage in x, y, z, rotation and tilt, trigonometric translation calculations were written to predict where a point of interest would move when the stage was tilted or rotated. The calculations would then determine the x and y vectors needed to correct the stage position, so the electron beam was again falling on the point of interest. Because the electron beam is in a fixed position it is defined to be the z-axis of a 3D cartesian co-ordinate system. It is assumed that the electron beam is defined as being at x = y = 0. Then z = 0 is the height at which the electron beam is focused at, i.e. the focal point.
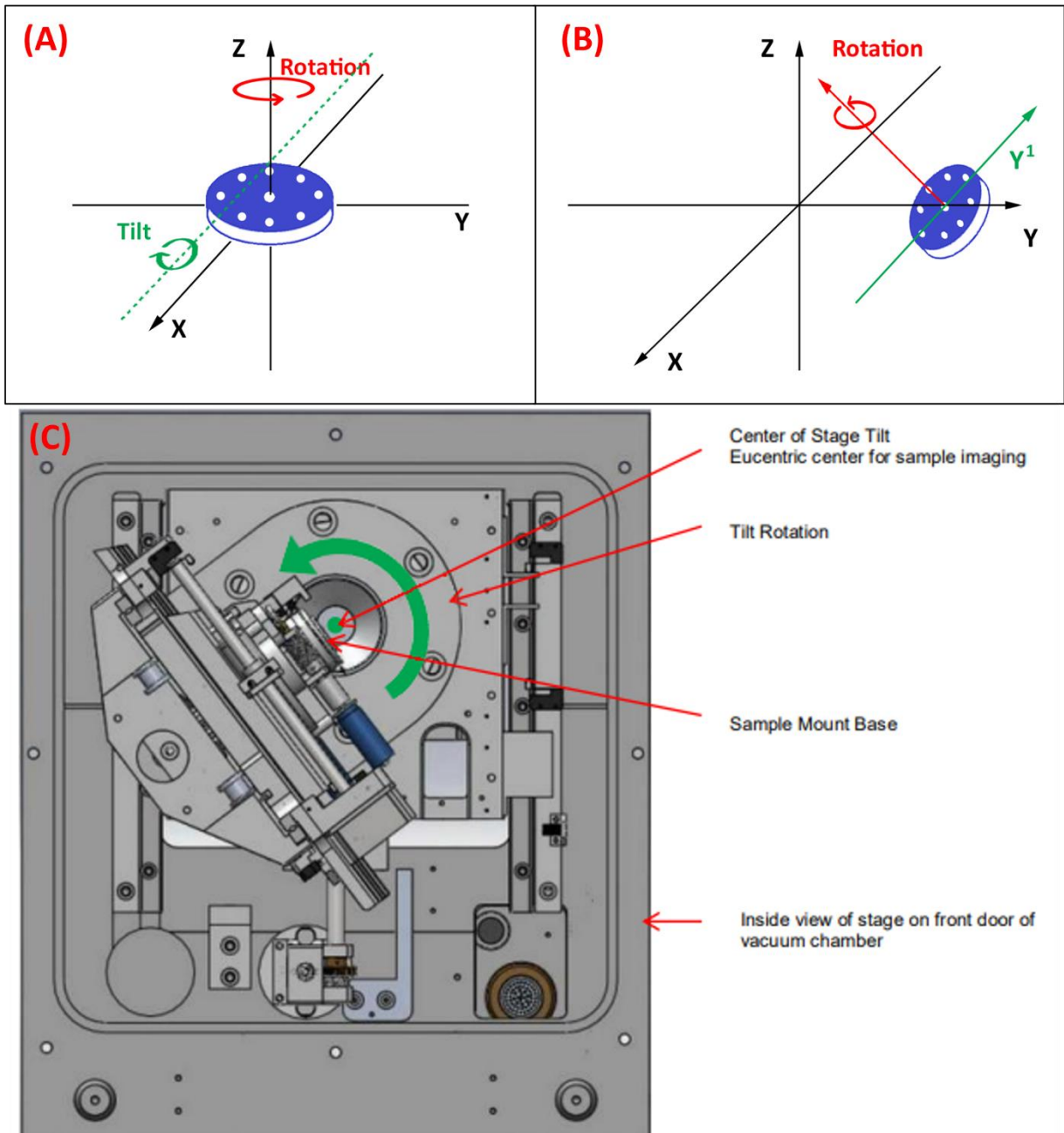
*Figure 21: A graphic showing: (A) The mechanisms by which the sample stage (blue circle) translates along the x, y and z axes and how it rotates and tilts, (B) How the methods of movement change their axes ($Y^1$ and Rotational axes) with a change of stage tilt. (C) A cross-section of the vacuum chamber door and how these axes correspond to it.*

As described in Figure 21, an SEM specimen stage can move in 5 ways. The stage can translate along the x, y and z axes. It can be tilted about an axis which is not fixed relative to the stage. The stage's tilt axis is shown in Figure 21 to be the midpoint of the stage part bolted to the specimen chamber door. Therefore, the axis of rotation is seen to run perpendicular over the

stage carousel in Figure 21 (A). The rotational axis is fixed relative to the stage's position and corresponds with the z-axis when the stage is at the origin and the tilt is zero but changes if the stage is tilted. When the stage tilts, the rotational axis tilts by the same angle, as shown in Figure 21 (B). The y'-axis, along which the stage translates, changes when the stage tilts. At zero tilt, the direction of translation is the y-axis. The x-axis along which the stage translates is unaffected by tilting. Therefore, because the movement of the stage is known, the movement of a point of interest away from the electron beam due to tilting or rotating can be mathematically predicted through the use of trigonometry.
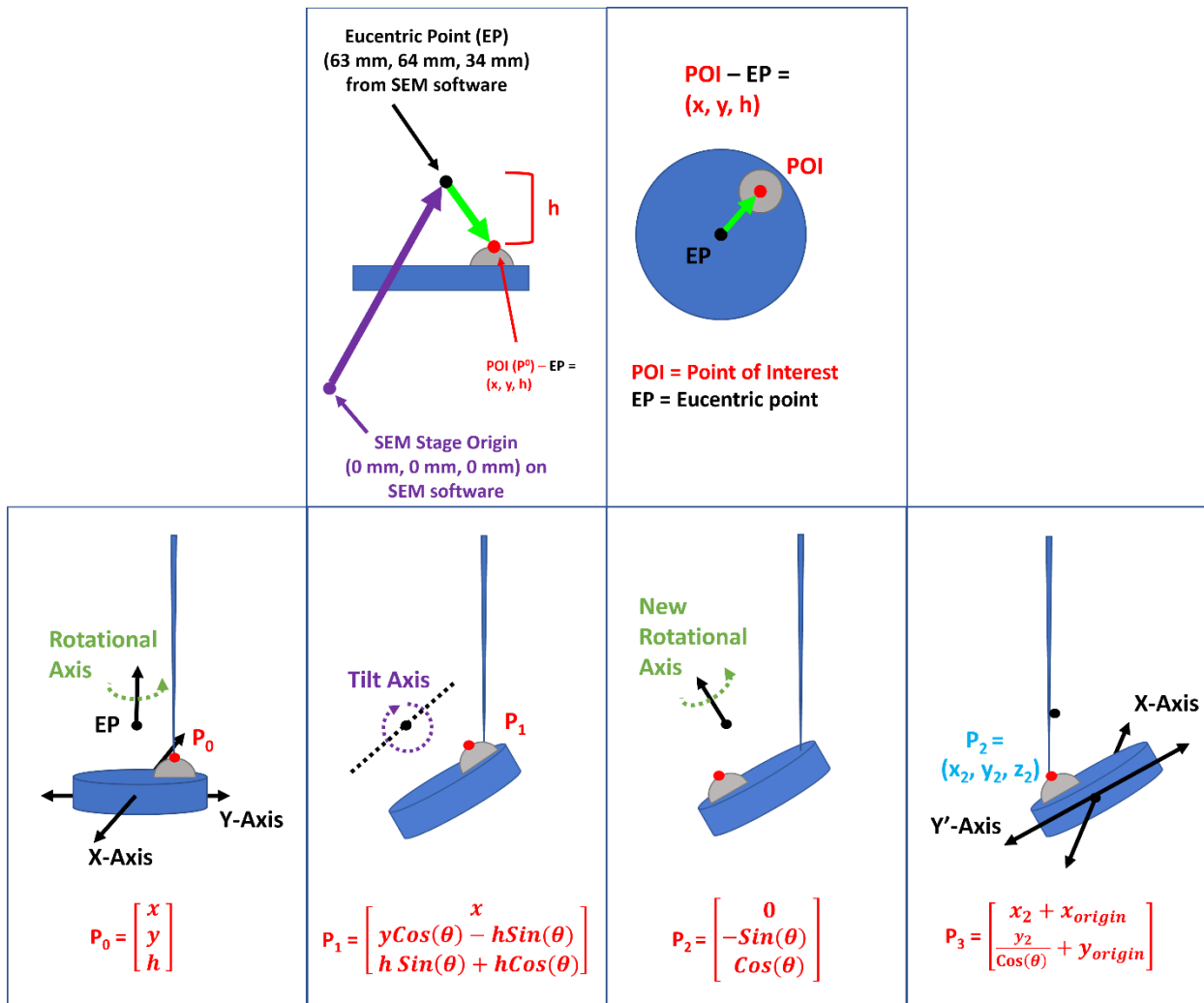


*Figure 22: The mathematical workflow of the stage co-ordinate prediction program produced.*

Figure 22 describes the mathematical workflow of predicting the movement of a point of interest with the movement of the sample stage. The SEM stage measures its movement in

millimetres and has a travel distance, in x, y, and z, of approximately 120 mm, 120mm and 70mm respectively, from the 0 mm values. The EP of the stage was used as a reference point for the mathematics and was defined as the origin of stage movement as this was the point through which the stage tilted and rotated. The EP, at an x and y value of 63 mm and 64mm, was made the origin in a new coordinate system to simplify calculations. The Point of Interest (POI) (or point $P_0$ at 0° tilt and 0° rotation) that we wish to image is at the point (x, y, h), demonstrated in Figure 22. It can be represented by the vector:

$$P_0 = \begin{bmatrix} x \\ y \\ h \end{bmatrix} \qquad (1.1)$$

The value of x and y in Eq (1.1) is the difference in distance (in mm) between the x and y value given by the SEM software for the EP, subtracted from the value of x and y when the electron beam intersects the POI at zero tilt and rotation, as described by Figure 22. The value of 'h' was the height difference between the EP and the POI on the sample surface. This was determined to be 16 mm through the use of a vernier callipers. As described in Figure 22, when the sample stage is tilted by the angle $\theta$, in order to obtain a new perspective of the point of interest, $P_0$ moves to $P_1$.

$$P_1 = \begin{bmatrix} x \\ yCos(\theta) - hSin(\theta) \\ ySin(\theta) + hCos(\theta) \end{bmatrix} \qquad (1.2)$$

The value of $\theta$ would be decided ahead of time and would depend on the photogrammetry software's requirements to produce a 3D model. When the POI is not on the EP, tilting the sample stage causes the POI to move away from the electron beam's illumination. The trigonometric transform, equation 1.2, shows the distance, in mm, needed to move the stage to once again illuminate the POI under the electron beam. As in Figure 22, when the sample stage is tilted, the rotational axis also tilts to the same degree, i.e. the sample stage's rotational axis is fixed relative to the stage.

$$P_2 = \begin{bmatrix} 0 \\ -Sin(\theta) \\ Cos(\theta) \end{bmatrix} \qquad (1.3)$$

When the stage is tilted by an angle $\theta$, the rotation axis is also tilted by an angle $\theta$ about the tilt axis. This change in rotational axis is accounted for with the equation 1.3. What is produced, is point $P_2$, the predicted position of the point of interest after the stage has been tilted and rotated. $P_2$ is defined as $(x_2, y_2, z_2)$. The x and y values of $P_2$ can be input into the stage navigation controls on the SEM software, in order for the electron beam to be illuminating the POI from a different perspective. However, the y-axis' movement is relative to the tilting axis, like the rotational axis, and thus must be accounted for when moving the stage. There are two possible ways to complete this.
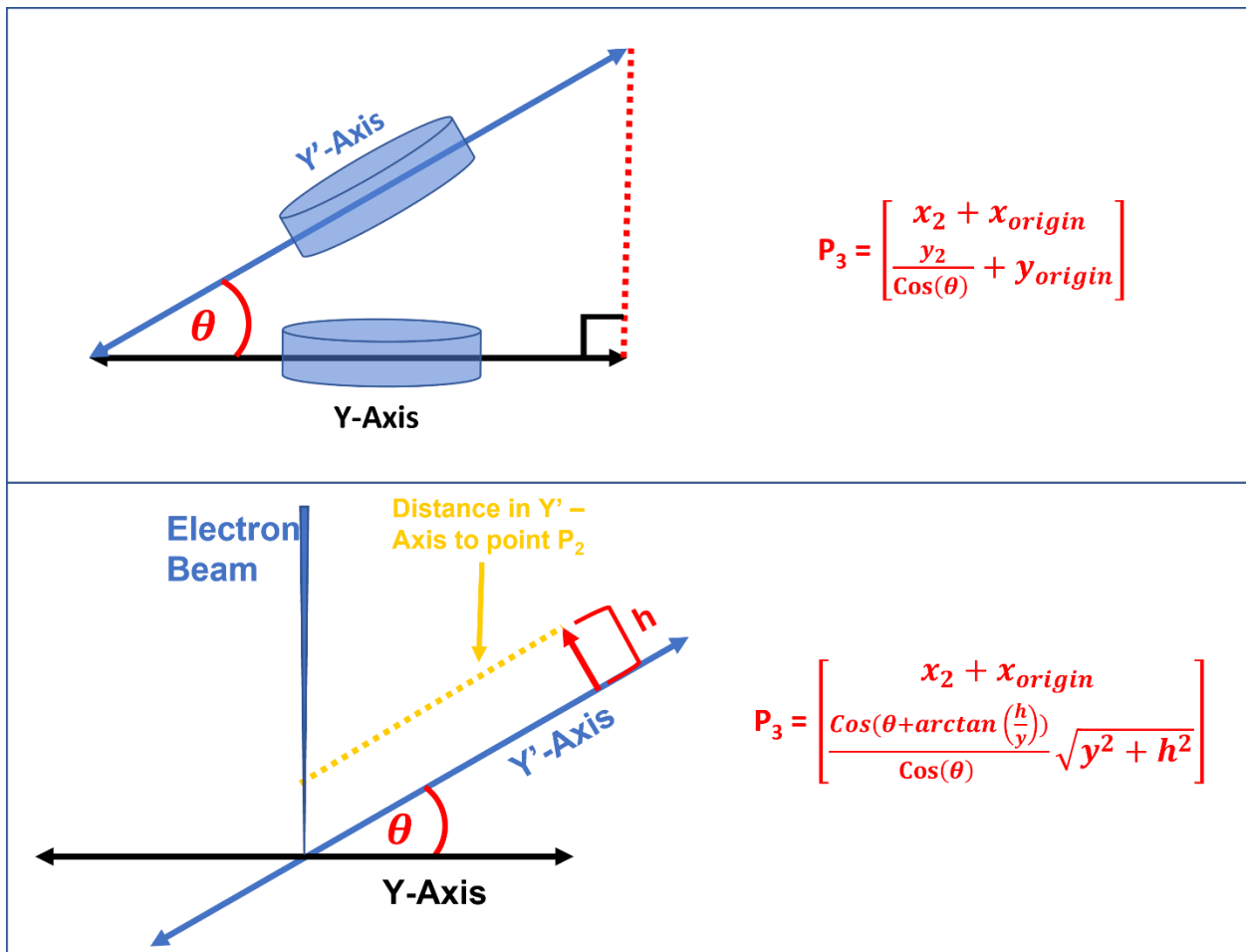


Figure 23: The two different trigonometric methods used to determine the distance along the y'-axis, the axis the sample stage moves along when the sample is tilted by an angle $\theta$.

Figure 23 above shows the two methods used to determine the distance needed to move the stage along the y'-axis, when the distance to be moved along the y-axis is given by Eq 1.1-1.3.

The first method is simple and describes the tangents involved as a right-angled triangle. The y'-axis is the hypotenuse, the y-axis is the adjacent with the angle between them being the tilting angle $\theta$. Therefore, we know the distance the stage needs to be translated along the y-axis (adjacent). The angle $(\theta)$ by which the stage was tilted is known, then the value of the hypothenuse/distance to be travelled in the y'-axis can be determined by simple trigonometry. The hypothenuse can be determined to be:

$$Cos(\theta) = \frac{y_2}{y'} \rightarrow y' = \frac{y_2}{Cos(\theta)} \tag{1.4}$$

Eq. 1.4 determines the distance that is to be travelled by the y'-axis given the distance to be travelled by the y-axis and the angle by which the stage has been tilted. The value determined (y') can be input straight into the SEM software, which will traverse the sample stage along the y'-axis and illuminate the POI with the electron beam once again from a different perspective. The equations 1.1 – 1.4 used in tandem with each other, have the ability to predict where the POI will move to when the sample stage has been tilted/rotated. Therefore, when they are programmed using Python programming language (as seen in the appendix), the output will be a list of x and y values of the POI when the sample stage has been tilted or rotated by different angles.

```
-----------------------------   -----------------------------   -----------------------------   -----------------------------
Tilt = 10                       Tilt = 20                       Tilt = 30                       Tilt = 40
-----------------------------   -----------------------------   -----------------------------   -----------------------------

Rotation = 0.0:                 Rotation = 0.0:                 Rotation = 0.0:                 Rotation = 0.0:
[ 47.62 , 51.334 ]              [ 47.62 , 51.146 ]              [ 47.62 , 50.933 ]              [ 47.62 , 50.671 ]
Rotation = 60.0:                Rotation = 60.0:                Rotation = 60.0:                Rotation = 60.0:
[ 43.802 , 71.397 ]             [ 43.802 , 71.209 ]             [ 43.802 , 70.996 ]             [ 43.802 , 70.734 ]
Rotation = 120.0:               Rotation = 120.0:               Rotation = 120.0:               Rotation = 120.0:
[ 59.268 , 84.735 ]             [ 59.268 , 84.547 ]             [ 59.268 , 84.334 ]             [ 59.268 , 84.072 ]
Rotation = 180.0:               Rotation = 180.0:               Rotation = 180.0:               Rotation = 180.0:
[ 78.552 , 78.01 ]              [ 78.552 , 77.822 ]             [ 78.552 , 77.609 ]             [ 78.552 , 77.347 ]
Rotation = 240.0:               Rotation = 240.0:               Rotation = 240.0:               Rotation = 240.0:
[ 82.37 , 57.947 ]              [ 82.37 , 57.759 ]              [ 82.37 , 57.546 ]              [ 82.37 , 57.284 ]
Rotation = 300.0:               Rotation = 300.0:               Rotation = 300.0:               Rotation = 300.0:
[ 66.904 , 44.609 ]             [ 66.904 , 44.421 ]             [ 66.904 , 44.208 ]             [ 66.904 , 43.946 ]
```

*Figure 24: A screenshot of the x and y value outputs when the predictive mathematics stage movement program is run.*

Figure 24 illustrates, the x and y co-ordinates predicted by the Python program. By entering the predicted co-ordinates into the SEM stage movement software, the POI will be aligned in the desired orientation on screen. This significantly improves the time to image and acquire photogrammetric datasets, particularly at low magnification. The accuracy of these values

55

diminished as the magnification of the electron beam was increased. This is thought to be for a number of reasons. Backlash of the stage gears, involved in stage movement, prevented the rotation value being exact every time. Backlash is caused by the clearance between two mating components. The clearance between two components leads to a loss in motion between the drive gear and the driven gear. This caused inaccurate positioning when rotating and traversing in x and y. This was not noticeable at low magnifications as they were relatively small differences. However, when the magnification increased, the small differences became relatively big differences and thus could no longer be ignored. The issue of backlash in the sample stage's gears could be avoided if they are turned in the same way every time. However, this may not always be possible when traversing in x and y when the sample is rotated through 360° and 40°.

The SmartSEM software did already contain a keystroke logger and macro production element to its software. This was developed for a small number of images in mind and would not have served our purposes efficiently. The **Zeiss© SmartSEM API** unlocks huge functionalities for the SEM in terms of developing programs. However, this is an expensive piece of software and does not align with the cost-effective, accessibility goals of this project.

The value of 'h' the height of the subject of interest from the tilt axis was difficult to determine. This was measured with a vernier callipers, but this brought about significant user error due to the lack of clear markings where the centre of stage rotation was. However, if there was an error in this value, the error was compounded as the image was magnified to smaller pixel numbers. This is because of the relative change in microscope inputs to a magnification change (i.e. the joystick doesn't move the image as far when you are at high magnification versus low magnification).

## 6.4.  Getting the photogrammetry dataset

The sapphire dome sample, synthesised by L. Keeney *et al.,* was chosen as the sample of choice due to its high degree of surface roughness as well as the domes' unique surface shape. This would help the photogrammetry software's photo matching algorithm to find matching points on multiple photos. For ease of imaging, after the sample was mounted on an aluminium

sample stub, it was fixed to the centre position of the sample carousel in order to view the sample at the EP of the stage. The sample consists of repeating, uniquely dome shaped crystalline structures, and have approximately 125,000 domes per mm$^2$. Therefore, identifying one particular dome, over multiple tilts and rotations or perspective changes, can be challenging.



**"Mohawk" Dome for Focusing**          **Dome for Imaging**
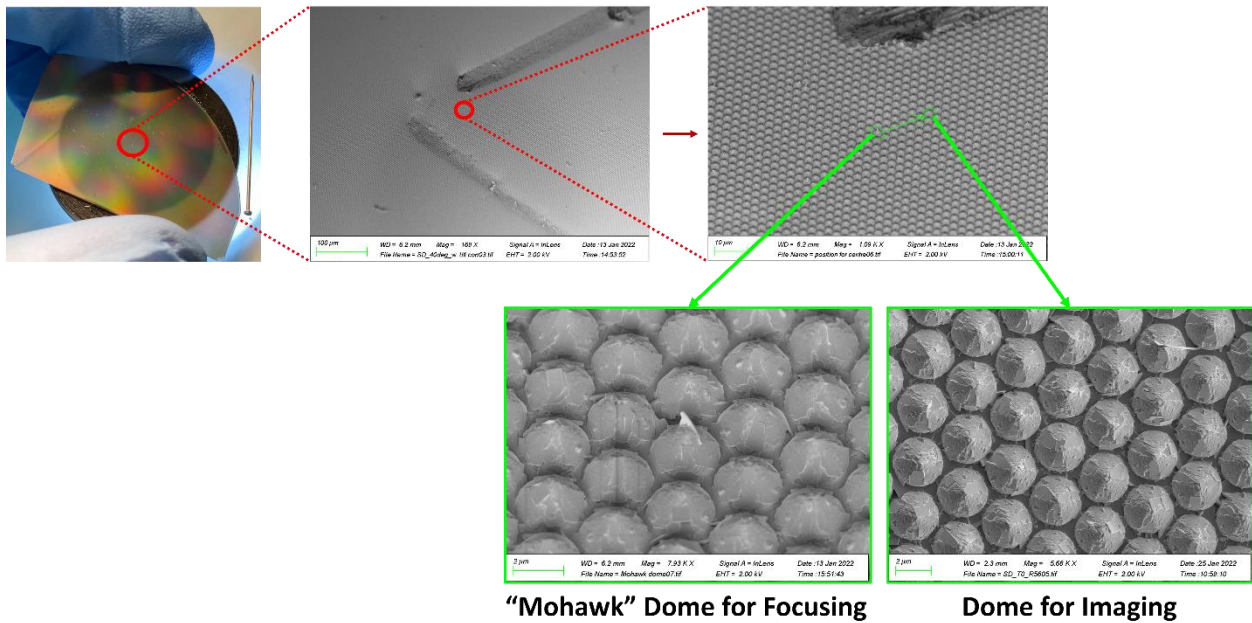
*Figure 25: The method of choosing a particular dome, which stands out at low magnification, to image multiple times.*

Figure 25, shows how the sample surface was marked in order to flag the approximate centre of the sample. The marking, an L-shape, was carried out using a sewing pin under an optical microscope. The sewing pin was scraped along the surface of the sample twice to form an L-shaped scratch. This scratch allowed for ease of identification of the point of interest, even from low magnification. Marking the sample surface in this way also prevents the SEM user from losing the point of interest when rotating or tilting or becoming lost on the sample surface, which could easily happen without this marking. After this, the dome which was to be photogrammetrically reconstructed was chosen. This was chosen, far enough away from the marking so it would not show up in the final model, but also close enough so it could be easily identified. Therefore, 13 domes in the down direction from the long scratch of the L-shape was a slightly disfigured dome. This was identified as a focusing point. 6 domes to the right of

this dome was identified as the dome to be imaged. The two points of interest are highlighted in green in Figure 25: the dome designated for focusing and the dome designated for imaging.

In order for the beam to be focused more accurately, the magnification was increased. As mentioned above, deposition occurs more readily at higher magnifications, due to focusing the electron dose over a smaller area. As seen in Figure 25, a focus point was therefore established, to avoid excess deposition/raster burn on the subject of interest. In the sapphire dome sample, this was the "mohawk" dome. This particular dome has a growth on its crown, which is triangular in shape and looks like the mohawk hairstyle. This dome was chosen as the point where the beam would be focused on, and the astigmatism corrected as it was easily recognisable from every viewpoint and from lower magnification. At 0° tilt, if the sample is rotated on the sample stage, the subject of interest will not change its height relative to the pole piece and thus there will be no need to refocus/correct astigmatism.
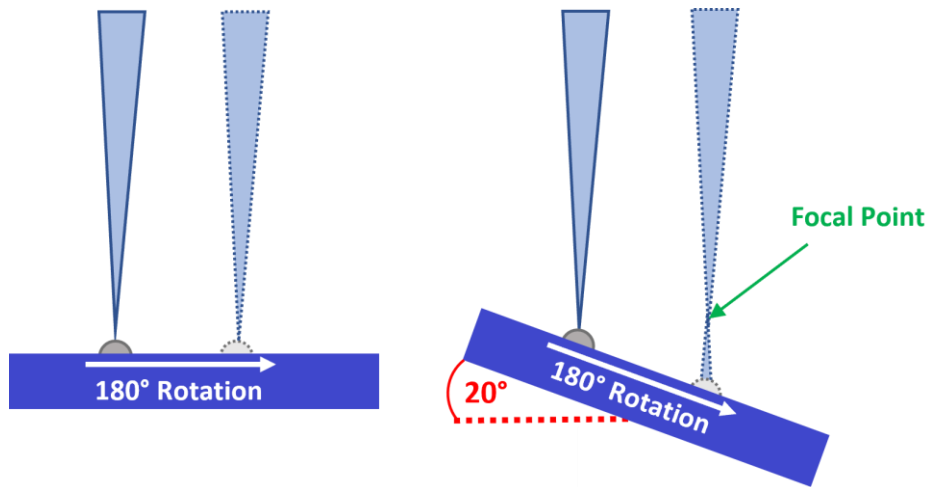


*Figure 26: Describes the differences in focus caused by changes in tilting and rotating.*

However, as seen in Figure 26, when the sample is tilted and then rotated the relative height between the subject and the pole piece will change and thus focus and astigmatism must be corrected. The defocus because of tilting/rotating becomes more severe when the angle of tilt is larger. The defocus is alleviated somewhat, due to the fact that the stage moves in the y-axis relative to the tilt. The sample therefore can be corrected back to the original position by correcting the y-axis element. This however is imperfect, due to imperfections in stage movement and thus focus and astigmatism must be corrected.

Magnification was kept constant throughout each image capture to ensure the same points were being counted for the image matching algorithm.

### 6.4.1. Dynamic Focus

As mentioned above, in section 5.4, in order to obtain different perspectives of the sample surface, the sample stage must be tilted to a significant degree. This can cause problems for the image matching algorithms in photogrammetry software as parts of a sample that were in focus at low/zero tilt would be defocused at high tilt. The image matching algorithm would therefore fail to recognise an image at high tilt is viewing the same surface structure as the surface structure at low/zero tilt. This phenomenon can be corrected using the dynamic focus function on the **Zeiss© ULTRA** SEM.
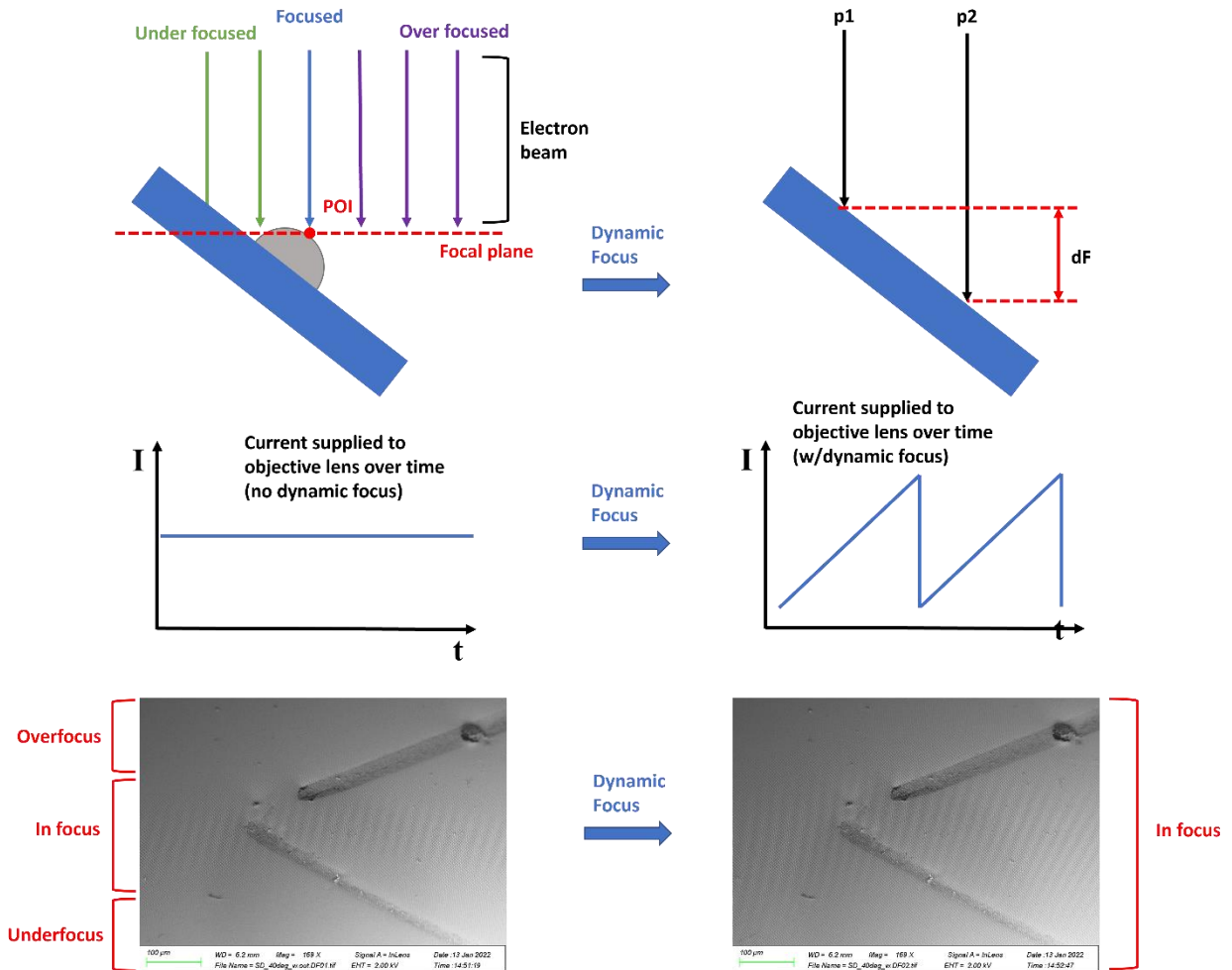


*Figure 27: The mechanism of action and demonstration of dynamic focus and its use for photogrammetric dataset capture*

The operation of the dynamic focus correction is illustrated in Figure 27. Highly tilted samples induce underfocus and overfocus of the electron beam, resulting in defocusing at the edges of the micrographs. This is demonstrated in the electron micrograph of the sapphire dome sample in Figure 27, where the top and bottom of the specimen is out of focus, demonstrated by the surface structures on the top left and right and the surface structures on the bottom right. The middle of this micrograph is in focus with surface structures being observed with high fidelity. This is contrasted with the electron micrograph to its right where all of the image is in focus. This is achieved by using the dynamic focus correction setting/parameter on the SEM control panel. Dynamic focus achieves this through the focal plane of the sample surface following the scanning beam and thus the defocus at the edge of the micrographs are eliminated. As mentioned in section 3.3, the position of the electron beam focal plane is determined by the current which flows through the objective lens in the electron column. For dynamic focus, the power amplifier supplies the objective lens with a "saw-tooth" current in order to adjust the focal length (dF in Figure 27) along the tilted sample surface. Thus, if the objective lens coil is supplied with the saw tooth current, it is reduced at the top of the image, allowing for a longer WD (p1 in Figure 27). The current in the middle of the image should correspond to the total current input to the objective lens when there is no dynamic focus selected. At the bottom of the image, more current is supplied, in order to reduce the WD (p2 in Figure 27). What results is an image with all of its area in focus, which prevent matching images from failing to be processed together by the imaging matching program. This parameter is generally reserved for lower magnification work, but becomes crucial for higher magnifications when high detail is needed, like in the case of producing 3D models using photogrammetry software.

### 6.4.2. High current mode

High current mode increases the current in the electron beam, through an activation of the condenser lens, to increase the amount of signal that reaches the detectors as well as improving the signal to noise ratio. However, increasing the current also has the (sometimes unwanted) side effects of increasing the spot size (probe diameter); from the electron brightness equation increasing the electron beam damage done to the sample surface.[77]

- Higher resolution
- Grainy Image
- Less damage
- Lower Depth of Field

Low ⟵ **Probe Current** ⟶ High

- Lower resolution
- Smooth Image
- More damage
- Higher Depth of Field
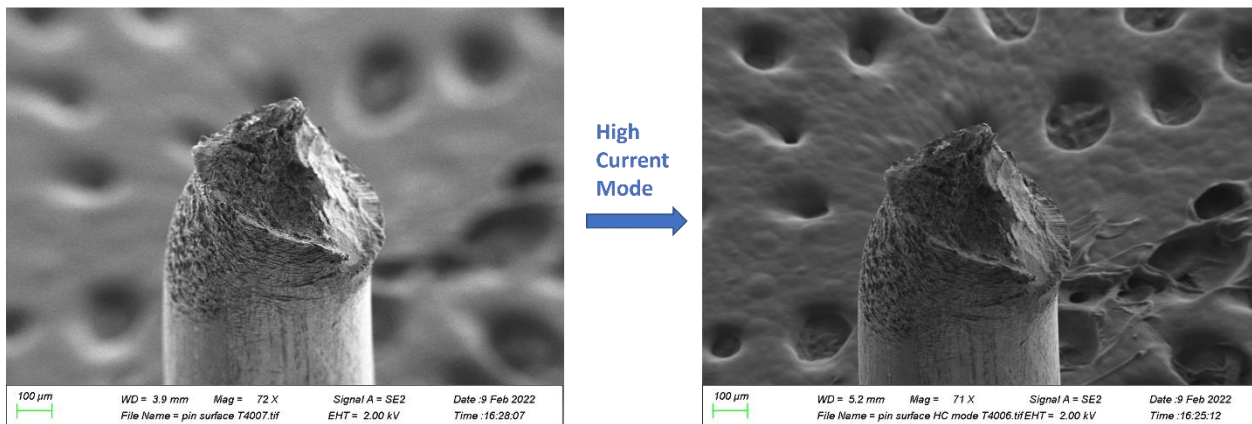
High Current Mode →

*Figure 28: Demonstration of high current mode (turned on in the image on the right), by imaging the fracture surface of a safety pin with the same aperture size, how it affects imaging and how it affects the depth of field of the image.*

As can be seen in Figure 28, increasing the probe diameter has the knock-on effect of increasing the depth of field of the electron beam, allowing for more of the sample's structures at different heights to be in focus, rather than just a very small area. This is demonstrated by the steel safety pin which has been bent multiple times and broken, in order to simulate a ductile metal fracture surface. The final position of the pin is in an L-shape, with the fractured surface pointing in the direction of the electron beam axis/z-axis. In the image on the left-hand side, conventional current is being used to image the surface. A lot of surface fracture structures can be seen with good resolution on the part of the sample which is in focus. The parameters chosen for this sample was a surface sensitive regime (low kV and small aperture) under the SE2 detector. Therefore, the sample has a small spot size/ good resolution at the plane of focus on the sample. This highlights the lack of focus of the parts of sample which have a different height value to that of the plane of focus. This is most evidently displayed by the carbon tab in the background of the image, which has a substantial overfocus. This is recognisable as a shallow depth of field. This depth of field is contrasted to that of the image, in Figure 28, on the right-hand side. In this image the high current mode has been turned on. This causes the beam current to increase and therefore increases the spot size, which in turn

increases the depth of field. This can be easily identified by the much clearer surface resolution of the carbon tab in the background of the image.

## 6.5. Parameter choice

Therefore, in order to obtain a large number of electron micrographs with a high degree of detail over the entire height range of the sample, we need a balance of operating parameters. High surface sensitivity parameters (In-Lens, small aperture, small WD, small accelerating voltage) are needed while also having a suitable depth of field (the opposite of these things) to ensure that both the top-most and bottom-most of the surface structure is in focus. Therefore, the following parameters were used to obtain the 3D model's dataset:

| Detector Choice | Accelerating Voltage | Aperture size | Working distance | Dynamic Focus | High Current mode |
|---|---|---|---|---|---|
| In-Lens | 2 kV | 20 µm | 5 mm | ☑ | ☑ |

*Table 1: Showing the key parameter choices for SEM 3D model reconstruction.*

Table 1 shows the features which were found to be optimal for the samples that were imaged. The In-Lens detector was used to ensure good topographic contrast, high surface sensitivity and avoid asymmetric electron collection as described in section 6.2.3. The accelerating voltage was kept relatively low (2 kV) to ensure the surface sensitivity of the electrons as a low accelerating voltage has an interaction volume much closer to the surface of the sample. Aperture size was kept at 20 µm, slightly smaller than the standard 30 µm to boost the sample's depth of field without deteriorating beam current too much. The WD was kept at 5 mm. The WD should be kept short to ensure good resolution but also kept larger when aiming for a longer depth of field. This WD was also chosen for practical reasons, to give adequate space for the pole piece during large sample tilting. As mentioned in section 6.4.1 and 6.4.2 dynamic focus and high current mode are turned on for the reasons stated in those sections. These parameters working together will increase the probability that images are matched between one another, allowing for the most matching points to be obtained for the image matching algorithm (SIFT) in the photogrammetry software.

## 6.6. Sample choice

Three samples were investigated as possible candidates for the 3D SEM photogrammetry regime. These were GaSe Nanoribbons, produced by the LTM lab in Grenoble by Pauline Hauchecorne, PEG nanopillars produced by Niamh Geoghegan for application in tissue engineering, a ten cent coin produced by the European central bank and B6TFMO, also called Sapphire domes, produced by Louise Colfer of the Tyndall Institute. These samples were chosen on their basis that they have interesting, rough, high aspect ratio or delicate surface features which AFM would find difficult to image, with the exception of the 10 cent coin, which was chosen as an easily imaged test sample.
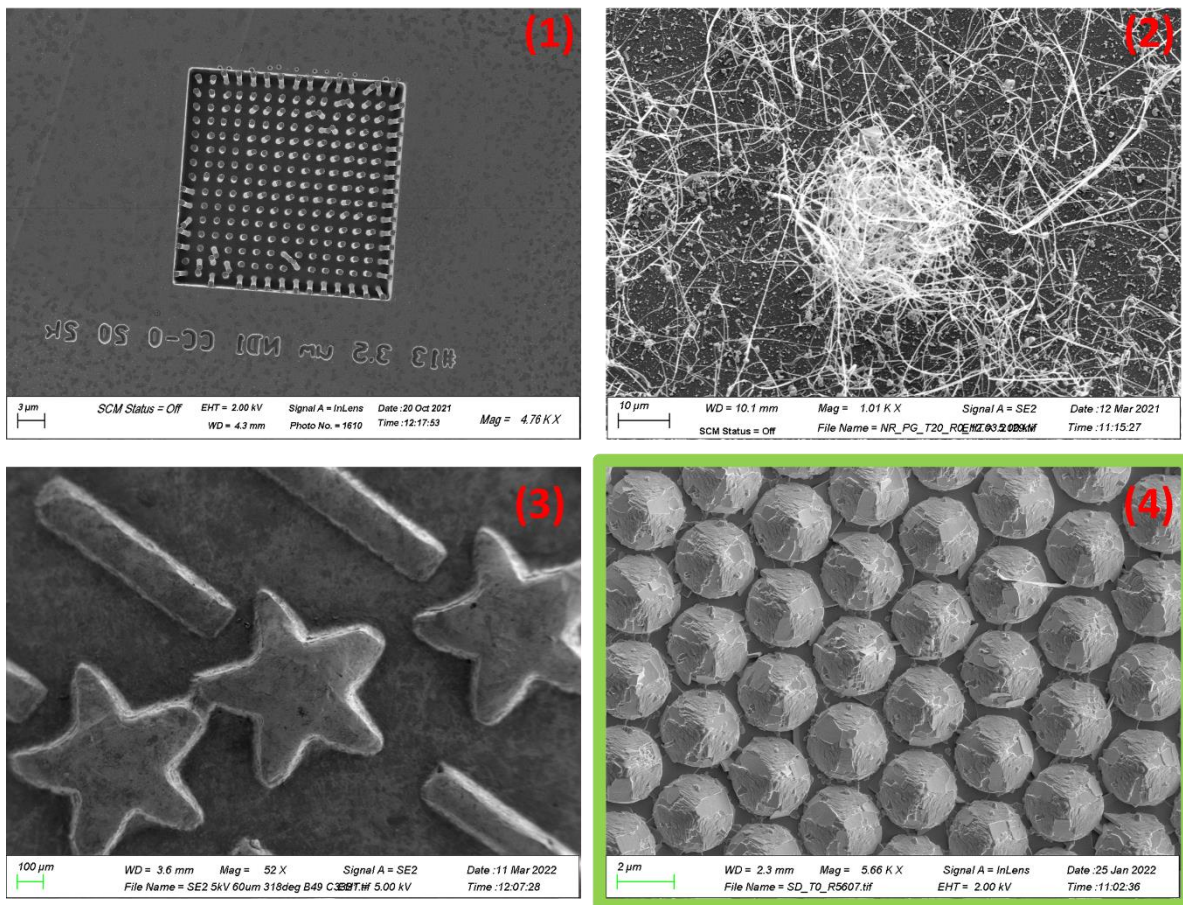


*Figure 29: Scanning electron micrographs of (1) the PEG nanoribbons sample, (2) the GaSe Nanoribbons sample, (3) the 10 cent coin sample (4) and the sapphire dome sample.*

Displayed in Figure 29 are SEM images taken of each of the samples which were considered for the 3D photogrammetry regime.

The PEG Nanopillars is a polyethylene glycol sample, displayed in Figure 29 (1) which finds application in tissue engineering as possible cellular supports. The sample, produced by a replica molding of 2-photon polymerization is predictable and easy to navigate due to the structure identification code imprinted in the synthesis stage. Additionally, the sample has regular lines of pillars, with some falling over, giving the sample extra recognizability. Due to Dr. Geoghegan researching the effect of different length scale and aspect ratio of the pillars on the efficacy of cellular growth, multiple length and diameter pillars were produced. To investigate their length scales the pillars were imaged by AFM, which worked well for shorter pillars. Some loss of data was noted on higher pillars, due to the shape of the pillars and the pit they sit in and the shape of the AFM's cantilever. The sample was therefore chosen as a sample for 3D SEM photogrammetry reconstruction. The nanopillars, made from an insulating material, are a very insulating sample. As a result, they are very reactive to the electron beam, even when the sample has undergone rigorous hygiene (plasma cleaning) and conduction regimes (Au/Pd sputtering, silver colloid paint and copper tape conduction). The pillars were observed to bend and move under high magnification and under lower magnification over a long period of time. If the point of interest's shape is changing over time, the point matching algorithm in the photogrammetry software would have difficulty choosing similar points between images, resulting in a failed or incorrect reconstruction. A preliminary dataset was obtained which failed under all attempted software settings and therefore the sample was discarded as a candidate for this project.

Nanoribbons Very interesting sample with an optoelectronics application. The extremely thin nanoribbons are grown from indium seed droplets on a silicon surface with subsequent GaSe chemical vapor deposition. The ribbons grow in free space above the silicon substrate in random directions and can tangle themselves into knots as seen in Figure 29 (2). The ribbons can grow significantly high in the z direction. This makes obtaining a height image via. AFM extremely challenging. The cantilever could potentially get tangled in the ribbons which could break it. Alternatively, the cantilever could break the delicate nanoribbon structures. Either of these issues would lead to significant errors in the resulting data. It was thought that the SEM photogrammetry regime could solve these issues and a preliminary data set for the

nanoribbons was imaged. The sample was difficult to image due to the fact that the sample was difficult to navigate (in contrast to the nanopillar sample), due absence of structures which were easily recognizable from low magnification or different tilt perspectives. Additionally, the nanoribbons were very sensitive to the electron beam. Under high magnification, or lower magnification for a prolonged time, the ribbons were observed to move. This would have major implications for the point matching algorithm, discussed in section 3.2.2.3, which requires strictly stationary subjects. If the ribbons were to move under the beam, this would put them out of place for subsequent images in order for them to be matched together and thus reconstructed into a 3D model. A 3D model was reconstructed, but the model had significant exclusions in data with nanoribbons seemingly floating in free space and was therefore not chosen as a candidate for this project.

A 10-cent euro coin was also imaged using the SEM, which is reported by Figure 29 (3). The coin had a very easily navigable surface, was conductive without any additional techniques and had large surface features (stars) which were the ideal test subjects for using photogrammetry within the SEM. This sample, however, would not make a good argument for this project as its surface would very easily be imaged by an AFM and reconstructed into a 3D model.

The sample that was chosen was therefore the Sapphire dome sample, synthesized by L. Colfer. This sample, with application in optoelectronics, is produced by chemical vapour of B6TFMO being deposited onto a sapphire substrate. What results is shown in the scanning electron micrograph on Figure 29 (4). The B6TFMO crystallizes on the sapphire substrate and forms a regular dome shape with a microscale size (approximately 2.7 µm in diameter). The texture of the domes, however, are anything but regular. Irregular crystal facets, nanoscale in size, grow in all different shapes and sizes and all different directions. This surface is ideal for 3D model reconstruction, due to its large overall size with small detail on its surface. AFM would struggle to image the overall structure and the surface roughness of the sample, without some loss of data. The fact that the sample is conductive allows for extended imaging periods without significant challenges.

## 6.7. 3D Model Reconstruction

There are a number of photogrammetry software packages available on the market, produced by several different software companies, some of which can be used specifically with a micrograph dataset,[139] however, the motivation of this project is to use open source software for these reconstructions to make this form of 3D characterisation accessible to anyone with access to an SEM. For the most part, every photogrammetry software uses the same mathematical algorithms when producing a 3D model (i.e. Bundle adjustment, SIFT, SfM, MVS etc.). Photogrammetry software companies differentiate themselves from their competitors by supplying extra proprietary reconstruction algorithms, pre-determined settings/parameters for specific 3D model types (i.e. aerial drone capture), editing tools/utilities and/or on-demand customer support. Therefore, when determining the number of 3D models required and the desired level of reconstruction quality, it is crucial to consider all available options and factors.

| Software name | Price | Photo Limit | Needs a GPU |
|---|---|---|---|
| Meshroom | Free | No | Y |
| 3DF Zephyr | Free-$3500 | Yes | N |
| Mic Mac | Free | No | N |
| Agisoft Metashape | $180-3500 | Yes | Y |
| Reality Capture | Pay-as-you-go - $3750 | Yes | Y |

Table 2: A comparison of a selection of photogrammetry software, based on their price and their support of acceleration using a Graphics Processing Unit (GPU). Meshroom was the software of choice due to its accessibility.

Table 2 compares a number of photogrammetry software packages on the basis of their cost, if they have a limit on the number of photos that can be used and if the software has the ability to produce a model on CPU power alone. The photogrammetry software used to carry out the 3D reconstruction was called **Meshroom©**, produced by **AliceVision©** software. **AliceVision©**'s mission statement is to "democratize the technologies of 3D digitization from

photographs", which aligns with this project's aims to determine most efficient and accessible method to produce 3D models from a number of SEM micrographs taken from a sample at different perspectives.

**Meshroom©** uses the different 3D model reconstruction algorithms mentioned in the introduction and illustrated by Figure 3. Once the dataset of the sapphire domes, made up of the 96 images obtained using the SEM, has been input into the software and the reconstruction can be started. In general, for this technique, the more images input into the software, the better quality the resulting 3D model will be. However, there has to be a balance with finite operator time and instrument time cost. This number arises from obtaining 18 images at 20 degree rotation increments at 5 different tilt values as well as 6 images from 0 degrees tilt, top-down mapping the point of interest. As mentioned in section 3.2.1, the software can determine the 3D position and orientation of the camera and subject through its algorithms. Therefore, the technique did not require any prior positional information of the images. Thus, the images were input and the algorithm was started. The software includes a number of "nodes" which contain these algorithms. The first step is the Structure-from-Motion node, which contains both the SIFT, keypoint matching algorithm and bundle adjustment algorithm in a single step.
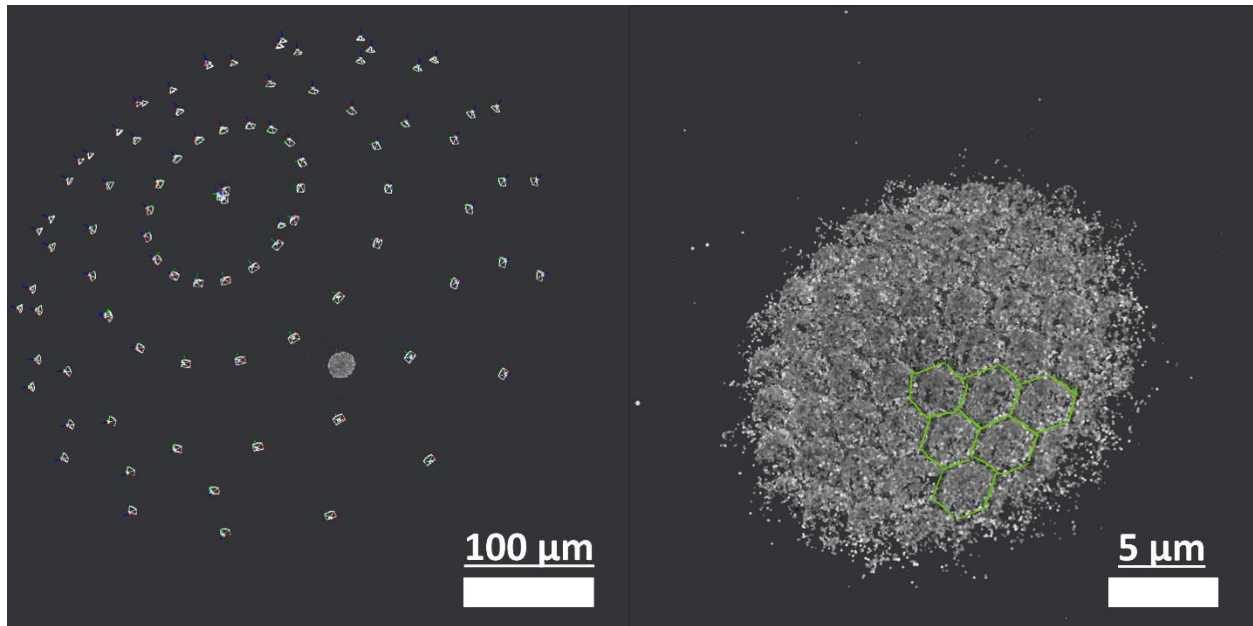
*Figure 30: The results of the "structure-from-motion" node from the Meshroom software of the sapphire dome dataset. (Left) The image shows the SfM algorithm, which estimates the positions of the keypoints (computed by SIFT) and the positions and orientations of the "cameras". (Right) A zoomed in 3D image of the dense point cloud of the dataset with the domes outlined by green lines.*

Illustrated in Figure 30, is the first step in reconstructing the 3D structure of the microstructure of the sapphire dome sample. Here **Meshroom©** applies the SfM algorithm, containing the SIFT and bundle adjustment. As mentioned in the introduction, this algorithm estimates the positions of common 2D keypoints over 96 images. After this, the bundle adjustment algorithm estimates the positions of the keypoints in 3D space as well as the positions of the "cameras". The "cameras" in this sense, means the position and orientation that the image was taken from. This is presented in Figure 30 (left), with a hemisphere of cameras surrounding the sample's dense point cloud. This results in the dense point cloud which has been made up of matching keypoints within 3D space. The basic shape of the sapphire domes can be made out from this image, which is outlined by the green lines showing the sapphire substrate in between domes. Some keypoints have been mismatched, as illustrated by outlier points to the left and above the 3D dense point cloud, in Figure 30. The dense point cloud contains 106,895 keypoints which have been identified by the SIFT algorithm and coordinated in 3D space by bundle adjustment. The software can be made to increase or decrease the sensitivity by which keypoints are found. The former of which could increase the quality of the dense point cloud

and therefore the quality of the resulting 3D model. However, increasing the sensitivity for keypoint matching across images can also lead to more errors in the form of outliers. Outliers, like in any quantitative analysis, can skew data in a negative way. Furthermore, the increased sensitivity for matching keypoints can greatly increase the time for computation. Thus, outliers are minimised as much as possible by choosing the best parameters on the photogrammetry software as possible, by playing to the strengths of the algorithms as mentioned in section 3.2.2 and by using parameters to mimic how photographers would take photos for macroscale photogrammetry. The next step in the process is the meshing step.
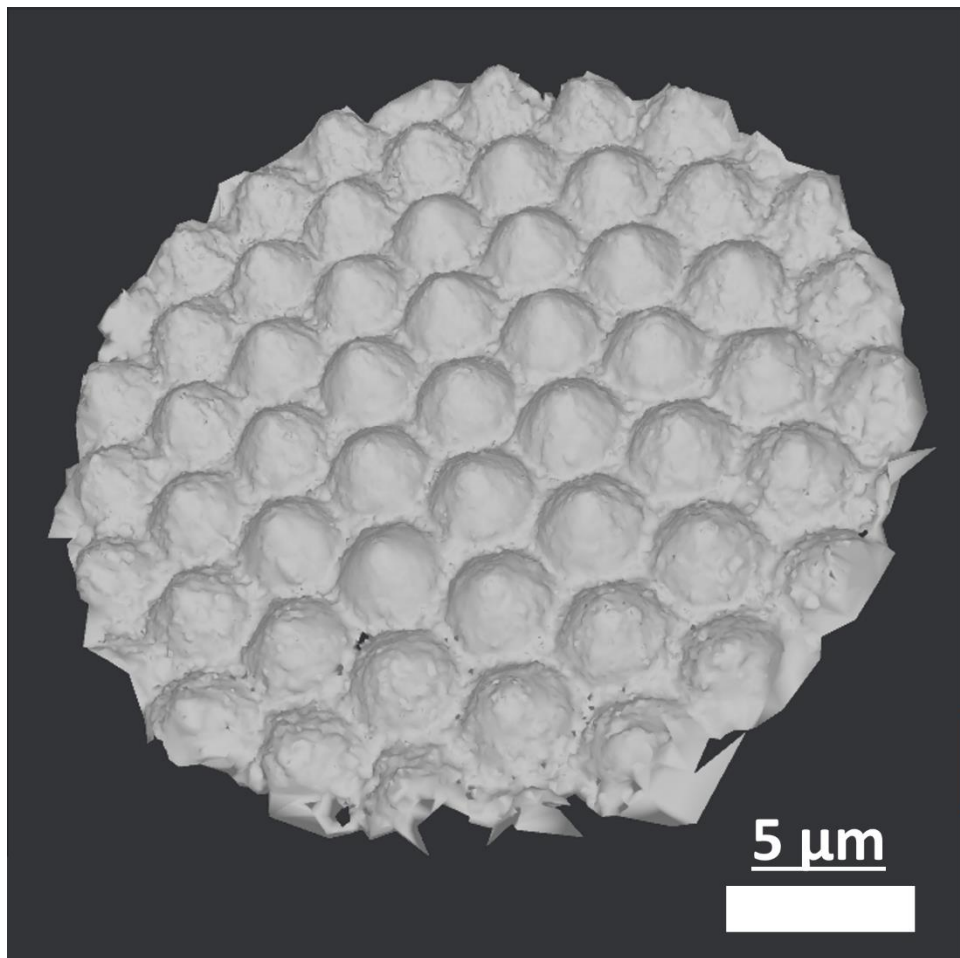


*Figure 31: The computed result of the meshing algorithm of the sapphire dome dataset.*

The objective of this step is to take the results from the SfM algorithm and generate a dense geometric surface depiction of the sample's surface. Illustrated in Figure 31is the mesh which has been generated. The meshing algorithm used by **Meshroom©** is a 3D Delaunay

tetrahedralization which calculates the shape of the sample's surface through polygonal meshing i.e. through linking the 3D keypoints matched by the previous algorithms. It does this by filling the spaces between keypoints with 2D shapes, in this case tetrahedrons. What results is a 3D mesh of the sapphire dome sample outlining the general shape of the subject, which is much more connected as shown in Figure 31. This step is much more complex than the general shape presented by the point cloud in Figure 30. The denser the point cloud, the smaller the tetrahedrons between points, allowing for a more refined structure. Once the mesh has been completed, then the next step is texturing it.
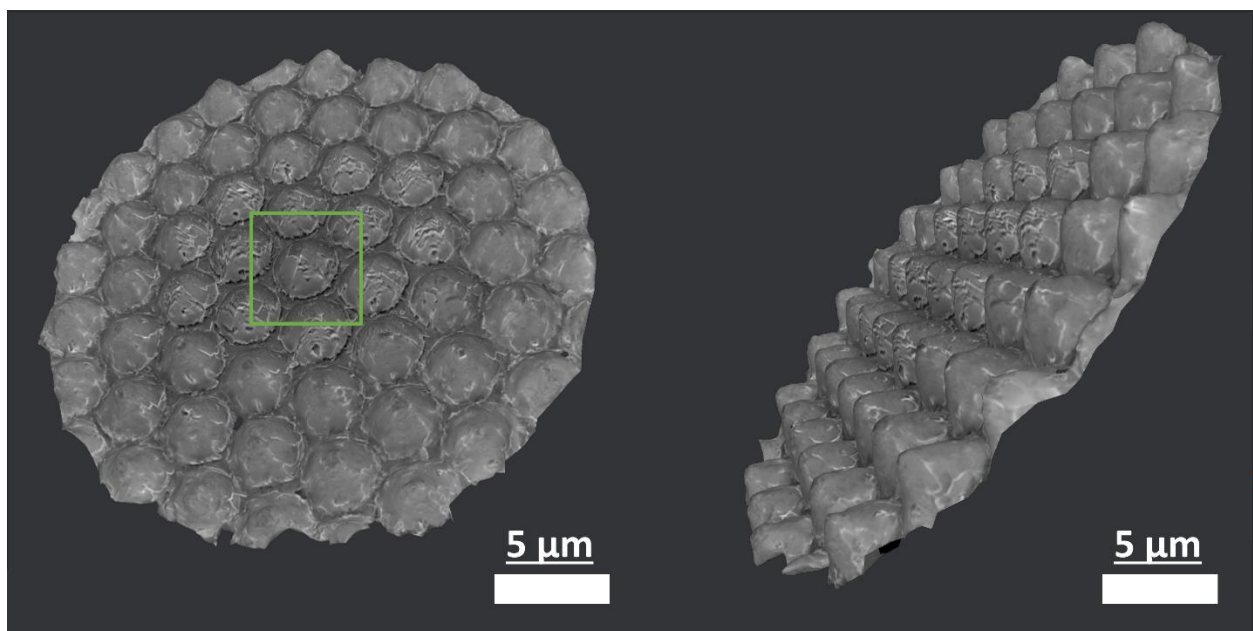


*Figure 32: Side by side images showing the textured 3D model of the Sapphire dome sample. (Left) the image shows the textured version of the mesh, with a green box indicating the dome that was chosen to be imaged and (right) the 3D dome shape of the sapphire dome.*

Demonstrated in Figure 32 (left) is the textured mesh of the sapphire dome sample. The dome that was chosen as the dome to be imaged is clearly the middle dome, indicated with a green box. It can be clearly seen that the pattern on the dome is the same as the image in Figure 25(green box), indicating that the reconstruction process of a microscale structure was a success. A brightness gradient can be seen from the outside of the 3D model's circular shape, where it is a lighter grey, to the middle, where it is a darker grey. This highlights the effect that

the dwell time can have on the sample's contamination level. Reconstructing the 3D model was the shortest, from a time standpoint, only taking 15-20 minutes.

However, the smoothness of the 3D model's surface can also be noted in Figure 31 and in Figure 32 and contrasted to the surface's very crystalline, jagged microsurface as seen in Figure 29. Therefore, during the reconstruction this information was lost. This could be due to a lack of key point matches, but when the minimum number of keypoint matches setting was increased, an insignificant number of extra keypoints were obtained. The time taken to produce a 3D model, with these insignificant increases in quality, was increased by approximately 4 times (1.5 hours), adding to an already time-consuming process, making the new process not worth the time it took.

**3DF Zephyr©**, the algorithm used in Figure 3, uses different 3D model reconstruction algorithms. As mentioned in Table 1, 3DF Zephyr comes in a number of different versions, including proprietary algorithms (Samantha®, Stasia®, Sasha®) didn't work as well with the SEM micrographs in comparison to that of the tree stump. This was quoted as being because the software's algorithms heavily depend on colour scales for small datasets. Therefore, the overly greyscale datasets, like an SEM micrograph dataset, would not be suitable.

A 3D model of a 10-cent coin was also obtained using the same method. This was used as a test subject for photogrammetry in the SEM as its surface was very easily navigable and because of its large surface structures. Images of the 3D model for this sample can be found in Figure 34 in the appendix.

## 6.8. Comparison of Sapphire Dome 3D model with AFM data

The sapphire dome sample was also imaged, by L. Colfer, using an AFM. As mentioned in section 3.5, the AFM is a versatile technique used to image the 3D structure of a nanoscale sample's surface. However, the resolution of this 3D characterisation technique can be affected by a wide range of surface roughness.
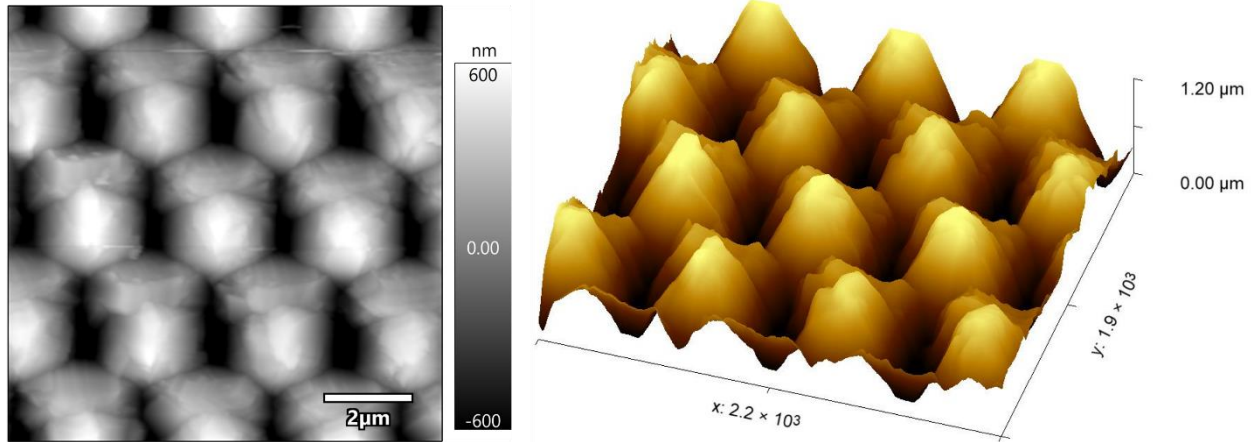
*Figure 33: (Left) Atomic Force Microscope (AFM) AC tapping mode image of the Sapphire Dome sample using a tip with a 7 nm tip. (Right) A 3D model reconstructed using the height image data.*

Presented in Figure 33, is the AFM image and subsequent reconstruction of the 3D model from the AFM height image data. As mentioned in section 3.5, the resolution of the height image is affected by the z-axis movement range of the AFM head, which is a function of the z-piezo crystal and is in the range of 10 μm typically. Additionally, the resolution can be affected by the aspect ratio of the AFM tip and the sensitivity of the AFM head's feedback loop. This reduced resolution can be clearly seen when comparing the AFM image in Figure 33 (left) and the SEM image in Figure 29 (4). In the AFM image, the sapphire domes can be seen as relatively smooth, indicating that the AFM has lost a lot of information about the very faceted, sharp, crystalline structures which can be found on the SEM images. Additionally, in the AFM image, all information about the sapphire substrate is completely lost, which could be valuable to the researcher. The SEM image, however, shows both the substrate and some of the B6TFMO material growing in the region between domes, which could indicate to the researcher that an ineffective (or effective) mask has been used during synthesis. This loss of crystal and substrate information could be due to incorrect tip aspect ratio being used or an insensitive feedback loop. This loss of information carries through to the 3D model. The AFM's 3D model, in Figure 33 (right), is produced by **Gwyddion©** software. The software is used to extrapolate the height information from the 2D image and then produce the 3D model. Much like the 2D image, the AFM 3D model displays a relatively smooth surface on the sample. The general structure of the domes can be seen while the crystalline, multifaceted, sharp surface is completely lost.

Additionally, any information on the sample's sapphire substrate is, again, lost, which would make calculating accurate geometrical values complicated. When compared to the 3D model produced using the SEM and **Meshroom©** software, in Figure 32, the AFM's 3D model has lost significant information on the sample's surface texture as well as the sample's substrate. The SEM's 3D model produced a 3D model with a texture which is complementary to the actual sample's surface with crystal boundaries and general shapes can be determined. Additionally, the sample's substrate surface is visible and therefore the samples geometry could be calculated with more accuracy.

However, the SEM's 3D model is not perfect. As reported in the In-Lens detector image of the sapphire dome sample Figure 29 (4), the sample grows from the sapphire surface, producing flat, rectangular shaped crystals which converge on a point to produce a general dome shape. The crystal growth is inconsistent, meaning the dome shape has protruding edges and overhangs all across its surface. These protruding edges and overhangs are completely absent in the SEM's 3D model. Even in the 3D models mesh Figure 31, before the sample's texture is applied to the model, the sample is all but devoid of these edges and overhangs on the surface and without the knowledge gained by the In-Lens image Figure 29 (4) a viewer of the 3D model alone may believe this sample to be smoother than it actually is.

# 7. Conclusions

In conclusion, this project developed a framework for optimizing imaging parameters in the SEM, to enhance the acquisition of photogrammetric datasets and to produce an alternative method to AFM for the reconstruction of 3D models. Additionally, a predictive and mathematics-based stage automation program was developed and implemented as an approach to decrease the most time-consuming aspect, namely, the data acquisition process. Moreover, developed framework facilitated the generation of a high-quality 3D model of a sapphire dome sample, using **Meshroom©**, an open-source photogrammetry software. Finally, the 3D model produced was subsequently compared against the AFM data of the of the same sample. The result is an accessible procedure to produce 3D models, using an SEM, which any researcher can carry out.

In this study scanning electron microscopy was evaluated as a candidate to produce 3D models of microscale structures using photogrammetry software. The microscale reconstruction of the 3D models exploited the fact that the input of the photogrammetry software was simply a dataset of image files. Therefore, because the SEMs output is image files, the software should theoretically have the ability to produce 3D models of microscale samples. As described in section 3.4.4, this method to produce 3D models through photogrammetry software has been carried out before. However, these studies used premium photogrammetry software in order to reconstruct their 3D models, which is not an option for some researchers. Additionally, the imaging methodologies used by previous studies have not been explicitly highlighted, this study addresses this through the development of a framework for optimizing imaging parameters. During the development of the framework to capture adequate datasets, various subjects, including those mentioned in section 6.6, were examined for their suitability for this project. This was carried out by focusing on refining imaging parameters for "microscopy for photogrammetry" in order to improve the throughput of 3D model reconstruction. Therefore, the imaging parameters (focus, astigmatism, brightness/contrast, apertures etc.) of the SEM were investigated. In tandem with this how photogrammetry algorithms obtain a 3D model and how mechanisms of microscale imaging using an SEM compare to that of macroscale imaging, were also investigated. This included phenomena such as edge effect, detector

position as well as sample stage movement. Stage movement was focused on in particular, as it was the limiting point in the workflow of dataset acquisition and the step which caused the largest bottle neck, with regards to time to image. By defining the EP of the stage, the time to image was vastly improved. However, the time taken to obtain the 96 images of the sapphire dome sample was approximately 6 hours, not including the time taken to scratch the surface and define the EP. This is contrasted to the comparably much shorter scan and 3D model reconstruction time of the AFM.

In an effort to reduce the time required for data acquisition, A predictive mathematics-based stage movement program was written through the Python programming language. When the sample was rotated or tilted to capture different perspectives of the same point of interest, the stage movement moves the point of interest out of illumination by the electron beam. By defining the movements of the sample on the sample stage and applying trigonometry, the program determined the 3D position of the point of interest after each movement. This produced co-ordinates for an entire dataset acquisition through a desired amount of different rotation and tilt values. After this, it was determined to need more refinement, particularly the value of h, who's error increased error in x and y, which compounded with greater magnifications. Machine learning algorithms will also be considered in the future in order to counteract the error introduced by the stage's mechanical movement (gear and screw hysteresis), particularly at high magnifications.

Finally, a dataset of a sample with a high degree of surface roughness (sapphire domes) was obtained. The dataset produced a 3D model through the open-source photogrammetry software **Meshroom©**, successfully. The method developed in this study is accessible to all researchers since the software is open-source and the widespread availability of SEMs. This has the potential to pave the way for exploring new avenues of research and analysis in a plethora of different fields. The resulting 3D model obtained from the SEM photogrammetry was compared to the AFM data of the sapphire dome surface. In the AFM images, data about the substrate is not discernible. The surface of the domes is seen to be flat, indicating that the sample has no surface roughness. In contrast, the SEM photogrammetry generated 3D model contained information about the substrate and exhibited surface roughness details. However,

it is important to note that the 3D model, while informative, appeared flatter compared to the input scanning electron micrographs. Any information on the crystalline surface details on the dome's surface were largely indiscernible in the 3D model.

One noteworthy characteristic of the sapphire dome sample is its ferromagnetic nature. The presence of ferromagnetism could have potentially led to distortion in the electron beam or interaction with escaping secondary or backscattered electrons. However, in this project, careful consideration was given to SEM parameters, including those relevant to photogrammetry. As a result, it is likely that the optimal parameters for imaging ferromagnetic samples, such as astigmatism correction and longer WDs were inadvertently chosen. These parameter selections, informed by the overall optimization process, helped mitigate the potential effects of ferromagnetism on the electron beam and contribute to obtaining high-quality imaging results.[140] Further research on the specific consideration and strategies for imaging ferromagnetic samples in the SEM can provide valuable insights for future magnetic samples.

## 8.    Future Work

In future work, it is essential to explore and evaluate a wider range of photogrammetry options, including both paid and other open-source software. These should then be assessed against each other to allow researchers to make informed choices based on their 3D model requirements. Furthermore, expanding the scope of the samples is important, particularly by incorporating diverse sample types, including insulating samples. This expansion necessitates the adoption of more rigorous sample and vacuum chamber hygiene practices, such as solvent and plasma cleaning to ensure accurate, non-disrupted images are obtained for photogrammetric datasets. Finally, to achieve higher-quality 3D models, more extensive data acquisition protocols will be applied, such as grid capture and increased magnifications. These enhancements will allow for a more comprehensive representation of the sample's features.

The geometry of the sapphire domes will be thoroughly analyzed and determined as part of further investigations. This will be further compared against using other 3D characterisation techniques to determine the validity of 3D photogrammetry for SEM as a method to determine the accurate height or slopes of surface structures.

Additionally, further research on quantitatively evaluating the roughness of the 3D model is important to analyse the quality of the established framework. This could be done by quantitatively analysing the surface of the samples and using this analysis to compare against the surface of the 3D model. This may prove difficult for different sample types and therefore a new methodology to determine this may be needed.

To further optimize the imaging process and reduce the burden of the significant time cost of this method, it is imperative to continue and improve the development of the stage automation program. This comes in the form of addressing existing errors, such as those encountered at high magnifications, is crucial to ensure the success of this program. The implementation of machine learning algorithms holds promise to enhance both the accuracy and efficiency of the positioning program. Additionally, obtaining the rights to the **Zeiss©** API could drastically improve this programs functionality, allowing it to directly control the SEMs controls, rather than just producing the coordinates for the user to input, and unlock new

possibilities for SEM-based photogrammetry. Furthermore, the implementation of an improved sample stage, such as the **Kleindik©** nanomanipulator, could efficiently define the EP of the sample to be wherever the user decides. The user would have complete control of the sample in 8 axes, significantly improving the time taken to image. However, these implementations would significantly increase the cost of the technique, which does not align with the project's goal.

# 9.    References

1.    Parker, A. J. Binocular depth perception and the cerebral cortex. *Nature Reviews Neuroscience* vol. 8 379–391 at https://doi.org/10.1038/nrn2131 (2007).

2.    Brewster, D. *The stereoscope; its history, theory, and construction, with its application to the fine and useful arts and to education*. (1856).

3.    Jimenez, J. R., Rubino, M., Diaz, J. A., Hita, E. & Del Barco, L. J. Changes in stereoscopic depth perception caused by decentration of spectacle lenses. *Optom. Vis. Sci.* **77**, 421–427 (2000).

4.    Seitz, S. M. & Kim, J. The Space of All Stereo Images. *Int. J. Comput. Vis. 2002 481* **48**, 21–38 (2002).

5.    Wade, N. J. Charles Wheatstone (1802-1875). *Perception* **31**, 265–272 (2002).

6.    Wade, N. J. & Ono, H. The stereoscopic views of Wheatstone and Brewster. *Psychol. Res. 1985 473* **47**, 125–133 (1985).

7.    Oculus Store: VR Games, Apps, & More | Oculus. https://www.oculus.com/experiences/quest/.

8.    Cipresso, P., Giglioli, I. A. C., Raya, M. A. & Riva, G. The past, present, and future of virtual and augmented reality research: A network and cluster analysis of the literature. *Front. Psychol.* **9**, 2086 (2018).

9.    Luckey, P. & Trexler, B. I. Virtual reality headset. (2013).

10.    Fauster, L. Stereoscopic Techniques in Computer Graphics. (2007).

11.    Koppal, S. *et al.* A viewer-centric editor for 3D movies. *IEEE Comput. Graph. Appl.* **31**, 20–35 (2011).

12.    Geng, J. Three-dimensional display technologies. *Adv. Opt. Photonics* **5**, 456 (2013).

13.    Lemle, E., Bomkamp, K., Williams, M. K. & Cutbirth, E. Virtual reality and the future of entertainment. *SpringerBriefs Comput. Sci.* **0**, 25–37 (2015).

14. Taubert, M., Webber, L., Hamilton, T., Carr, M. & Harvey, M. Virtual reality videos used in undergraduate palliative and oncology medical teaching: Results of a pilot study. *BMJ Support. Palliat. Care* **9**, 281–285 (2019).

15. Lopez, L. Virtual Reality And Augmented Reality In Education - eLearning Industry. *eLearning Industry* (2016).

16. Tredinnick, L. Virtual realities in the business world. *Bus. Inf. Rev.* **35**, 39–42 (2018).

17. Aber, J. S., Ries, J. B. & Marzolff, I. *Small-format aerial photography: Principles, techniques and geoscience applications*. *Small-Format Aerial Photography: Principles, Techniques and Geoscience Applications* (Elsevier, 2010). doi:10.1016/C2009-0-18493-3.

18. Linder, W. Digital photogrammetry: A practical course. *Digit. Photogramm. A Pract. Course* 1–220 (2009) doi:10.1007/978-3-540-92725-9/COVER.

19. Egels, Y. & Kasser, M. Digital Photogrammetry. *Digit. Photogramm.* (2001) doi:10.4324/9780203305959.

20. Shirai, Y. Three-Dimensional Computer Vision. (1987).

21. Sorabji, R. ARISTOTLE ON COLOUR, LIGHT AND IMPERCEPTIBLES. *Bull. Inst. Class. Stud.* **47**, 129–140 (2004).

22. Pirenne, M. H. THE SCIENTIFIC BASIS OF LEONARDO DA VINCI'S THEORY OF PERSPECTIVE*. *https://doi.org/10.1093/bjps/III.10.169* **3**, 169–185 (1952).

23. Gernsheim, H. The 150th anniversary of photography. *Hist. Photogr.* **1**, 3–8 (1977).

24. Polidori, L. ON LAUSSEDAT'S CONTRIBUTION to the EMERGENCE of PHOTOGRAMMETRY. in *International Archives of the Photogrammetry, Remote Sensing and Spatial Information Sciences - ISPRS Archives* vol. 43 893–899 (2020).

25. Collier, P. The development of photogrammetry in World War 1. *https://doi.org/10.1080/23729333.2018.1497439* **4**, 285–295 (2018).

26. Wolf, P. R., Dewitt, B. A., Wilkinson, B. E. & York Chicago San Francisco Athens London Madrid, N. *Elements of Photogrammetry with Applications in GIS*. (McGraw-Hill Education, 2014).

27. Schenk, T. Introduction to Photogrammetry. *Dep. Civ. Environ. Eng. Geod. Sci. Ohio State Univ.* 79–95 (2005).

28. Jiang, R., Jáuregui, D. V. & White, K. R. Close-range photogrammetry applications in bridge measurement: Literature review. *Measurement: Journal of the International Measurement Confederation* vol. 41 823–834 at https://doi.org/10.1016/j.measurement.2007.12.005 (2008).

29. Shevchenko, A. V *et al.* The rebirth and evolution of Bezymianny volcano, Kamchatka after the 1956 sector collapse. *Commun. Earth Environ.* **1**, (2020).

30. Omar, H., Mahdjoubi, L. & Kheder, G. Towards an automated photogrammetry-based approach for monitoring and controlling construction site activities. *Comput. Ind.* **98**, 172–182 (2018).

31. Peppa, M. V., Mills, J. P., Moore, P., Miller, P. E. & Chambers, J. E. Automated co-registration and calibration in SfM photogrammetry for landslide change detection. *Earth Surf. Process. Landforms* **44**, 287–303 (2019).

32. Howland, M. D., Kuester, F. & Levy, T. E. Photogrammetry in the field: Documenting, recording, and presenting archaeology. *Mediterr. Archaeol. Archaeom.* **14**, 101–108 (2014).

33. Baqersad, J., Poozesh, P., Niezrecki, C. & Avitabile, P. Photogrammetry and optical methods in structural dynamics – A review. *Mech. Syst. Signal Process.* **86**, 17–34 (2017).

34. Silva-Bolivar, G. J., Reyes Muñoz, C. A., Londoño-Marín, S. & Castro-Maldonado, J. J. Creation of digital risk doubles using motion capture and photogrammetry for computer-generated imagery content. in *Journal of Physics: Conference Series* vol. 1418 (2019).

35. Socker, D. G., Howard, R. A., Korendyke, C. M., Simnett, G. M. & Webb, D. F. NASA Solar Terrestrial Relations Observatory (STEREO) mission heliospheric imager. in *Instrumentation for UV/EUV Astronomy and Solar Missions* vol. 4139 284–293 (SPIE, 2000).

36. Elkhrachy, I. 3D Structure from 2D Dimensional Images Using Structure from Motion Algorithms. *Sustain.* **14**, (2022).

37. Iglhaut, J. *et al.* Structure from Motion Photogrammetry in Forestry: a Review. *Current Forestry Reports* vol. 5 155–168 at https://doi.org/10.1007/s40725-019-00094-3 (2019).

38. Ogle, K. Researches in Binocular Vision. *Arch. Ophthalmol.* **45**, 361–361 (1951).

39. Koenderink, J. J. & van Doorn, A. J. Affine structure from motion. *J. Opt. Soc. Am. A* **8**, 377 (1991).

40. Ullman, S. The interpretation of structure from motion. *Proc. R. Soc. Lond. B. Biol. Sci.* **203**, 405–426 (1979).

41. Lingua, A., Marenchino, D. & Nex, F. Performance analysis of the SIFT operator for automatic feature extraction and matching in photogrammetric applications. *Sensors* **9**, 3745–3766 (2009).

42. Munich, M. E. *et al.* SIFT-ing through features with ViPR. *IEEE Robot. Autom. Mag.* **13**, 72–77 (2006).

43. Sibbing, D., Sattler, T., Leibe, B. & Kobbelt, L. SIFT-realistic rendering. in *Proceedings - 2013 International Conference on 3D Vision, 3DV 2013* 56–63 (2013). doi:10.1109/3DV.2013.16.

44. Levi, G. A Short introduction to descriptors | Gil's CV blog. https://gilscvblog.com/2013/08/18/a-short-introduction-to-descriptors/#more-3 (2013).

45. Lowe, D. G. Object recognition from local scale-invariant features. in *Proceedings of the*

*IEEE International Conference on Computer Vision* vol. 2 1150–1157 (IEEE, 1999).

46.    Torres-Sánchez, J., López-Granados, F., Borra-Serrano, I. & Manuel Peña, J. Assessing UAV-collected image overlap influence on computation time and digital surface model accuracy in olive orchards. *Precis. Agric.* **19**, 115–133 (2018).

47.    Lowe, D. G. Distinctive image features from scale-invariant keypoints. *Int. J. Comput. Vis.* **60**, 91–110 (2004).

48.    Triggs, B., McLauchlan, P. F., Hartley, R. I. & Fitzgibbon, A. W. Bundle adjustment – a modern synthesis. in *Lecture Notes in Computer Science (including subseries Lecture Notes in Artificial Intelligence and Lecture Notes in Bioinformatics)* vol. 1883 298–372 (Springer Verlag, 2000).

49.    Furukawa, Y. & Hernández, C. Multi-view stereo: A tutorial. *Found. Trends Comput. Graph. Vis.* **9**, 1–148 (2015).

50.    Seifi, S. & Tuytelaars, T. How to improve CNN-based 6-DoF camera pose estimation. in *Proceedings - 2019 International Conference on Computer Vision Workshop, ICCVW 2019* 3788–3795 (2019). doi:10.1109/ICCVW.2019.00471.

51.    Geva, A., Briskin, G., Rivlin, E. & Rotstein, H. Estimating camera pose using Bundle Adjustment and Digital Terrain Model constraints. in *Proceedings - IEEE International Conference on Robotics and Automation* vols 2015-June 4000–4005 (2015).

52.    Nguyen, H. M., Wünsche, B., Delmas, P. & Lutteroth, C. 3D Models from the black box: Investigating the current state of image-based modeling. in *20th International Conference in Central Europe on Computer Graphics, Visualization and Computer Vision, WSCG 2012 - Conference Proceedings* 249–258 (2012).

53.    Moons, T., Van Gool, L. & Vergauwen, M. 3D reconstruction from multiple images part 1: Principles. *Found. Trends Comput. Graph. Vis.* **4**, 287–404 (2009).

54.    Agarwal, S., Snavely, N., Seitz, S. M. & Szeliski, R. Bundle adjustment in the large. in *Lecture Notes in Computer Science (including subseries Lecture Notes in Artificial*

*Intelligence and Lecture Notes in Bioinformatics)* vol. 6312 LNCS 29–42 (2010).

55.   Shum, H. Y., Ke, Q. & Zhang, Z. Efficient bundle adjustment with virtual key frames: A hierarchical approach to multi-frame structure from motion. *Proc. IEEE Comput. Soc. Conf. Comput. Vis. Pattern Recognit.* **2**, 538–543 (1999).

56.   Wojciechowska, G. & Luczak, J. Use of close-range photogrammetry and UAV in documentation of architecture monuments. in *E3S Web of Conferences* vol. 71 (EDP Sciences, 2018).

57.   Marr, D. & Poggio, T. A computational theory of human stereo vision. *Proc. R. Soc. London - Biol. Sci.* **204**, 301–328 (1979).

58.   Seitz, S. M., Curless, B., Diebel, J., Scharstein, D. & Szeliski, R. A comparison and evaluation of multi-view stereo reconstruction algorithms. in *Proceedings of the IEEE Computer Society Conference on Computer Vision and Pattern Recognition* vol. 1 519–526 (2006).

59.   Xiao, X. *et al.* Multi-view stereo matching based on self-adaptive patch and image grouping for multiple unmanned aerial vehicle imagery. *Remote Sens.* **8**, (2016).

60.   Skarlatos, D. & Kiparissi, S. COMPARISON of LASER SCANNING, PHOTOGRAMMETRY and SFM-MVS PIPELINE APPLIED in STRUCTURES and ARTIFICIAL SURFACES. in *ISPRS Annals of the Photogrammetry, Remote Sensing and Spatial Information Sciences* vol. 1 299–304 (Copernicus GmbH, 2012).

61.   Yu, Z. & Gao, S. Fast-MVSNet: Sparse-to-dense multi-view stereo with learned propagation and Gauss-Newton refinement. in *Proceedings of the IEEE Computer Society Conference on Computer Vision and Pattern Recognition* 1946–1955 (2020). doi:10.1109/CVPR42600.2020.00202.

62.   Nocerino, E., Stathopoulou, E. K., Rigon, S. & Remondino, F. Surface Reconstruction Assessment in Photogrammetric Applications. *Sensors 2020, Vol. 20, Page 5863* **20**, 5863 (2020).

63. Kazhdan, M., Hopkins University, J. & Hoppe, H. Screened Poisson Surface Reconstruction. *ACM Trans. Graph* **32**, (2013).

64. Furukawa, Y. & Hernández, C. Multi-View Stereo: A Tutorial. *Found. Trends® Comput. Graph. Vis.* **9**, 1–148 (2015).

65. Schonberger, J. L. & Frahm, J. M. Structure-from-Motion Revisited. in *Proceedings of the IEEE Computer Society Conference on Computer Vision and Pattern Recognition* vols 2016-Decem 4104–4113 (2016).

66. Chandler, J. H. & Fryer, J. G. Recording aboriginal rock art using cheap digital cameras and digital photogrammetry Underwater photogrammetry View project Quantifying landslide evolution using historical photography, digital photogrammetry and image processing View project. (2005).

67. Pepe, M. & Costantino, D. Techniques, tools, platforms and algorithms in close range photogrammetry in building 3D model and 2D representation of objects and complex architectures. *Comput. Aided. Des. Appl.* **18**, 42–65 (2020).

68. Dering, G. M., Micklethwaite, S., Thiele, S. T., Vollgger, S. A. & Cruden, A. R. Review of drones, photogrammetry and emerging sensor technology for the study of dykes: Best practises and future potential. *Journal of Volcanology and Geothermal Research* vol. 373 148–166 at https://doi.org/10.1016/j.jvolgeores.2019.01.018 (2019).

69. Nickolls, J. & Dally, W. J. The GPU computing era. *IEEE Micro* **30**, 56–69 (2010).

70. Krishna, A. V., Flys, O., Reddy, V. V. & Rosén, B. G. Surface topography characterization using 3D stereoscopic reconstruction of SEM images. *Surf. Topogr. Metrol. Prop.* **6**, 024006 (2018).

71. Ul-Hamid, A. *A Beginners' Guide to Scanning Electron Microscopy*. *A Beginners' Guide to Scanning Electron Microscopy* (Springer International Publishing, 2018). doi:10.1007/978-3-319-98482-7.

72. Wouters, R. & Froyen, L. Scanning electron microscope fractography in failure analysis

of steels. *Mater. Charact.* **36**, 357–364 (1996).

73. Goodhew, P. J., Humphreys, F. J. & Beanland, R. Electron microscopy and analysis. 17 (2001).

74. Hoseinzade, M., Nijatie, M. & Sadighzadeh, A. Numerical simulation and design of a thermionic electron gun. *Chinese Phys. C* **40**, 057003 (2016).

75. Jensen, K. L., O'Shea, P. G., Feldman, D. W. & Shaw, J. L. Emittance of a field emission electron source. *J. Appl. Phys.* **107**, 014903 (2010).

76. Pérez, F., Kemp, A. J., Divol, L., Chen, C. D. & Patel, P. K. Deflection of MeV electrons by self-generated magnetic fields in intense laser-solid interactions. *Phys. Rev. Lett.* **111**, 245001 (2013).

77. Hafner, B. Scanning Electron Microscopy Primer. *Charact. Facil. Univ. Minnesota—Twin Cities* (2007).

78. McKinlay, K. J. *et al.* Comparison of environmental scanning electron microscopy with high vacuum scanning electron microscopy as applied to the assessment of cell morphology. *J. Biomed. Mater. Res. - Part A* **69**, 359–366 (2004).

79. Muller, D. A. Structure and bonding at the atomic scale by scanning transmission electron microscopy. *Nature Materials* vol. 8 263–270 at https://doi.org/10.1038/nmat2380 (2009).

80. Kumar, A. & Arnold, W. High resolution in non-destructive testing: A review. *J. Appl. Phys.* **132**, 100901 (2022).

81. Allmendinger, T. A Classical Approach to the De Broglie - Wave Based on Bohr ' s H - Atom - Model. *Int. J. Appl. Math. Theor. Phys.* **2**, 1–15 (2016).

82. De Broglie, L. The wave nature of the electron. *Nobel Lect. Phys. 1922-1941* 244–256 (1929).

83. Nader, B., Dgania, P., Tikva, I. & Butto, N. A New Theory on Electron Wave-Particle

Duality. *J. High Energy Physics, Gravit. Cosmol.* **06**, 567–578 (2020).

84.   Wang, Y., Pan, J. A., Wu, H. & Talapin, D. V. Direct Wavelength-Selective Optical and Electron-Beam Lithography of Functional Inorganic Nanomaterials. *ACS Nano* **13**, 13917–13931 (2019).

85.   Goldstein, D. J. Resolution in light microscopy studied by computer simulation. *J. Microsc.* **166**, 185–197 (1992).

86.   Caldas, L. A. *et al.* Ultrastructural analysis of SARS-CoV-2 interactions with the host cell via high resolution scanning electron microscopy. *Sci. Rep.* **10**, 16099 (2020).

87.   Zhou, W., Apkarian, R., Wang, Z. L. & Joy, D. Fundamentals of scanning electron microscopy (SEM). in *Scanning Microscopy for Nanotechnology: Techniques and Applications* 1–40 (Springer New York, 2007). doi:10.1007/978-0-387-39620-0_1.

88.   Hawkes, P. W. MAGNETIC LENS THEORY. in *Topics in Current Physics* vol. 18 1–56 (Springer Verlag, 1982).

89.   Chang, W. Y. & Chen, F. R. Wide-range tunable magnetic lens for tabletop electron microscope. *Ultramicroscopy* **171**, 139–145 (2016).

90.   Guyon, J. *et al.* Sub-micron resolution selected area electron channeling patterns. *Ultramicroscopy* **149**, 34–44 (2015).

91.   Mohammed, A. & Abdullah, A. SCANNING ELECTRON MICROSCOPY (SEM): A REVIEW. *Proc. 2018 Int. Conf. Hydraul. Pneum. - HERVEX* 77–85 (2018).

92.   JEOL. Scanning Electron Microscopes A to Z: Basic Knowledge for using the SEM. *Semicond. Int.* **6**, 90–94 (1983).

93.   Goldstein, J. I. *et al.* Scanning electron microscopy and x-ray microanalysis. *Scanning Electron Microsc. X-ray Microanal.* 1–550 (2017) doi:10.1007/978-1-4939-6676-9/COVER.

94.   ZEISS. ZEISS GeminiSEM Family. 1–20 (2015).

95. Polman, A., Kociak, M. & García de Abajo, F. J. Electron-beam spectroscopy for nanophotonics. *Nature Materials* vol. 18 1158–1171 at https://doi.org/10.1038/s41563-019-0409-1 (2019).

96. Suri, A. *et al.* Analysis and detection of low-energy electrons in scanning electron microscopes using a Bessel box electron energy analyser. *J. Electron Spectros. Relat. Phenomena* **241**, 146823 (2020).

97. Joy, D. C., Joy, C. S. & Bunn, R. D. Measuring the performance of scanning electron microscope detectors. *Scanning* **18**, 533–538 (1996).

98. Everhart, T. E. & Thornley, R. F. M. Wide-band detector for micro-microampere low-energy electron currents. *J. Sci. Instrum.* **37**, 246–248 (1960).

99. Kotera, M., Fujiwara, T., Suga, H. & Wittry, D. B. A Simulation of the Topographic Contrast in the SEM. *Jpn. J. Appl. Phys.* **29**, 2312–2316 (1990).

100. Reimer, L. Scanning Electron Microscopy. **45**, 209 (1998).

101. Kumagai, K. & Sekiguchi, T. Sharing of secondary electrons by in-lens and out-lens detector in low-voltage scanning electron microscope equipped with immersion lens. *Ultramicroscopy* **109**, 368–372 (2009).

102. Yan, H., Voorhees, P. W. & Xin, H. L. Nanoscale x-ray and electron tomography. *MRS Bull.* **45**, 264–271 (2020).

103. Berg, C. F., Lopez, O. & Berland, H. Industrial applications of digital rock technology. *J. Pet. Sci. Eng.* **157**, 131–147 (2017).

104. Coindreau, O., Vignoles, G. & Cloetens, P. Direct 3D microscale imaging of carbon-carbon composites with computed holotomography. in *Nuclear Instruments and Methods in Physics Research, Section B: Beam Interactions with Materials and Atoms* vol. 200 308–314 (North-Holland, 2003).

105. Rau, E. I., Karaulov, V. Y. & Zaitsev, S. V. Backscattered electron detector for 3D microstructure visualization in scanning electron microscopy. *Rev. Sci. Instrum* **90**,

23701 (2019).

106. Haruta, T. Comparison of 3D Imaging Methods in Electron Microscopy for Biomaterials. *Analytics* **8**, 536–543 (2018).

107. Baumeister, W., Grimm, R. & Walz, J. Electron tomography of molecules and cells. *Trends Cell Biol.* **9**, 81–85 (1999).

108. Jenkinson, K. *et al.* Multimode Electron Tomography Sheds Light on Synthesis, Structure, and Properties of Complex Metal-Based Nanoparticles. *Adv. Mater.* **34**, 2110394 (2022).

109. Lučić, V., Förster, F. & Baumeister, W. STRUCTURAL STUDIES BY ELECTRON TOMOGRAPHY: From Cells to Molecules. *http://dx.doi.org/10.1146/annurev.biochem.73.011303.074112* **74**, 833–865 (2005).

110. Knobloch, J. L. *et al.* Structural and Elastic Properties of Empty-Pore Metalattices Extracted via Nondestructive Coherent Extreme UV Scatterometry and Electron Tomography. *ACS Appl. Mater. Interfaces* **14**, 41316–41327 (2022).

111. Hu, H. Multi-slice helical CT: Scan and reconstruction. *Med. Phys.* **26**, 5–18 (1999).

112. Reichelt, M. *et al.* 3D reconstruction of VZV infected cell nuclei and PML nuclear cages by serial section array scanning electron microscopy and electron tomography. *PLoS Pathog.* **8**, 1002740 (2012).

113. Ercius, P., Alaidi, O., Rames, M. J. & Ren, G. Electron Tomography: A Three-Dimensional Analytic Tool for Hard and Soft Materials Research. *Advanced Materials* vol. 27 5638–5663 at https://doi.org/10.1002/adma.201501015 (2015).

114. Weyland, M. & Midgley, P. A. Electron tomography. *Mater. Today* **7**, 32–40 (2004).

115. Baena, V., Schalek, R. L., Lichtman, J. W. & Terasaki, M. Serial-section electron microscopy using automated tape-collecting ultramicrotome (ATUM). *Methods Cell Biol.* **152**, 41–67 (2019).

116. Denk, W. & Horstmann, H. Serial block-face scanning electron microscopy to reconstruct three-dimensional tissue nanostructure. *PLoS Biol.* **2**, (2004).

117. Wacker, I. & Schroeder, R. R. Array tomography. *Journal of Microscopy* vol. 252 93–99 at https://doi.org/10.1111/jmi.12087 (2013).

118. Ender, M., Joos, J., Carraro, T. & Ivers-Tiffée, E. Quantitative Characterization of LiFePO 4 Cathodes Reconstructed by FIB/SEM Tomography. *J. Electrochem. Soc.* **159**, A972–A980 (2012).

119. Pintus, R., Podda, S. & Vanzi, M. Improvements in automated photometric stereo 3D SEM. in *Microscopy and Microanalysis* vol. 14 608–609 (Cambridge University Press, 2008).

120. Mignot, C. Color (and 3D) for Scanning Electron Microscopy. *Micros. Today* **26**, 12–17 (2018).

121. Kareiva, S., Selskis, A., Ivanauskas, F., Šakirzanovas, S. & Kareiva, A. Scanning electron microscopy: Extrapolation of 3D data from sem micrographs. *Medziagotyra* **21**, 640–646 (2015).

122. Diller, S. A Synoptic View on Microstructure: Multi-Detector Colour Imaging, nanoflight®. in *Biological Field Emission Scanning Electron Microscopy: Volume I: Volume II* vols 1–2 659–678 (John Wiley & Sons, Ltd, 2019).

123. Kozikowski, P. Extracting Three-dimensional Information from SEM Images by Means of Photogrammetry. *Micron* **134**, (2020).

124. Ball, A. D., Job, P. A. & Walker, A. E. L. SEM-microphotogrammetry, a new take on an old method for generating high-resolution 3D models from SEM images. *J. Microsc.* **267**, 214–226 (2017).

125. Schitter, G. *et al.* Design and modeling of a high-speed AFM-scanner. *IEEE Trans. Control Syst. Technol.* **15**, 906–915 (2007).

126. Méndez-Vilas, A., Nuevo, M. J., González-Martin, M. L. & Labajos-Broncano, L.

Quantitative Surface Roughness Determination of Materials by AFM: Some Limitations. *Mater. Sci. Forum* **408**–**412**, 239–244 (2002).

127. Ukraintsev, V. A., Baum, C., Zhang, G. & Hall, C. L. The role of AFM in semiconductor technology development: the 65 nm technology node and beyond. *https://doi.org/10.1117/12.602758* **5752**, 127–139 (2005).

128. Keeney, L. *et al.* Magnetic Field-Induced Ferroelectric Switching in Multiferroic Aurivillius Phase Thin Films at Room Temperature. *J. Am. Ceram. Soc.* **96**, 2339–2357 (2013).

129. Faraz, A. *et al.* Direct visualization of magnetic-field-induced magnetoelectric switching in multiferroic aurivillius phase thin films. *J. Am. Ceram. Soc.* **100**, 975–987 (2017).

130. Kanarik, K. J., Tan, S. & Gottscho, R. A. Atomic Layer Etching: Rethinking the Art of Etch. *J. Phys. Chem. Lett* **9**, 51 (2018).

131. Moore, K. *et al.* Charged Domain Wall and Polar Vortex Topologies in a Room-Temperature Magnetoelectric Multiferroic Thin Film. *Cite This ACS Appl. Mater. Interfaces* **14**, 5525–5536 (2022).

132. Yang, F. *et al.* Eight-logic memory cell based on multiferroic junctions. *J. Phys. D. Appl. Phys.* **42**, 072004 (2009).

133. Zephyr, 3DF. Photography Guide. https://www.3dflow.net/zephyr-doc/en/PhotographyGuide.html.

134. Erdman, N., Bell, D. C. & Reichelt, R. Scanning electron microscopy. *Springer Handbooks* 229–318 (2019) doi:10.1007/978-3-030-00069-1_5/COVER.

135. Frank, L., Zadražil, M. & Müllerová, I. Scanning electron microscopy of nonconductive specimens at critical energies in a cathode lens system. *J. Scanning Microsc.* **23**, 36–50 (2001).

136. Egerton, R. F., Li, P. & Malac, M. Radiation damage in the TEM and SEM. in *Micron* vol. 35 399–409 (Micron, 2004).

137. Dusevich, V. M., Purk, J. H. & Eick, J. D. Choosing the Right Accelerating Voltage for SEM (An Introduction for Beginners). *Micros. Today* **18**, 48–52 (2010).

138. Echlin, M. P., Mottura, A., Torbet, C. J. & Pollock, T. M. A new TriBeam system for three-dimensional multimodal materials analysis. *Rev. Sci. Instrum.* **83**, 023701 (2012).

139. Beb, M. Y. *et al.* Proposal for a complete 3D surface reconstruction using images from a scanning electron microscope (SEM). in *Optics InfoBase Conference Papers* JW5A.69 (Optica Publishing Group, 2022). doi:10.1364/fio.2022.jw5a.69.

140. Mager, M. Examining Ferromagnetic Samples in the SEM/EDX. *Micros. Today* **7**, 41–41 (1999).

# 10. Appendix

## 10.1. Code

```
In [263]:  import pandas as pd
           import matplotlib.pyplot as plt
           import numpy as np
           import scipy
           from scipy.spatial.transform import Rotation as R
           import os

           #when changing data, make sure to change dataset, tilts, rotations, POI, and mabye EU
```

```
In [312]:  os.chdir('C:\\Users\\david\\Desktop')
           df = pd.read_csv("test.csv")
           results = pd.read_csv("data3.csv")

           print(results)
```

```
        a       b
0  78.701  49.560
1  58.430  43.141
2  42.717  57.467
3  47.205  78.288
4  67.455  84.810
5  83.263  70.512
```

```
In [313]:  #tilts = [0,10]
           #rotations = np.linspace(0,340,num = int(340/20)+1)

           #tilts = [0,10,20,30]
           #rotations = np.linspace(0,270,num = int(270/90)+1)

           tilts = [20]
           rotations = np.linspace(0,300,num = int(300/60)+1)


           print(len(tilts)*len(rotations))
           print(tilts,rotations)


           for i,phi in enumerate(rotations):
               rotations[i] = -phi
           #location of point of interest at 0 tilt and rotation

           POI_x = 47.620

           POI_y = 51.510


           #eucentric point of stage
           eu_x = 63.086
           eu_y = 64.848

           h_arr = np.linspace(1,4, num = 300)

           average_x_error = np.zeros_like(h_arr)
           average_y_error= np.zeros_like(h_arr)


           err_x = np.zeros(len(tilts)*len(rotations))
           err_y = np.zeros(len(tilts)*len(rotations))

           x =  POI_x - eu_x
           y =  POI_y - eu_y
```

```
6
[20] [  0.  60. 120. 180. 240. 300.]
```

```
In [314]: def tilt(x, y, h, theta):
              x2 = x
              y2 = np.cos(theta) * y - h * np.sin(theta)
              #y2  = np.sqrt(y**2+h**2)*( (np.cos( theta+np.arctan(h/y) ) )/(np.cos(theta) ))
              #y2 = np.sqrt(y**2+h**2) * np.cos(np.arctan(h/y)+theta)

              #look into this section again
              h2 = np.sin(theta) * y + h * np.cos(theta)
              arr = [x2,y2,h2]
              return arr
```

```
In [315]:
          for j,h in enumerate(h_arr):
              count = 0


              for i,theta in enumerate(tilts):

                  print("-------------------------------")
                  print("Tilt = %s" %(int(theta)))
                  print("-------------------------------")
                  print("")

                  theta =  theta * (np.pi/180)

                  vec  = tilt(x,y,h,theta)


                  for i,phi in enumerate(rotations):
                      rotation_degrees = phi
                      rotation_radians = np.radians(rotation_degrees)
                      rotation_axis = np.array([0, -np.sin(theta), np.cos(theta)])

                      rotation_vector = rotation_radians * rotation_axis
                      rotation = R.from_rotvec(rotation_vector)
                      q1 = rotation.apply(vec)

                      q1[0] = q1[0] + eu_x
                      q1[1] = q1[1] / np.cos(theta) + eu_y


                      print("Rotation = %s:" %(-phi))
                      print("[",round(q1[0],3),",",round(q1[1],3),"]")


                      err_x[i+count] = np.absolute(q1[0]-results.loc[i+count,'a'])
                      err_y[i+count] = np.absolute(q1[1]-results.loc[i+count,'b'])


                      #print("")

                  count = count + len(rotations)

              average_x_error[j] = np.average(err_x)
              average_y_error[j] = np.average(err_y)



          df.to_csv("test.csv", index=False)
```

```
In [316]: #plt.plot(h_arr,average_x_error)
          plt.plot(h_arr,average_y_error)
          plt.plot(h_arr,average_x_error)

          print(h_arr[np.where(average_y_error == np.min(average_y_error))])
          print(average_y_error[np.where(average_y_error == np.min(average_y_error))])



          plt.show()
```
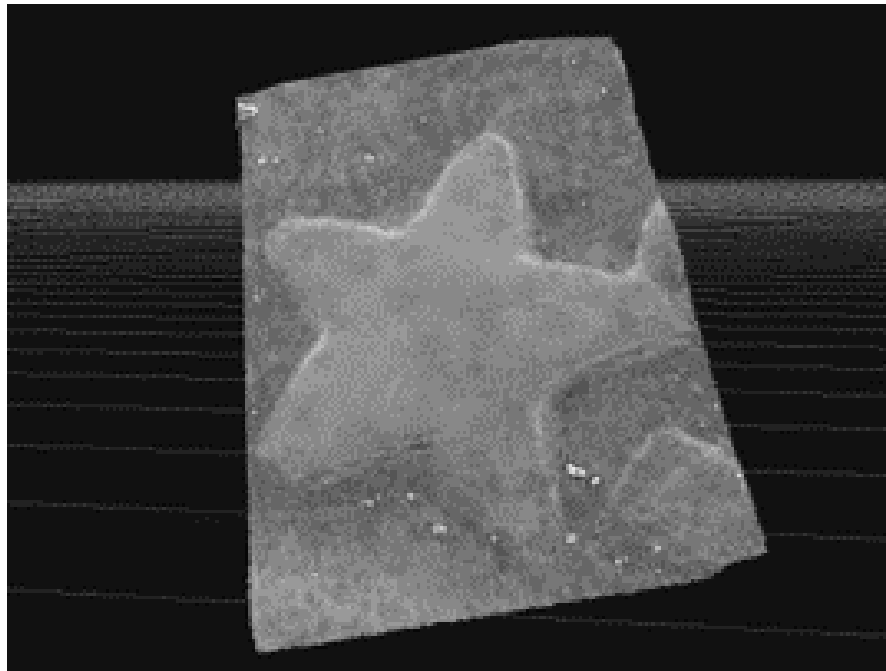
## 10.2. 10 cent coin



*Figure 34: 3D model of the 10 cent coin that was imaged*